ISSN 2236-5281

Technical Report
**INCoD/LAPIX.01.2021.E**

# Systematic Literature Review on Forecasting/Nowcasting based upon Ground-Based Cloud Imaging

**Authors**:
Bruno Juncklaus Martins
Allan Cerentini
Sylvio Luiz Mantelli Neto
Aldo von Wangenheim

Version 1.0
Status: Final
Distribution: External
**FEVEREIRO - 2021**

**Brazilian Institute for Digital Convergence**

Federal University of Santa Catarina - UFSC
Campus Universitário João David Ferreira Lima - Trindade
Departamento de Informática e Estatística - Room 320
Florianópolis-SC - CEP 88040-970

Phone/FAX: +55 48 3721-4715
**www.incod.ufsc.br**

ISSN 2236-5281

Relatório Técnico do Instituto Nacional para Convergência Digital/ Departamento de Informática e Estatística, Centro Tecnológico, Universidade Federal de Santa Catarina. -- v.11, n.01 (2021).-- Florianópolis: INE, UFSC, 2011 - 2021

Semestral
Resumo em português

ISSN 2236-5281

1. Convergência digital. 2. Tecnologia da informação. 3. Visão Computacional. 4. Energia Fotovoltaica. 5. Inteligência Artificial. Universidade Federal de Santa Catarina. Departamento de Informática e Estatística.

# Systematic Literature Review on Forecasting/Nowcasting based upon Ground-Based Cloud Imaging

**Bruno Juncklaus Martins[1,*,+], Allan Cerentini[1,*,+], Sylvio Luiz Mantelli Neto[2,*,+], and Aldo von Wangenheim[1]**

[1]UFSC Federal University of Santa Catarina, INE, Florianópolis , 88040-900, Brazil
[2]INPE Brazilian National Institute for Space Research, CCST, São José dos Campos, 12227-010, Brazil
[*]Corresponding authors: bjuncklaus@gmail.com, allancerentini@gmail.com, sylvio@lepten.ufsc.br, aldo.vw@ufsc.br
[+]these authors contributed equally to this work

## ABSTRACT

Artificial Neural Networks (ANN) are being used on several fields mostly as a mapper from input domain variables into output application area results. Several methods are being used on the automatic assessment of clouds from surface to predict solar power generation, assisted by a camera, side sensors, etc. The present Systematic Literature Review (SLR) is intended to search the related scientific articles, to find the state of the art in the area. We were able to find gaps in researches in regards to validation metrics for prediction of solar power generation as well as a small number of works in this domain area using computational intelligence (machine learning) methods, with the majority of works relying on classical statistics approaches. Results show that most works rely on images captured by Total Sky-imagers (TSI) and most works using computational intelligence rely on classical approaches like Artificial Neural Networks, Convolutional Neural Networks (CNN) and Multilayer Perceptrons (MLP) and that there still a relevant amount of works published from the last three years using classical statistics.

## Introduction

The automated assessment of surface cloud observations has been studied by several years. The World Meteorological Organization (WMO) calls continuous sky monitoring equipment Synoptic Observation Systems (SOS) [1]. Authors are not looking for satellite-based or airborne-based methods, although they could provide essential tools for method validation, they are post-processing methods. The focus of the presented revision is only on short range forecasting and current atmospheric conditions. Therefore, we start looking for low cost effective recent methodologies, based on modelling from data statistics and Neural Networks from 2011 and move on to surface cameras monitoring stations.

The presented systematic literature review (SLR) uses the following open access research bases. Over the next sections we discuss the methodology performed.

- IEEE: Institute of Electrical and Electronics Engineers.
- SD: Science Direct Digital library.
- ACM: Association of Computer Machinery.
- AX: Arxiv is an open-access repository of electronic pre-prints.
- SP: Springer.

## Methods

The SLR begins on open access Journals, Magazines and Conferences from the year 2011 up to the date of the search (year 2020), defining the semantic keywords used on general search. We consider the year of publication only, therefore an article might have a more recent review. Every search is data stamped, allowing to track and include any additional publication until the research is closed. The initial search will be performed automatically on titles using keywords. Then a reading inspection on titles, abstracts and text will remove the remaining articles that could not be excluded by automatic search and out-of-scope

contents. The most significant ones used on the research will be included in the literature by the end of this report. A short description specific for each base will also be described.

### The initial inclusion/exclusion search strings

The main subject has similar words for example: cloud, clouds and cloudiness. Instead of defining all the similar words, the wildcard * will cover any letters or none (e.g. cloud*). The same applies for forecast* and predict*. The short range horizon of prediction words are commonly referenced as short term, very short, intra-hour, now-cast, nowcast, nowcasting. It's decided to use the key words: short term, very short, now* and intra.

Other keywords were also considered for example: sky imager, sky imaging, fisheye, fish-eye or fish eye or camera or cameras (sky imag*, ou fish*, ou camera*), Solar Irradiance or Irradiance (Solar Irradia* ou irrad*) and also Neural networks, Neural network (Neural network*). But their inclusion resulted in too many references from query. The keywords used on each database is described on Table 1.

| # | Base | Initial Search String |
|---|---|---|
| 1 | IEEE | ("All Metadata":"Cloud")<br>AND ("All Metadata":"Camera" OR "All Metadata":"Image")<br>AND ("All Metadata":"Intra" OR "All Metadata":"Prediction" OR "All Metadata":"Flow"<br>OR "All Metadata":"Movement" OR "All Metadata":"Track" OR "All Metadata":"forecast")<br>NOT ("All Metadata":"Cloud Computing")<br>NOT ("All Metadata":"Point Cloud")<br>NOT ("All Metadata":"Cloud-Computing")<br>NOT ("All Metadata":"Satellite") |
| 2 | SD | ("Cloud")<br>AND ("Image")<br>AND ("Intra" OR "Prediction" OR "Flow" OR "Movement" OR "forecast")<br>NOT ("satellite")<br>NOT ("Point Cloud") |
| 3 | ACM | Abstract:((Intra* OR Prediction OR flow OR movement* OR forecast*))<br>AND Title:(NOT satellite)<br>AND Abstract:(image)<br>AND Title:(cloud)<br>AND Abstract:(cloud) |
| 4 | AX | title=cloud OR solar power OR photovoltaic OR segmentation;<br>NOT title=radar;<br>NOT title=satellite;<br>NOT title=point;<br>NOT title=cloud computing;<br>AND abstract=photovoltaic OR movement OR flow OR coverage OR irradiance OR photovoltaic;<br>NOT abstract=cloud computing;<br>NOT abstract=star;<br>AND abstract=nowcast OR predict OR forecast;<br>AND abstract=movement OR flow OR coverage OR irradiance OR photovoltaic;<br>AND abstract=cloud OR solar power OR photovoltaic OR segmentation |
| 5 | SP | Disciplines: Energy, Engineering, Computer Science<br>(cloud AND image AND sky)<br>AND (intra OR prediction OR flow OR movement OR forecast)<br>AND NOT (satellite OR "Point Cloud" OR "computing")<br>AND (solar OR irradiance) |

**Table 1.** Databases and search strings used.

#### *Exclusion Criteria*

The following criteria were used to exclude articles from being included in the revision. These were considered during a full-text reading of the articles:

- Not using images as an input

- Main objective being cloud detection/classification or cloud motion
- Not providing a forecast of some sort
- Comparative studies
- Using satellite data only
- Predicting sun coverage only

Table 2 shows the resulting amount of articles removed by our criteria. After exclusion we obtained 1.245 articles, in which 2 were duplicated and were also removed. Three articles ([2], [3], [4]) were also removed due to the lack of a PDF file available at the Arxiv platform and one article was removed due to the lack of a formatted citation on the same platform (exact error: 404 Citation entry not found.). In total we removed 68 unique articles via exclusion criteria.

| Exclusion Criteria | Amount |
|---|---|
| No image | 46 |
| Cloud detection | 15 |
| Cloud tracking | 4 |
| Study | 3 |
| Cloud classification | 1 |
| Satellite | 1 |
| Sun coverage | 1 |

**Table 2.** Amount of excluded articles by exclusion criteria.

***IEEE Explore reference search***
IEEE Explore initially returned too many results. In order to reduce to a maximum of 2000 results, we restricted the search to open access articles only and added several exclusion keywords, until we reached 290 results. The system limited the search string to 20 logical terms. We reduced the set to 210 after exclusion by only reading the titles, and reduced to 36 by reading the abstracts and finally to 17 by reading the text. The results are described in the first row of Table 3. In the end 27 articles were included. Additional information on search sentences syntax etc, can be found on IEEE explore digital library resources and help.

***Science Direct reference search***
Science Direct returned 355 articles initially. The resulting articles were reduced to 288 after reading the titles and reduced furthermore to 28 after reading the abstracts. After reading the full-text of the remaining articles 10 were removed, resulting in 29 included articles. Additional information on search sentences syntax etc, can be found on ScienceDirect Support Center.

***Association of Computer Machinery reference search***
The ACM search engine allows the usage of wildcards, therefore we took advantage of the feature reducing the amount of keywords necessary to obtain the desired results. Initially the search string returned 49 results, after reading the titles we reduced it to 41 results and after reading the abstracts we reduced it even further, to 4 articles. There were only 2 exclusion after reading the texts for this database, which resulted in the addition of 2 articles in the SLR. This Help Article gives more information about the search engine used.

***Arxiv reference search***
Initially we obtained 443 results from Arxiv, however after a thorough analysis of the obtained resulting articles we decided to refine the search string used. This new search string is the one presented in this SLR in which returned 454 references initially, after reading the titles we obtained 395 references and after reading the remaining papers abstracts we reduced it to 9 articles. Finally after reading the full-text of the remaining articles we removed 44 articles and ended up with 6 included articles. More information can be found on this Help Page.

***Springer reference search***
Springer initially returned 97 results. After reading the title of the results we reduced it to 85 articles and reduced it further down to 8 articles after reading all the abstracts. After reading the remaining articles we decided to removed 3 results, ending up with only one article included. More information about the search engine can be found on this Help Article.

| # | Base | Date | Initial | Title | Abstract | Text | Included |
|---|---|---|---|---|---|---|---|
| 1 | IEEE | $May, 5^{th}2020$ | 290 | 210 | 36 | 17 | 27 |
| 2 | SD | $May, 8^{th}2020$ | 355 | 288 | 28 | 10 | 29 |
| 3 | ACM | $May, 28^{th}2020$ | 49 | 41 | 4 | 2 | 2 |
| 4 | AX | $Dec, 21^{st}2020$ | 454 | 395 | 9 | 44 | 6 |
| 5 | SP | $May, 28^{th}2020$ | 97 | 85 | 8 | 3 | 1 |

**Table 3.** Databases, initial results and subsequent remaining amount articles after: title, abstract and article reading.

# 1 Results

In this section, we give a short description of the selected article, grouped by year, with a picture representing the main idea of the original article. In total we selected 65 papers.

## 1.1 2011

### *1.1.1 Intra-hour forecasting with a total sky imager at the UC San Diego solar energy testbed*

In [5] a rooftop mounted TSI 440A total sky imager (TSI, Yankee Environmental Systems, has taken images of the sky over UCSD since August 2009. The instrument consists of a spherical mirror and a downward pointing camera. The camera provides images that are 640 by 480 pixels and the mirror occupies 420 by 420 pixels. Images are taken every 30 s when the sun is above an elevation angle of 3. The authors developed their own algorithm and all image processing is conducted on raw image output. The cloud detection technique is based on the concept of the ratio of the red channel to the blue channel developed at the Scripps Institution of Oceanography. A clear sky background image is generated for each sky image based on the current solar ZA. The Clear Sky Library (CSL) threshold is defined to be the red-blue-ratio (RBR) in the clear sky background image plus an additional threshold value. A pixel is classified as cloudy if its RBR is larger than the CSL threshold. A sunshine parameter is used in addition to the CSL to improve cloud decision in the circumsolar region. SP is computed as the average RBR of the pixel area on the shadowband around the sun position. Pixels with RBR $>$ SP are classified as cloudy even if the CSL indicates otherwise. To estimate the sky conditions between a given ground point and the sun, the intersection of the vector to the sun from that point on the ground to the cloud map is computed. Cloud velocity and direction of motion is determined through the cross-correlation method (CCM) applied to two consecutive sky images. To forecast cloud cover, the cloud map at time $t_0$ is advected at the speed and direction of the global vector determined from cross-correlating the images at time $t_0$ and $t_0 - dt$ ($dt = 30s$). The sky image is divided into the circumsolar region and the outer region. The matching error between the two cloud maps is the ratio between the number of falsely forecasted pixels and the number of total pixels in a region. The CSL was compiled as a sun-pixel-angle by zenith angle (ZA) lookup table from a full day of images on September 24, 2009. After performing the CCM only on cloudy region, and vectors with cross-correlation coefficients less than 0.8 are removed, most remaining vectors are uniform. By computing the average and standard deviation of the vector field, the remaining outlier vectors are eliminated. Using the binary irradiance technique global horizontal irradiance time series were produced for the ground stations with daily availability on 4 days. The results are presented in Figure 1.

| | CLR/CLR (%) | CLR/CLD (%) | $CLR_m$ count | CLD/CLR (%) | CLD/CLD (%) | $CLD_m$ count | % Correct |
|---|---|---|---|---|---|---|---|
| September 14, 2009 | 47.1 | 52.9 | 594 | 28.3 | 71.7 | 368 | 56.6 |
| October 4, 2009 | 76.2 | 23.8 | 441 | 10.3 | 89.7 | 419 | 82.8 |
| March 4, 2010 | 63.1 | 36.9 | 157 | 33.3 | 66.7 | 144 | 64.8 |
| March 10, 2010 | 52.7 | 47.2 | 110 | 7.0 | 93.0 | 201 | 78.8 |
| Total | 59.4 | 40.6 | 1302 | 18.5 | 81.5 | 1132 | 69.7 |

**Figure 1.** Distribution of measured versus TSI nowcast clear (CLR) and cloudy (CLD) conditions for skies with cloud fraction $0.2 \leq cf \leq 0.8$ (fraction of hemispheric solid angle). In line 1, the first term denotes measured sky conditions, and the second is the TSI estimate, thus CLD/CLR means the ground station measured cloudy conditions but the TSI estimated clear. $CLR_m$ and $CLD_m$ are the number of clear and cloudy measurements, respectively, in the outer region. The last column shows the overall statistics (not conditioned on cloudy or clear). Data is for all available stations.

## 1.2 2012

### *1.2.1 Forecasts of PV Power Output Using Power Measurements of 80 Residential PV Installs*

The authors in [6] used measurements of PV power output from 80 residential rooftop systems distributed over a 50 km x 50 km area are used to forecast PV power output. Measurements are recorded at 15-minute intervals, and each measurement

represents the average AC power over the previous 15 minutes. First, a clear-sky expectation for the output of each system is obtained. Subsequently, the authors correct for outages, system orientation, and partial shade due to permanent obstacles (not clouds). Finally, they identify deviations from the clear-sky operation of the system as the effect of clouds. The authors explored three ways of estimating cloud velocity using: wind velocity from the WRF model; cloud velocity inferred from the network of PV systems; a constant velocity throughout the day that is numerically optimized (retrospectively) to minimize the RMS error. The authors use images from a wide-angle camera mounted on a dual-axis equatorial tracker that follows the sun throughout each day. Using a block-motion estimation algorithm, the velocity of clouds in the image (in pixels/second) is determined. Then the velocity of pixels in the image are converted to estimate cloud velocity in real-world coordinates. A forecast of cloud position up to 10 minutes into the future is taken. These forecasts can predict cloud arrival times with an accuracy of a few minutes. Figure 2 shows the block-motion estimation method to estimate the velocity of clouds in different parts of the image. The authors achieved an RMS error/Avg. power of 0.29 for 15 mins. ahead forecast, up to 0.37 for for 75 mins. compared to an RMS Error of the Weather Research and Forecasting 0.51.

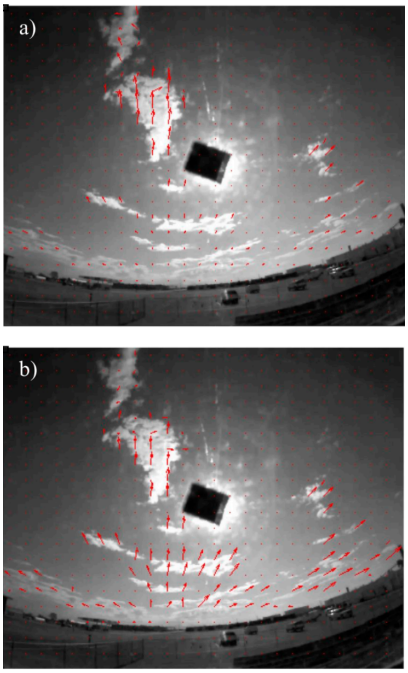


**Figure 2.** Sky images taken with a camera mounted on a dual-axis tracker pointed at the sun. Red arrows indicate motion vectors obtained from block motion estimation analysis. Motion vectors represents velocity in a) pixels/second b) meters/second. The sun is obscured by a piece of black tape.

#### *1.2.2 Solar Forecasting and Variability Analyses using Sky Camera Cloud Detection & Motion Vectors*

In [7] the authors use a cloud detection methodology based on images from clear days, the expected RBR is determined and stored in a clear sky library. On cloudy days, the RBR is compared against the clear sky library. If the RBR exceeds the clear sky library by more than 0.18, a pixel is classified as cloudy. Cloud velocity is used to advect the clouds detected forward in time to project shadow locations. Figure 3 illustrates a cross-correlation method using two images on October 4, 2009 at 161830 and 161900h. A region of pixels from (a) is correlated to (b) within a search distance. The location of the highest correlation is found and a motion vector is defined. The box is looped over the entire image to obtain a motion vector field and the average of that vector field is determined.

After advecting the cloud map using the velocity determined, a binary cloud and clear map is generated. Cloud shadows are then projected onto the ground using the solar azimuth and elevation angles to determine shading of PV systems. The cloud shadow is used to determine which PV systems are affected by clouds. However, irradiances are not measured directly so a cloud optical depth has to be provided. Currently the optical depth is determined from separate irradiance measurements and all clouds are assumed to have the same optical depth. In the result presented, cloudy periods are assumed to bring about a 60% reduction in irradiance.

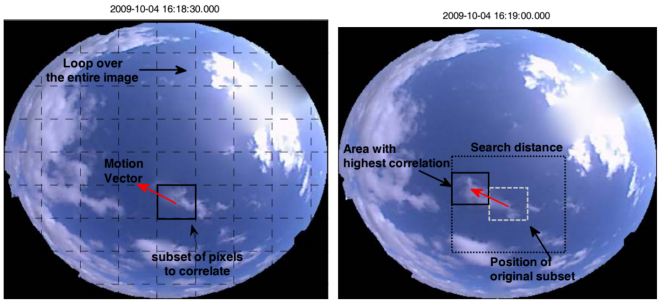


**Figure 3.** Cross correlation method used to determine cloud velocity

### *1.2.3 Correlation and Local Feature Based Cloud Motion Estimation*

The work from [8] uses both correlation and local feature approach to predict the cloud motions. The phase correlation approach uses two images with the same size to compute the motion vectors with 2D Fourirer transform, which makes it weak to noise. The cross correlation approach uses the Pearson Correlation Coefficient between two images to calculate the motion vector, this approach is robust to noise but is slower and cannot handle cloud shape changes. Both approaches have severe drawbacks like: they are unable to detect accurate vector when a cloud shape changes, sensitivity to intensity changes and suffer from low resolution around boundary area. So circumvent those problems an local feature method, Partially Intensity Invariant Feature Descriptor, was used to adjust motion vectors detected by correlation methods. The method was used to track the clouds feature points and calculate the motion vectors between two images, as we can see in figure **??**. The author improves both approaches, phase correlation and cross correlation modifying its parameters. On the first one, he uses different block sizes for the center of images e smaller for boundary. The second is to fill local mean values into the boundary area and shadownband, to remove spurious motion vectors. On the last approach he utilises an external algorithm to remove spurious motion vectors from the image. Then both improved methods were used as an hybrid approach that is robust to intensity and multi-layer clouds and some degree of cloud shape change. The proposed methods reduced the error rate by 25% on average to predict motion frames.

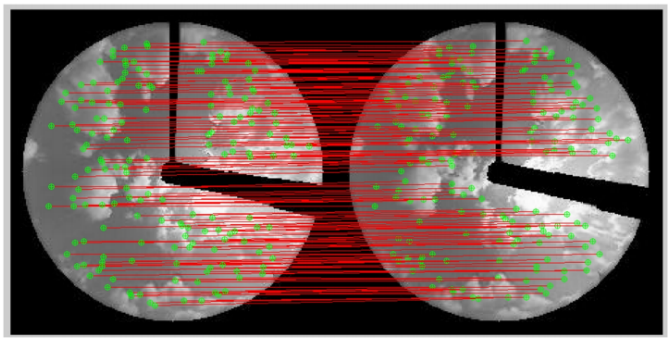

(a) Local feature pairs from two frames

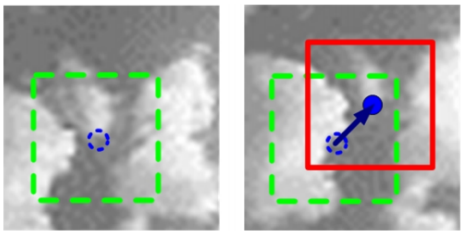

(b) Motion vector from local feature pair

**Figure 4.** Motion vector detection using local features

## 1.3 2013

### 1.3.1 Hybrid intra-hour DNI forecasts with sky image processing enhanced by stochastic learning

The paper in [9] uses experimental data for collected at an observatory in Merced, CA during the Spring, Summer and Fall of 2011. Sky images were recorded with the Yankee Environmental Systems Total sky imager (TSI 880) every 20 s. The TSI built-in software computes the daily sun percentage (SP) index. The authors developed an empirical expression specific to the data, in which the clear-sky DNI is given by a polynomial expression that depends on the cosine of the solar zenith angle. The algorithm to convert the TSI images into numerical information for the forecasting models can be summarized in four main steps: projection of the original image onto a rectangular grid, computation of the velocity vectors, identification of cloud pixels, and the calculation of cloud indices. In the present work, ANNs were trained with the Bayesian regularization process that uses the Levenberg–Marquardt optimization. The first six variables are the cloud cover indices, and the remaining variables are the time-lagged values of DNI ranging from 0 to 20 min in steps of 5 min. They employed two validation methods: cross validation (CVM) and randomized training and validation (RTM). RTM is a learning process which selectively chooses part of the learning period for training. It is based on the premise that not all elements of the available data are equally informative for ANN training (e.g. outliers or repeated data points). This strategy searches for the optimal composition of the training sets by means of some optimization algorithm, in this case is the GA. The GA optimization objective function in this study computes the models' performance by means of the validation methods (CVM or RTM). The GA chromosome length is fixed. The chromosome for ANN[CVM] optimization contains 13 elements. The first 11 are binary and decide whether an input vector is selected or not as an ANN input. The last two are integers, the first represents the number of layers ($L = \{1,2,3,4\}$), and the second represents the number of neurons ($N = \{1,....,20\}$). Once persistence, deterministic and ANN-based forecasting models were determined for both periods (high and low DNI variability) we defined a smart forecasting model that uses the best model from each period to create a season-independent model. Three statistical metrics for the models' error were used to assess their performance: mean bias error (MBE), RMSE, forecast skill (s). The performance metrics for these models are presented in Figure 5, with results showing that the smart forecasting model outperforms all other models regardless of the forecast horizon.

| Models | 5 min forecast | | | 10 min forecast | | |
|---|---|---|---|---|---|---|
| | MBE (Std) [W/m$^2$] | RMSE (Std) [W/m$^2$] | s (Std) [%] | MBE (Std) [W/m$^2$] | RMSE (Std) [W/m$^2$] | s (Std) [%] |
| Smart model | **−0.2** | **88.6** | **20.9** | **−1.9** | **103.3** | **22.5** |
| | (0.1) | (0.5) | (0.4) | (0.4) | (0.6) | (0.4) |
| $ANN_{LV}[RM]$ | −14.1 | 104.8 | 6.5 | 34.6 | 141.3 | −5.6 |
| | **(0.0)** | **(0.1)** | **(0.0)** | **(0.1)** | **(0.1)** | **(0.0)** |
| $ANN_{HV}[CVM]$ | −5.5 | 90.7 | 19.0 | −7.5 | 103.9 | 22.1 |
| | (0.1) | (0.6) | (0.6) | (0.6) | (0.7) | (0.5) |
| Deterministic | −10.7 | 150.5 | −25.6 | −8.3 | 144.0 | −7.4 |
| Persistence | 2.1 | 112.0 | 0.0 | 3.6 | 133.4 | 0.0 |

**Figure 5.** Cross correlation method used to determine cloud velocity

### 1.3.2 Intra-hour DNI forecasting based on cloud tracking image analysis

In [10], images of the sky are taken at 1 min intervals at the University of California Merced's solar observatory station using Yankee Environmental Systems' TSI-880. High quality solar irradiance data has been collected at the UC Merced Solar Observatory since September 2009. Binary masks are created where the element values are used to indicate true or false pixel values. Regions indicated as true are the regions of interest (ROI) and only these pixels are used in the cloud decision and forecasting exercises. The binary masks are created by making use of predict able attributes of the images:

1. The images are always enclosed by a circle located of the same size and centered at a constant position.
2. The shadow-band and nearby objects in the horizons such as poles are always the same size and shape.
3. The shadow-band moves in a predictable fashion, according to the solar azimuth angle.

The task of determining the circumference of the ROI uses the function *CircularHough_Grd* available at the Matlab Central File Exchange. The orientation of the shadow-band is determined using solar azimuth calculations obtained from Duffie and Beckman (2006). The authors use the 'MPIV' computer software developed by Mori and Chang (2003) to obtain the cloud velocity fields. The interrogation window is defined by a 32 pixels 32 pixels area, and the overlap between two consecutive windows is set to 50%, with maximum displacements set to 20 pixels for both vertical and horizontal directions. For each image, several velocity vectors are computed depending on the local motions of clouds at points. A representative velocity vector is chosen by applying k-means clustering on the distribution of velocity vectors. Then the authors cluster each velocity

field around two cluster means, which are determined using a cluster means algorithm. For the cloud pixel identification they follow an approach proposed by Li et al. which employs an adaptive threshold scheme. In order to forecast solar irradiance, the authors construct a set of grid elements originating from the sun's position and oriented in column-wise fashion in the reverse direction of the cloud flow field as shown in Figure 6. The direction is obtained from the representative velocity vectors. With this methodology the number of grid elements is limited by the size of the image (255 255). In this work, up to 6 grid elements are used. For each grid element cloud fractions are computed. Evaluations of the RMSE errors demonstrate that sky imagers are useful for 3–15 min ahead forecasting horizons. Comparing with a persistent model, it appears that the most significant forecast accuracies are for 5-min ahead.

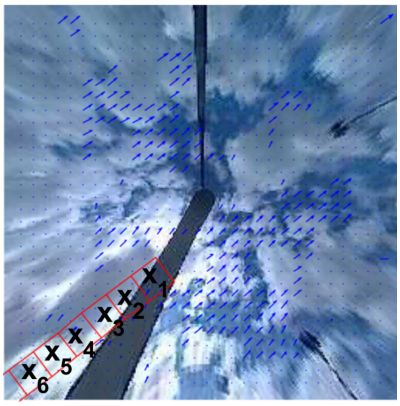


**Figure 6.** The squares indicate regions of interest assigned for variables $X_1, ..., X_6$. Each variable represents the computed cloud fraction in the designated regions.

#### *1.3.3 Low-cost solar micro-forecasts for PV smoothing*

In [11], a digital SLR camera mounted on a tracker is used, combined with a Licor LI-200 pyranometer mounted in the vicinity. A neural network based on Adaptive Resonance Theory (ART) was applied to associate cloud patterns with irradiance values 60 seconds. For the particular type of ART architecture used in this study, referred to as Fuzzy ART, the output layer is a winner-takes-all structure; the output code for a given category of input pattern will be represented as a single active neuron. The Lateral Priming Adaptive Resonance Theory (LAPART) network architecture is based upon the lateral coupling of two Fuzzy ART subnetworks, referred to as A and B and shown in Figure 7. The input patterns, network layers, and prototype templates are labeled with an A or B referring to the A or B Fuzzy ART subnetworks. The present approach to learning the relationships between cloud patterns and their movement at one time, and PV array irradiance at a future time utilizes a LAPART neural network. In the prototype LAPART application described in this paper, circumsolar cloud images are processed and presented to subnetwork A. The solar irradiance signal at a future time is presented to subnetwork B. As the subnetworks form category codes for these inputs, the LAPART network learns inference relations between them within the lateral connection matrix. A prediction consists of the inferred B node index and the associate template hyperbox. A correct inference occurs when the input falls within the inferred hyperbox, an inference error occurs when it falls outside otherwise. When an input arrives at the A subnetwork for which there is no direct access prototype and therefore no inferred B prototype, then an anomaly is declared. The total number of samples used is 360. For calculating performance measures, the data are equally partitioned into training and validation sets. Training required three passes through the training set while performance assessment required a single pass through the validation set. The data were shuffled prior to partitioning. As the number of irradiance categories (1-D hyperboxes) increases, the total error decreases, for 0.8 categories the RMS is 43.7 and for 0.98 is 7.9.

### 1.4 2014

#### *1.4.1 Bi-model short-term solar irradiance prediction using support vector regressors*

In [12], the device used to capture the all sky images is the all sky camera manufactured by the Santa Barbara Instrument Group. The experimental dataset is collected at a costal site in Taiwan. One all-sky image is captured per minute. SVM is used extract features from the all-sky images. The authors adopt five image features that exhibit higher absolute value of the correlation with the solar irradiance to be predicted: mean intensity level, mean gradient magnitude, averaged accumulated intensity of the vertical line of sun, and the mean and variance of cloud cover in a fixed time duration. When constructing prediction models, the authors separate the training data into two categories automatically by analyzing the cloud pixels in the region at the sun position. Two separated prediction models are trained using the two categories of training data according to the cloud obstruction condition near the solar disk. The first category contains data under the conditions when region at the sun

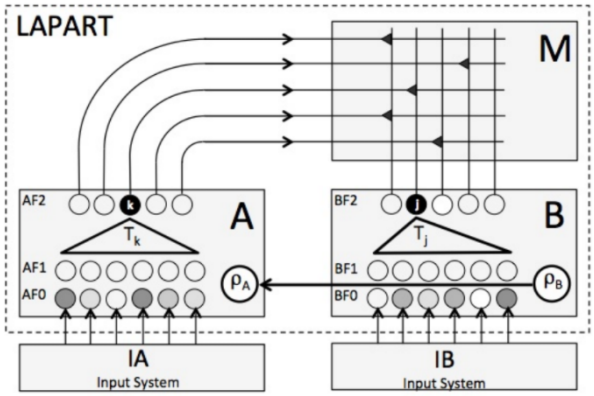


**Figure 7.** Standard LAPART network. The weights in the lateral connection matrix M are learned through a training process. The nodes containing $\rho$s are the vigilance nodes. The filled nodes in the AF2 and BF2 layers encode the current A and B categories.

position is clear. The second category contains data under the conditions when the region at the sun position is occluded by clouds. After predicting the short-term solar irradiance via regression, a refinement procedure is taken to improve the prediction results. In the proposed system, the authors generate ramp-down events if the difference between $CI_{i-1}$ and $CI_i$ is larger than a threshold. The labeled ramp-down events and the corresponding feature vectors $x_i$ are used to train a two-class SVM classifier. The trained classifier outputs one if a ramp-down event is forecasted. Otherwise, it outputs zero. The position of the sun is determined by detecting "vertical" line of the sun, which is the artifact created by the CCD device which can be seen at Figure 8. The results show that the proposed prediction framework outperforms the work referenced, achieving a RMSPE of at least 3% less than the referenced work and a MAPE of at least 4% less, for 5, 10 and 15 minutes predictions.

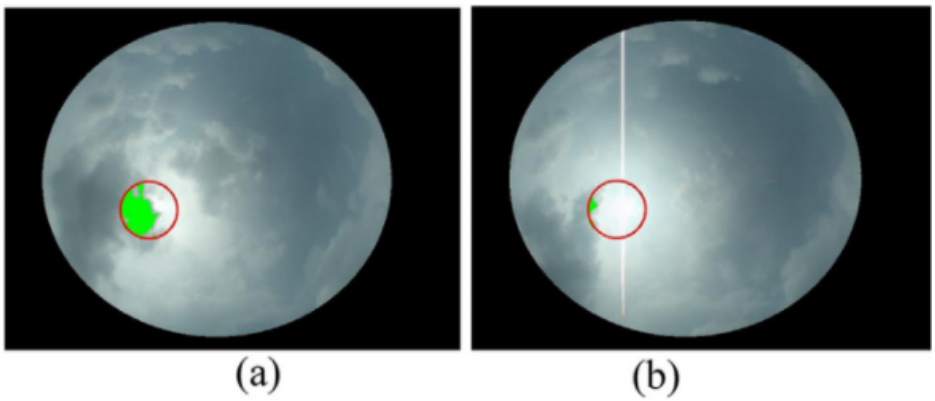


**Figure 8.** Sun position and region $\Omega$.

#### *1.4.2 Cloud-tracking methodology for intra-hour DNI forecasting*

The paper in [13] has direct normal irradiance data measured with the Eppley Normal Incidence Pyrheliometer (NIP) mounted on an Eppley SMT tracker at the University of California Merced's solar observatory. The sky images used in this work were obtained with the Yankee Environmental Systems Total Sky Imager (TSI-880) at the University of California Merced's solar observatory. The 3 channels RGB images were recorded every 20 s with a net resolution of 255x255 pixels. The sector method for cloud tracking is based on the use of a sun-centered circular grid over the projected masked binary Cloud Index (CI) images. The grid divides the images into several sectors as exemplified in Figure 9. The sun-centered circular grid is determined by 5 parameters that can be adjusted in order to optimize the accuracy of the cloud flow direction detection: number of sectors, number of rings, ring size, number of discarded inner rings and initial rotation angle. This algorithm computes the full cross-correlation. The correlation value, ranging from 0 to 1, is a measure of the degree of correlation between the two series, where higher values indicates higher correlation degree. Direct Normal Irradiance (DNI) is forecasted using the adjustable-ladder method. Using the selected grid elements the DNI forecasts for time horizons $\Delta t$ from 3 to 20 min are generated. The results show an overall RMSE of 105.26 and MAE of 63.30.

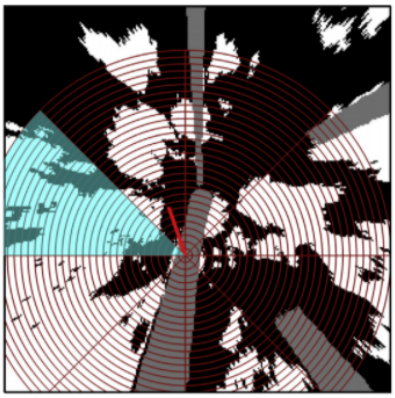

**Figure 9.** Sun-centered circular grid over masked projected binary Cloud Index (CI) image, where white areas represent clouds and black ones clear sky. Colored area represents the selected sector by the sector method. Solid red line indicates the cloud flow direction identified through the PIV algorithm.

#### *1.4.3 Predictions of cloud movements and the Sun cover duration*

In [14], the camera frame rate was set to 25 frames per second and processed every 100th or 300th image. Using BGR color model the initial cloud image is converted to image with predominantly red colors instead of blue colors. After the conversion erosion and dilation are performed with the image converted to black and white. In order to find contours corresponding to the edges of the clouds, the Suzuki contour tracing algorithm was used. In this paper, as a reference point for determining the movement of clouds, the centroid of every closed contour was chosen. Also, very small clouds were ignored and the centroid calculation was not performed. In order to determine velocity and direction of cloud movement, the spherical coordinate system is used. Angular velocity is determined by changes of azimuth and elevation. Since every 300th image of the video was processed, which means that the interval of cloud position analysis was performed every 12 seconds (300 frames / 25 frames per second = 12s). To accurately predict the duration of Sun cover with clouds, an approximation shapes of ellipse and rectangle were used (Figure 10 shows one cloud whose shape is approximated with ellipse and rectangle). Simulation the location of the Sun is performed by drawing a yellow filled circle at a given location in the image. The results presented are from two different measurements using either an ellipse or rectangle as the type of approximation with the error in prediction being measured at the start and end of covering for both types. Measurement 1 shows an error of 16.7% at the start and 1.3% at the end of covering for an ellipse and 16.7% for a rectangle. Measurement 2 shows 115.6% and 0.7% for start and end of covering for an ellipse and 102.1% and 4.39% for a rectangle, respectively.

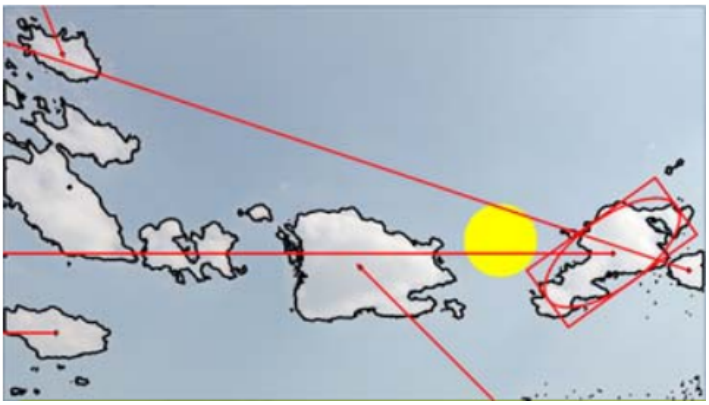

**Figure 10.** Approximation cloud shapes with ellipse and rectangle

#### *1.4.4 Short Term Cloud Coverage Prediction using Ground Based All Sky Imager*

In [15], the authors proposed a new sun occlusion prediction system. The system consists of data acquisition, cloud velocity estimation, sun location back propagation, cloud segmentation module and prediction module. In the absence of pyrheliometer/pyranometer. Sky images are captured at an interval of 5 seconds with Moonglow All Sky Imager. The camera is calibrated using the OcamCalib Toolbox with 11 checkerboard images. The images captured by the All Sky Imager are also projected

from image space (fish-eye) to sky-space (corrected lens). Sun position determination: The 3D world sun position is obtained from "The Astronomical Almanac" in terms of observation time and viewer's geographical location. 3D world sun position is then used to find corresponding position in the image space by extrinsic projection and camera model. To obtain this calibrated extrinsic projection matrix for mapping 3D world sun position to image space, 55 sun annotations from different time points are used. To predict the sun occlusion the authors model this problem as a binary classification problem between cloud and sky and use a linear support vector machines (SVM) to classify cloud and sky pixel with the following features: HSV color space, ratio of red and blue color channels, variance values and entropy values. They randomly sample 10,000 cloud pixels and sky pixels respectively for training from the annotated images. Remaining samples are used for testing in a cross validation like framework. The accuracy of classification is about 98.2%. Figure 11 shows an overview of the proposed system. The motion model for prediction is based on spatial regularized optical flow algorithm. The authors compute the flow between a pair of images at an interval of 5 seconds. They evaluated the above methods in the data collected at 755 College Road East, Princeton, NJ 08540, USA. Data was chosen to address "interesting cases" i.e with cloud coverage between 0 to 75%. Overall the data size covers 21 hours. The data used for the evaluation was collected during the months of March 2013 and April 2013. Even though the data is representative in terms of cloud coverage, there could be a bias in the data with respect to wind direction and speed due to a short period of data collection. Two baselines are used for comparison: the first one is random guess and the second is the persistent guess. The presented results show a comparison of prediction performance of both baselines. For up to 15 minutes at least one of the methods is better than both the baselines.

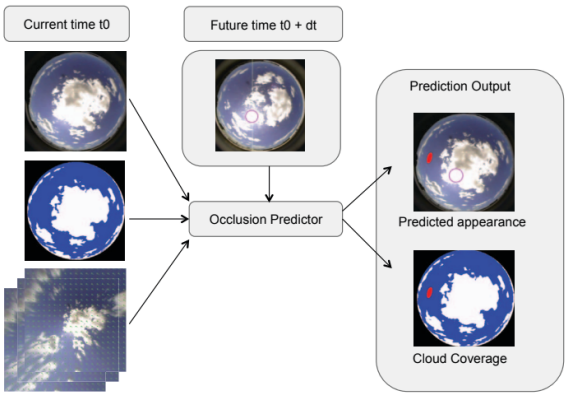


**Figure 11.** Overview of the prediction system.

#### *1.4.5 Short-term Solar Photovoltaic Irradiation Predicting Using a Nonlinear Prediction Method*

In [16], the cloud image is processed by LUM (Low-Up-Middle) filter firstly. Once the pre-process is finished, the image is divided into small blocks. And then, for each block the area of clouds is calculated by a modification method. Then, the difference of current and last image is distinguished and the motion of cloud is calculated. Lastly, the motion path is predicted by a nonlinear prediction method and then, the power of PV system is predicted with the historical data. The solution uses the sun's disk recognition and reconstruction methods. The resolution of cloud image is 4000x3000 and the image is divided into several grids. The arrayed sub-images are marked with numbers from 1 to N. To distinguish them, the blocks of clouds are calculated and the sub-images are ordered according to the minim distance between clouds and sun. To distinguish clouds of the sky, the authors use a modification technique. The feature of picture is described as a matrix and after steps of transmission, the parts of picture are classified into cloud and cloudless, as show in Figure 12. The change of clouds is a discrete process which is treated as a Markov chain which means the state of a system changing from one to another over time step. Generally, the states of clouds are determined to cloud and cloudless but considering the thickness of clouds the state of cloud is required to be many states. The real data is tested in Chengdu, capital city of Sichuan province and the predictive data is calculated by a computer using the temperature and irradiation data. Results show improvement in proportional error in the proposed method compared with traditional method.

#### *1.4.6 Solar irradiance forecasting using a ground-based sky imager developed at UC San Diego*

In [17], the UCSD Sky Imager (USI) captures images using an upward facing charge-coupled device (CCD) image sensor sensing RGB channels at 12 bit intensity resolution per channel. A 4.5 mm focal length circular fisheye lens allows imaging of the entire sky hemisphere. Although the CCD image sensor is capable of capturing images at a resolution of 2048x2048 pixels, the fisheye lens limits the image circle diameter to 1748 pixels. The USI does not employ a solar occulting device. The entire month of November 2012 was selected for detailed analysis. These 31 days provided a variety of sky conditions with which to

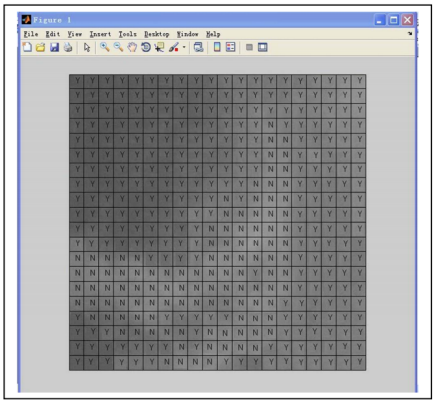

**Figure 12.** Classification of cloud and cloudless.

validate USI forecasts, including clear skies, marine layer overcast stratus and stratocumulus, passage of frontal systems, and partly cloudy conditions with low-level cumulus, mid-level altocumulus, and high-level cirrus clouds. USI forecasts can be broken into two steps: one which operates purely upon sky images, specifically cloud detection and cloud motion, and one which is specific to the location and equipment at the site of interest (as shown on the left side of Figure 13). Before image processing, each USI image pixel was calibrated to a geographic azimuth and zenith angle by leveraging the known position of the sun and the known projection function of the lens. Image quality control was completed by cropping to remove static objects on the horizon (buildings, trees, etc.), white balancing by a 3x3 color-correction matrix, and correcting for any known sensor errors. Image pixels were classified as clear, thin cloud, or thick cloud based on the ratio of the red image channel to the blue image channel, or red-blue-ratio (RBR). Thresholds were applied on the difference between the RBR of a specific pixel and the clear sky RBR of the same pixel. Cloud base height (CBH) measurements were obtained from METAR weather reports, which are typically generated once per hour (sometimes more frequently) from automated weather observation stations at airports. Cloud pixel velocity was obtained by applying the cross-correlation method (CCM) to the RBR of two consecutive. Irradiance forecasts were produced by determining the locations of ground shadows cast by clouds as defined by their location in each advected cloud map through ray tracing cloud maps. Two quantities were used to characterize the performance of image-based algorithms: matching error and cloud-advection-versus-persistence (cap) error. Four error metrics were used to assess the overall performance of the USI forecast system as a function of forecast horizon: relative root-mean-square error (rRMSE), relative mean absolute error (rMAE), relative mean bias error (rMBE), and forecast skill (FS). The results show an average matching error of 5.0 and 18.9 for 30 seconds and 5 minutes forecasting, while the cap error showed an average of 67.0 and 91.9 respectively. The graph of bulk error metrics as a function of forecast horizon for all 31 days is shown on the right side of Figure 13.

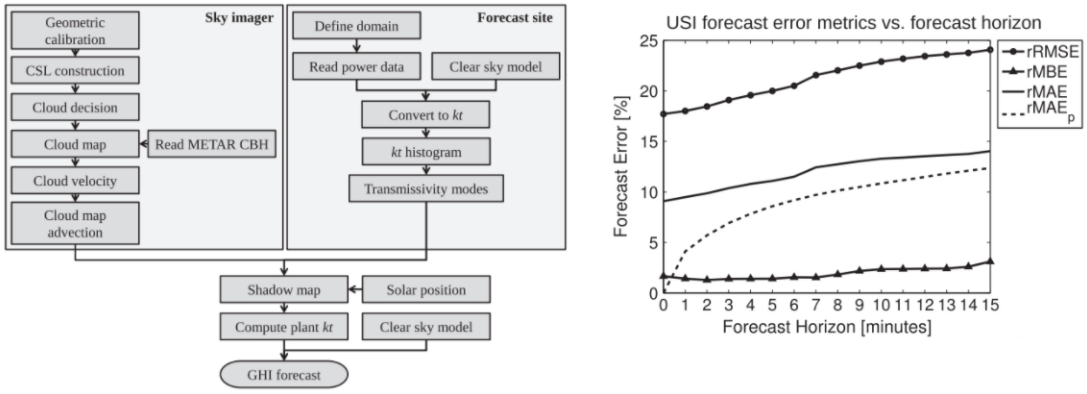


**Figure 13.** Left side: Flowchart of USI forecast procedure. Right side: USI error metrics for all 31 days in the November data set versus forecast horizon.

### 1.5 Continuous short-term irradiance forecasts using sky images

In [18] the author uses a pipeline of methods to predict the short term irradiance with images from a Sky Imager. In the first steps the author detects the motion vectors and segments the clouds. The Thirions "demons" algorithm to calculate the direction and speed of the clouds, in pixels, to generate the motion vectors, as we can see in figure 14. Then, the clouds are segmented using a Random Forest classifier, to classify if the pixel is from sky or cloud. The forecasting algorithm uses the segmented clouds and the cloud speed to predict if the sun will become occluded during the next 10 minutes in an area nearby the sun called dense motion field. Due to saturated pixels close to the sun, sparsity of the preliminary forecast and inaccuracies introduced in the previous steps, the forecast obtained from one cloud chart is not yet a reliable predictor of sun occlusion. Then a kalman filter, that takes information from previous forecasts, is used to increase the performance of prediction below 3 minutes, smoothing the overall forecast. The dataset used for the evaluation consists of continuous data collected over 15 days in June 2013, March 2014 and April 2014. The camera and pyranometers were installed near Kitzingen, in Bavaria, Germany. The acquisition of the pyranometer irradiance data is synchronized with the image capture, the data was recorded in 5s intervals.

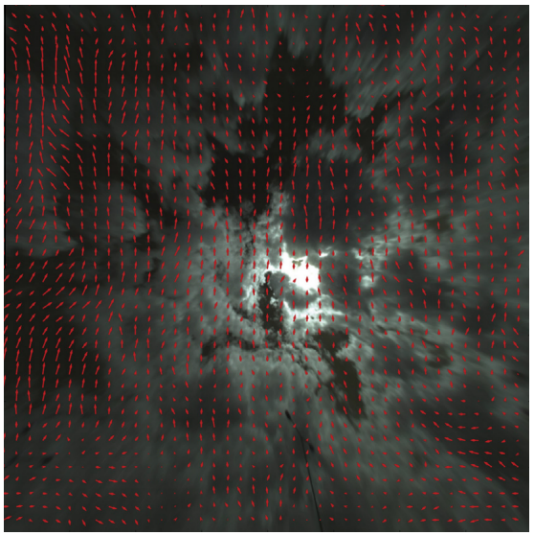

**Figure 14.** Example displacement vectors calculated with the "demons" algorithm (only every 20th displacement vector is shown).

### 1.6 2015

#### *1.6.1 A local features-based approach to all-sky image prediction*

In [19], an all-sky imager is used to take a series of cloud images. These images are subsequently calibrated to eliminate the distortion of the fish-eye lenses in the imager. The amera model is a Nikon D90 capturing raw images every 2 minutes with resolution of 2,144x1,424 pixels in JPEG format with 8 bits of depth. A dataset of 100 cloud images and 100 sky images from various weather conditions are manually collected. The data imply that red-blue difference (RBD) and color-invariance (CINV) give the most discriminative results. Because one single feature is insufficient to distinguish clouds from the sky, RBD and CINV are combined to form a feature vector as the input of the classifier. The features in every single image present a multi-Gaussian distribution; i.e., pixels representing clouds are close in the feature space, following a Gaussian distribution. By incorporating the distribution model of each image in cloud detection, an Adaptive Gaussian Mixture Model (AGMM) is proposed. In this model, the pixels in each image are grouped into certain clusters according to the feature values of each pixel. Clouds and sky can be described using the sum of corresponding Gaussian components. For the cloud matching the authors adopt a nearest-neighbor ratio matching strategy. The kd-tree with Best Bin First search is used to quickly search the closest and second closest neighbors. Only if the ratio between the Euclidean distance of the closest neighbor and the second closest neighbor is lower than a pre-defined threshold, this match is accepted. In the approach, a hierarchical coarse-to-fine motion model is presented, which is a decomposed form of affine transformation. Particle Filtering, used after the hierarchical motion model, consists of two steps: prediction and correction. A database including 100 images is constructed to evaluate the performance. The images are calibrated, and the sizes are normalized into 600x600 pixels. They divide the images into 20x20 sub-blocks. Each block is manually labeled as cloud or sky as a whole. Three linear classifier-based methods are compared in the experiment. Two linear classifiers with RBD and CINV are trained separately. Additionally, a new model using Linear Discriminant Analysis is applied. As illustrated Figure 15, the proposed AGMM method is more adaptable to variation of

weather conditions than the other three works are. In order to evaluate the prediction performance of this proposed method, a long series of real-time image sequences including 280 continuous images were collected as the evaluation dataset. The time interval between two consecutive images is two minutes. The distribution of clouds is forecasted from 2 to 14 minutes. The SAIPS exhibits desired results for two to ten minutes prediction, yielding over 82.23% average precision (AP) over the forecast periods of 2, 6, 10 and 14 minutes, which is an improvement above the all of the compared methods (Block-based, No Bayesian filtering and Kalman filtering).

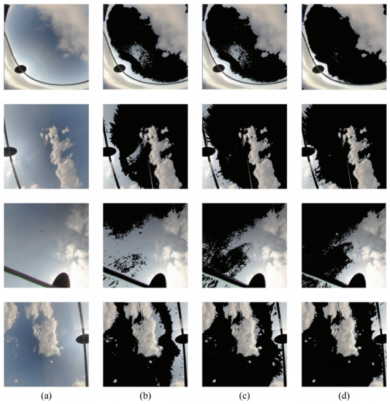


**Figure 15.** Examples of cloud detection results compared with other methods. (a) Original images. (b) Results of segmentation using threshold on Red-Blue-Difference. (c) Results of segmentation using linear classifier on both Red-Blue-Difference and Color Invariance. (d) The final results of the proposed algorithm.

#### *1.6.2 An ultra-short-term power prediction model based on machine vision for distributed photovoltaic system*

In [20] the authors used a Pan-tilt-zoom (PTZ), which equipped with CCD industrial camera tracks the sun automatically with time step of 30 minutes from sunrise to sunset. The moving data of the sun over the year in Hangzhou, China are calculated by astronomical formulas and location of latitude and longitude of photovoltaic power plants are calculated. The angle change of solar movement is slow, combined with the requirement of stepper motors step angle subdivision and tracking precision. So the system tracks the trajectory of the sun every 30 minutes. The features that cause the severe change of power output of PV system are the position and the shape. The position of clouds is represented by the centroid of clouds. For a timing series of cloud images, starting at $0^o$ polar angle with step of $3^o$, 120 sample points can be obtained in the polar coordinate in each image. Connecting these points predicts the clouds shape in the near future. Predictions of centroid position and shape change are made for the timing cloud image. Through image processing, the predicted outline of the $t_4$ moment with actual $t_4$ moment stacked in one window, as shown in Figure 16. The actual $t_4$ moment image subtracts the common part with the predicted image resulting in Figure 16(b), in which the area of white zone is 75.75. The predicted image subtracts the common part with the actual image resulting in Figure 16(c), whose area is 56.38. The different partial image between the predicted and the actual image is shown in Figure 16(d), whose area is 132.13. The area of cloud in actual $t_4$ moment is 2441.60. The deviation rate is $132.13/2441.60 = 5.4\%$.

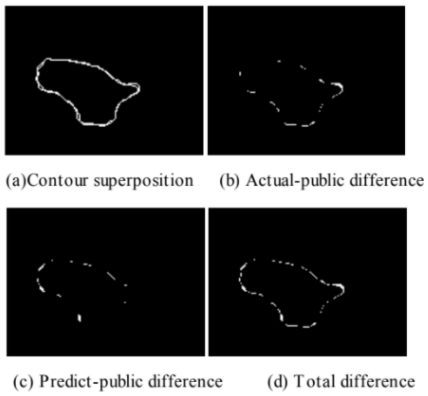


**Figure 16.** Contrast figure between predicted $t_4$ and actual $t_4$

#### 1.6.3 Cloud motion and stability estimation for intra-hour solar forecasting

In [21], a sky imager developed at UC San Diego mainly consists of a charge-coupled device (CCD) image sensor with 12 bits intensity resolution in each RGB channel, a 4.5 mm circular fisheye lens, and a neutral density filter. The USI utilizes high dynamic range (HDR) imaging and outputs lossless PNG images with a bit depth of 16 bits per channel, a dynamic range of 81 dB, and a useable size of the image of 1748x1748 pixels. Images were processed to remove the distortion caused by the fisheye lens, resulting in red–blue-ratios (RBRs) in a Cartesian coordinate system at the predetermined cloud height. Images were not considered if they were clear (cloud fraction <5%) or overcast (>95%). In this research, the algorithm by Liu (2009) is used due to its simple implementation, relatively low computational intensity, and flexibility in parameters. The nowcast (i.e. 0 min forecast) is obtained by shifting the cloud map at time $t_0 - dt$ ($dt = 30s$ throughout this analysis) with the motion vector field determined from the variational optical flow (VOF) and cross-correlation method (CCM) applied to the images at time $t_0$ and $t_0 - dt$. To determine accuracy, the actual cloud map at time $t_0 + n * dt$ is overlaid onto the advected cloud map to determine the pixel-by-pixel forecast error. This matching error ($e_m$) between the two cloud maps is the ratio between the number of falsely forecasted pixels and the number of total pixels in the image. The cloud-advection-versus-persistence (cap) error is applied to measure if cloud advection improves over a naïve image persistence forecast. The forecast skill (FS) is defined to measure the improvement in the matching error of the VOF forecast compared to the CCM forecast. Point trajectories are obtained by developing an optical flow tracker. Tracking of a point is terminated if one of the following three circumstances is encountered: point is advected out of the forecast domain; forward and backward optical flow yield inconsistent results; the image structure around the trajectory point decreases. Figure 17 shows an example image demonstrating the ability of the optical flow technique to capture the non-uniform cloud motion. The VOF forecast was found to be superior to CCM forecast for with an average error reduction of 39%, 21%, 19%, and 19% for 0, 5, 10, and 15 min forecasts respectively. While image persistence outperformed VOF forecast for forecast horizons of 5 and 10 min on 2 out of 20 days these days were associated with highly variable clouds.

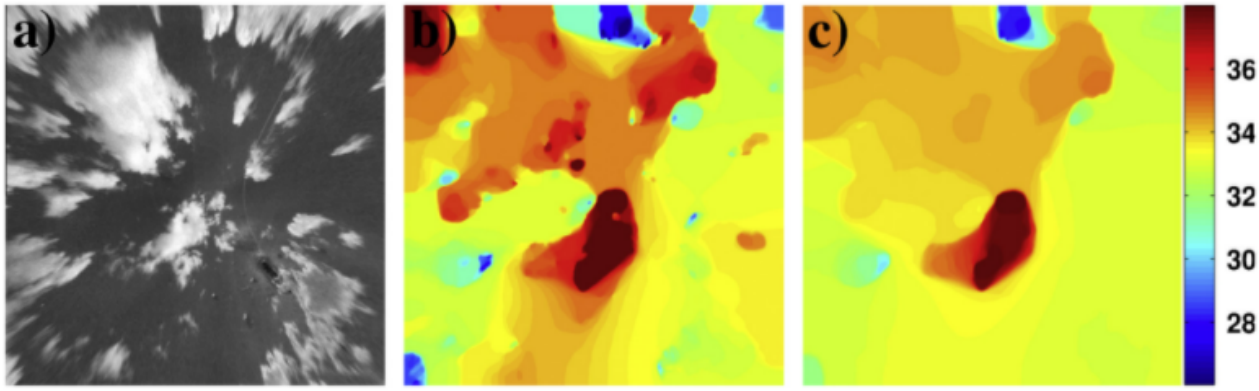


**Figure 17.** Optical flow estimation of the residual RBR image on November 10th, 2012, 08:46:00 PST out to zenith angles of 75° (a) with spatial smoothness $\alpha = 0.01$ (b) and $\alpha = 0.1$ (c). The colorbar indicates the motion magnitude in pixel per frame.

#### 1.6.4 Multi-model solar irradiance prediction based on automatic cloud classification

In [22], cloud classification is performed based on features extracted from the blocks. To extract the characteristics of textures, three different local pattern descriptors are considered in this work, including the LBP (Local Binary Pattern), the LTP (Local Ternary Pattern), and the LDP (Local Derivative Pattern). PCA (Principal Component Analysis) is performed to find the principal axes of data. Then, the feature vector is input into a trained classifier to determine the class label of the block. The classifier utilized in this work is the SVM (Support Vector Machine) with RBF (Radial Basis Function) kernels. In this paper, the authors classify the images as six classes, which are cirrus (class 1), cirrostratus (class 2), scattered cumulus or altocumulus (class 3), cumulus or cumulonimbus (class 4), stratus (class 5), and clear sky (class 6). The prediction models are established using regression functions. Both MLR (multiple linear regressor) and SVR (support vector regressor) are tested and their performance are analyzed. The experimental dataset contains the all-sky images and corresponding ground truth irradiance readings of 28 days. The dataset is collected at a costal site in Taiwan. We use all-sky images captured by the all-sky camera manufactured by the Santa Barbara Instrument Group (SBIG). The images are stored in bitmap format with resolution 640x480 pixels. One all-sky image is captured per minute. The device used to measure the ground truth solar irradiance is Delta OHM LP RYRA 03. It is a point sensor located next to the all sky camera. The sampling interval is 10 s. The measured solar irradiance within each minute is averaged to generate the ground truth irradiance data corresponding to each all-sky image. When performing dimensionality reduction using PCA, a threshold needs is selected to determine the number of dimensions that is preserved. The authors evaluated the five-fold cross-validated classification accuracy on 1500 blocks of size 60x80

pixels with manually labeled class labels to select the best threshold. To select the best block size, five different block size configurations are considered in experiment: 50x70, 60x80, 70x90, 80x100, and 90x110. The block size of 60x80 pixels yields the best cross-validated classification accuracy. Selected cloud classification results are displayed in Figure 18(a)-(d). For quantitative results of the irradiance prediction accuracy, the authors calculate the cross validated relative mean absolute error (rMAE) and relative root mean square percentage error (rRMSE). They use four-fold cross validation to calculate rMAE and rRMSE. For each fold, data from one week is used to train the regressor and the data from the other three weeks is used for testing. Then, the training and testing datasets are rotated and the statistics are averaged. Results shows that MLR generally yields slightly lower prediction error than SVR. The proposed multi-model prediction approach outperforms the bi model approach proposed with both rMAE and rRMSE lower using the proposed method in all intervals of forecasting (5, 10 and 15 minutes).

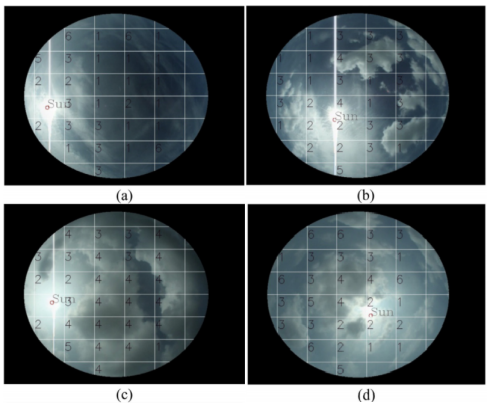


**Figure 18.** Selected cloud classification results.

#### *1.6.5 Real-time forecasting of solar irradiance ramps with smart image processing*

The authors in [23] collected irradiance data using 2 Multi-Filter Rotating Shadowband Radiometers installed at observatories in Folsom and San Diego, California. Sky images are obtained from 2 fisheye cameras installed next to the MFR-7s. Six months (January 13, 2013 to July 10, 2013) of historical irradiance and sky-imaging data were collected in Folsom for the training of the stochastic component of the integrated solar forecasting platform (ISFP). The real-time forecast produces 10-min forecasts of global horizontal irradiance (GHI) and direct normal irradiance (DNI). The authors develop a smart adaptive cloud identification system (SACI) to conduct cloud detection for images captured by the fish-eye cameras used in this experiment. Firstly, each sky image is categorized as clear or cloudy using five criteria computed from past 10-min GHI time-series. Secondly, if the image is categorized as cloudy, the hybrid thresholding method is used to analyze red blue ratio histograms and further categorize the image as either overcast or partly cloudy. Thirdly, after the image categorization, the SACI employs Fixed threshold method for overcast images, clear sky library method with fixed threshold for clear images, and clear sky library method with adaptive threshold for partly cloudy images (examples are shown in Figure 19). The proposed method employs multilayer preceptron neural networks (MLP). The training process is the Bayesian regularization process with Levenberg–Marquardt optimization using clear-sky indexes 10 min afterward as the training targets. Cross validation method (CVM) is employed to prevent over-fitting of the MLP. They employ the GA to identify the optimal MLP scheme that achieves the smallest validation RMSE and four statistical metrics to assess the performance of the ISFP: the mean biased error (MBE), root mean square error (RMSE), forecasting skill (s) and excess kurtosis. Both persistence and ISFP models show small MBE (less than 5 $w/m^2$ ). In terms of RMSE and forecasting skill s, ISFP outperforms the persistence model. The higher forecasting skill is attributed to the combination of cloud tracking and stochastic learning. Improvements over the persistence model are in the range of 6.0–11.3% depending on location and irradiance component. The ISFP results show smaller excess kurtosis than persistence model. The MLP-based ISFP produces fewer instances of large errors and more instances of moderate errors than persistence model, resulting in an error distribution with shorter tail and rounder shoulders,resulting in a smaller kurtosis.

#### *1.6.6 Solar irradiance forecasting at one-minute intervals for different sky conditions using sky camera images*

In [24], the authors used a total sky camera with a rotational shadow band (namely a TSI 880 model) for solar irradiance estimation in real time. The hemispheric vision was represented in JPEG images, with a 352x288 pixel-image resolution. All images were collected over one-minute periods when the solar altitude (in degrees) was higher than 5, with a frequency of 3 times a week and irradiance data for each minute. The authors use cloud motion vectors to determine the pixel motions following a referenced methodology where the image is split into different sectors to study the cloud motion of each, shown

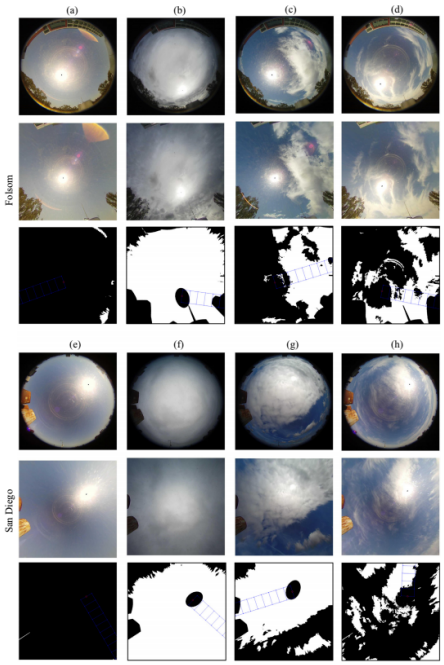


**Figure 19.** Examples of SACI cloud identification. Sky images for Folsom: (a) clear period (2013-08-05), (b) overcast period (2013-11-19), (c) partly cloudy period with optically thick clouds (2013-10-06), and (d) partly cloudy period with optically thin clouds (2013-11-11). Sky images for San Diego: (e) clear period (2013-12-30), (f) overcast period (2014-01-30), (g) partly cloudy period with optically thick clouds (2014-02-09), and (h) partly cloudy period optically thin clouds (2013-12-01). The first and the fourth rows present the original images, the second and the fifth rows present the projected images, and the third and sixth rows present the detected binary cloud maps with the grid elements.

in Figure 20(a). By applying the Maximum Cross-Correlation method, the cloud motion vector is calculated for each sector. The cloud detection is carried out on the last image collected containing the most recent information about sky conditions. To do this, the digital image levels are used to identify the clouds at the pixel level. After processing the image to identify the clouds, the next step was to obtain an irradiance value for each pixel. The authors created a methodology for estimating solar irradiance shows the main task developed to obtain the estimation (Figure 20(b)). Depending on the pixel position in the image, the digital levels have different values, being brighter in the sun area than in the rest of the image. For this reason, the image was divided into three spherical parts. For each type of sky condition and for each area, correlations between different image channels and the solar altitude were analyzed and the best correlations were those that showed less dispersion with respect to irradiance data. The Cloud Motion Vector (CMV) is applied to the last image received, from 1 to 180 times, representing the pixel motion from the first minute until the 180th minute. Once obtained the solar irradiance estimation at pixel level and the cloud motion vector (Figure 20(c)), the solar irradiance forecasting for the short and medium-term is carried out. For the results the authors used data from the years 2010 to 2014. Each day, a solar resource prediction was made every 15 min from 1 to 180 min. They classified the sky, by analyzing the DNI values, into three categories: cloudless, partially-cloudy and overcast. For cloudless sky the beam irradiance forecasting, nRMSE values present very constant results, starting at a value of 20.81% for 1 min, slightly higher from prediction to 2 h and having a value of 25.99% in 180 min. Under this sky condition, irradiance is often underestimated, from 16.24% for 1 min until 18.35% for 180 min, while the R value decreases linearly throughout the forecast period. For Partially-loudy sky the nRMSE value remains very constant over the forecast period, obtaining a value of 20.90% for 1 min and 28.88% for 180 min with a gentle rising trend. The nMBE value indicates an irradiance underestimation, with very stable values that oscillate between 7.70% and 9.16%. The value of R undergoes a decrease from 0.84 to 0.58 from 1 min to 180 min. For overcast sky the nRMSE value for beam irradiance shows a slight progressive increase in the forecast time, where the value is 12.64% for the first minute, reaching a value of 19.87% for 180 min. The nMBE value indicates an overestimation of 5.28% for the first minute of prediction and 10.42% for 180 min, demonstrating a slight increase over the forecast time. Meanwhile, the R value has a downward trend, starting at a value of 0.82 for 1 min, and ending at a value of 0.76 for 180 min.

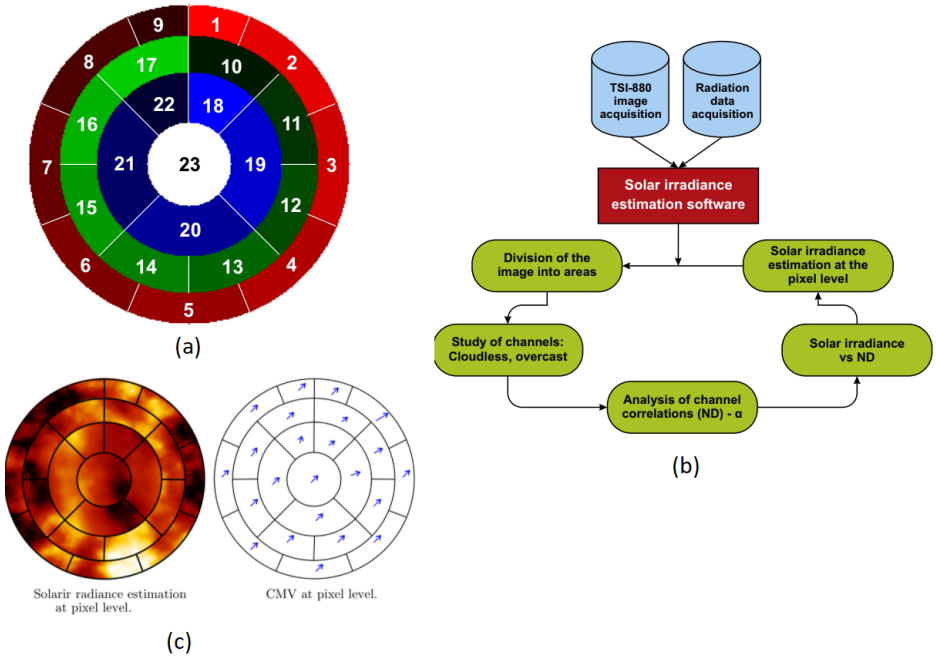


**Figure 20.** Sector divisions for sky-camera images (a). Flowchart of the process used to obtain the solar irradiance estimation (b). General representation of the two processes involved in the solar irradiance forecasting (c).

#### *1.6.7 3D cloud detection and tracking system for solar forecast using multiple sky imagers*

The work from [25] describes an methodology to forecast short-term solar irradiance using multiple total sky imagers. The work uses 9963 images, from each one of three cameras, from May 13, 2013 to June 03, 2013 and global horizontal irradiance from 25 pyranometers to validate its method. The images have a resolution of 640 x 480 pixels and an image is recorded every 10 seconds. A pipeline for the cloud detection is showed on figure 21. First, a supervised classifier, Support Vector Machine, was used to detect pixels from the cloud. The classifier was trained with characteristics from the cloud pixels like: red channel, green channel, blue channel, red to blue ratio and feature bases on pixels neighborhood. The mask generated by the classifier was also used to compute the histogram of the 3 cameras and identify if a device has an abnormal histogram, so that it can be adjusted. The cloud pixels are aggregated in blocks, to reduce the sensibility to noise and changes in luminance, using a block-matching algorithm that finds the best blocks between two frames. The generated blocks were used to find the 3D coordinate and motion from each block of clouds. Each cloud have three different views, one from each sky imager, and those views can be combined to estimate the height using a stereography approach. An algorithm was developed to simultaneously incorporate both spatial and temporal correlations to improve the accuracy of the block-matching methodology. This algorithm makes it possible to stitch multiple images together to increase the forecast horizon, because they can track the same cloud from different cameras views. To forecast the radiation, first they needed to identify the positions of the 25 pyranometers on the images to calculate when a cloud will block its measurement. An 7x7 sun-blocking window was used to reduce the risk of false prediction, along with 23 significant features that described the spectral variation inside this window, like: maximum, minimum and average from rgb channels. To test the predictive capabilities of the selected features, they explored four different irradiance models that use a subset or all of these features to generate a regular linear regression or more complicated non-linear relationships: linear RBR delta, linear regression model, Support Vector Regression based on a linear kernel and SVR with a non-linear kernel. All of the proposed methods reduced the prediction errors, compared to the persistent model, for forecasts up to 15 minutes.

The author proposes a four regression-based solar irradiance model, that uses predicted features from cloud pixels and compare with a Support Vector Regression and a persistent model.

#### *1.6.8 Solar Irradiance Forecasting Using Multi-Layer Cloud Tracking and Numerical Weather Prediction*

In [26] a pipeline to handle complex cloud scenarios is proposed. The clouds are tracked using a method composed by multiple steps. In the preprocessing step the images from the sky are undistorted then the shadowband and camera holding arm are masked. A cloud cover map, to distinguish pixels from sky or cloud, is generated using a Suport Vector Machine with pixel values, red to blue ratio and laplacian of gaussian. Then, an k-means clustering algorithm was used to identify the height of the

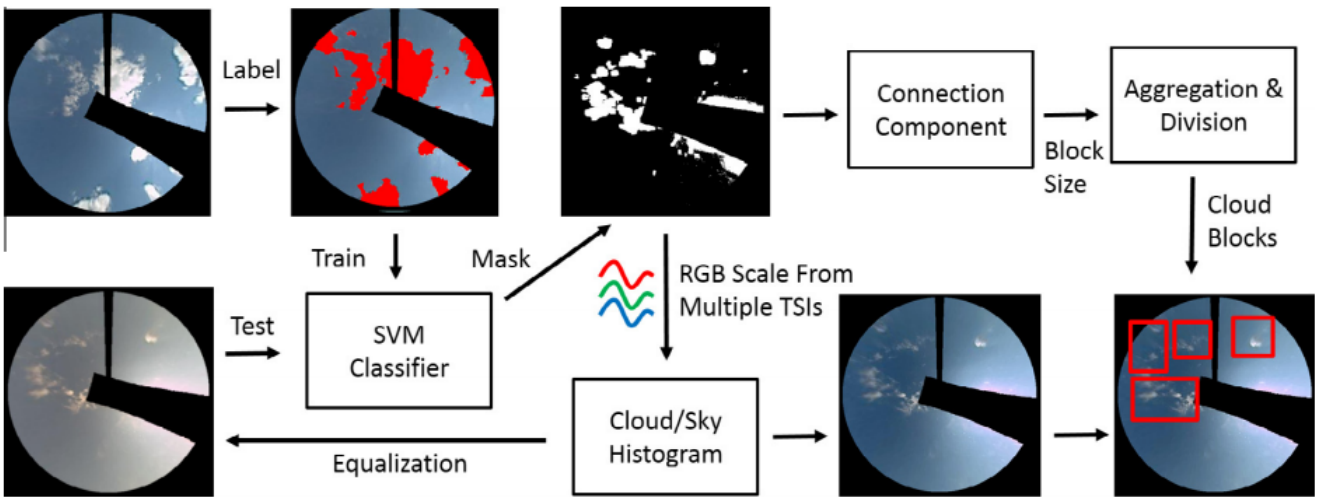


**Figure 21.** Pipeline for cloud detection using an SVM classifier and multi-source correction.

clouds. The steps of the pipeline can be seen on figure 22. The cloud tracking method was calculated by a cross-correlation algorithm. The author compares three different models to forecast the irradiation: Persistent Model, Linear Regression and Support Vector Regression. The Support Vector Regression model showed consistent better performance. The data used on the experiments consists of 20 days between may and July of 2013.

## 1.7 2016

### *1.7.1 A hybrid approach to estimate the complex motions of clouds in sky images*

In [27], the authors propose a new hybrid approach that integrates the block-matching method and the variational optical flow (OF) model, and uses the former method to guide/refine the latter one. The pipeline consists of a Support Vector Machine (SVM) based binary classifier. To comprehensively train the classifier for different imagers, theh authors selected four images representing four distinct cloud conditions, scattered clouds, cloudy, overcast, and clear sky, for each sky imager, manually label all cloud pixels, and extract six features for each cloud/sky pixel: R, G, B, red-blue-ratio, Laplacian of Gaussian, and the standard deviation value around the pixel's neighborhood (5x5 in use). The SVM classifier recognizes cloud pixels under various cloud/lighting conditions with the accuracy of 96.6%. Lastly they apply the classifier to generate a cloud mask for sky images where "1" stands for cloud pixels and "0" represents non-cloud pixels. To suppress image noise and neglect falsely estimated motion vectors, the proposed method identifies the dominant patterns of cloud motions and uses them to refine the entire motion field. In the experiments, the authors empirically use one as the threshold of vector length to remove small-scale motion vectors. A new OF model is proposed where they apply three filters thereafter to further assimilate cloud information, utilize dominant motion patterns, and remove noise in the motion field. An iterative algorithm is designed to generate and optimize the dense flow field and to update the subsequent reference motion vectors. To validate the effectiveness of the proposed model, a comprehensive simulation framework to incorporate translative cloud motions, cloud deformation, and various levels of noises into the synthetic sky images is established. Three different two-frame sequences of synthetic images from a cloud template (foreground) and a real sky image (background), each of which represents image noises or a different type of cloud motion were generated. The authors adopted five metrics to quantitatively evaluate the performance of the proposed model of estimating cloud motions and to compare it with several representative models: optical-flow color map; average angular error (AAE); standard deviation of angular error (STDANG); average end-point error (AEPE); mean absolute error (MAE). The proposed Hybrid model consistently outperforms other models in most cases in terms of three different metrics, (AAE, STDANG, and MEPE). For the most difficult case of simulating deformation (i.e. $A = 5$; $S = 32$), Hybrid retains the lowest level of errors in terms of AAE and MEPE and the second to the lowest in terms of STDANG, which is only 5% higher than the best score obtained by the large-displacement optical flow model. To validate the accuracy of detected motion vectors, the authors applied the resulting motion field between two consecutive frames ($t-1$ and $t$) to predict the next frame ($t+1$) and to compare it with the true image. In Figure 23, the first row lists the raw data of three frames at time $t-1$; $t$; $t+1$ (ground-truth) and a motion mask to remove outliers and calculate the MAE score. The second row presents the motion fields of BM, MPIV, BA, and Hybrid respectively. The third row shows the predicted images using detected motions and image interpolation. The fourth row displays the color maps of the difference between the predicted images by the four models and

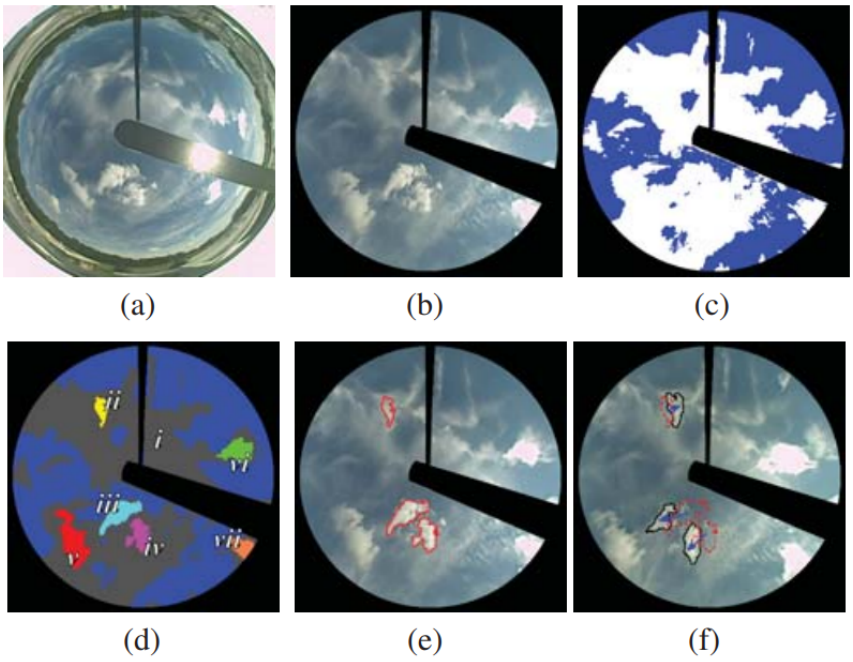


**Figure 22.** Cloud tracking steps. (a) Original image. (b) Image undistortion and shadowband dispatch. (c) Cloud cover. (d) Multi-layer detection and cloud segment identification, where colors represent individual clouds. (e-f) Cloud segments at time t are outlined in red in (e) and their corresponding predicted motion vectors are superimposed on the time t + 1 image in (f); clouds from time t are dashed for reference.

the ground-truth frame at time $t+1$.

#### *1.7.2 Estimation of solar irradiance using ground-based whole sky imagers*

In [28], measurements are taken continuously on various rooftops of the Nanyang Technological University (NTU) in Singapore. The devices comprise three Whole Sky Imagers and three weather stations. The authors use a Canon DSLR camera, a Sigma fish-eye lens and a single board computer. They deployed three WAHRSIS (Wide Angle High-Resolution Sky Imaging System) at NTU, which capture sky/cloud images at intervals of 2 minutes. They also use the Davis Instruments 7440 Weather Vantage Pro II, which collects temperature, humidity, dew point, pressure, surface wind speed and direction, rainfall rate, solar radiation, and solar energy at one minute intervals. A square patch of a fixed size around the sun from the image is cropped. The position of the sun in image is detected by setting a threshold of 240 in the red channel of the image. The centroid of the largest generated polygon from thresholding is considered as the sun's position in image. Then the mean luminance of the cropped image is computed by averaging the luminance channel of the image in the HSL (Hue, Saturation, Lightness/Luminance) color space. The aperture and ISO are kept constant, and only the exposure time varies. In order to fix the cropped patch size, the authors measure the correlation between solar radiation and luminance for different crop sizes around the sun. Experiments using 563 images on a typical day of December 2015 are performed and results are presented in Figure 24. The optimal performance for a size of 300 x 300 is obtained, which is selected for the subsequent experiments. The authors test the proposed algorithm for a large period of time, for all days in the month of December 2015. They claim to observe a strong correlation (Pearson correlation coefficient of 0.93).

#### *1.7.3 Forecasting variation of solar radiation and movement of cloud by sky image data*

In [29], the authors collect images every 30s with 1440 images taken every day by a EOS-60D Canon camera with fisheye lens. In the study a ceilometer is used to collect bottom height and cloudiness data, with observations divided into three layers (low, middle and high). The estimation of moving direction is done by color analysis. If the color variation of the moving cloud coincides with the search direction, the color variation per unit time difference is considered to be similar. Using the cloud image data obtained simultaneously at points A and B, the azimuth of point A and B are calculated. When the value of the estimated solar radiation was less than $0.3 kW/m^2$, the lower limit value correction of the solar radiation was calculated by using the brightness obtained from the all-sky image data as show in Figure 25. The relation between the brightness and solar radiation was calculated by the least squares method. To forecast the variation of solar radiation, the cloud image data taken at SFS and AIT are used. The forecasted results present an average error of 3.5% between the observed and the estimated values.

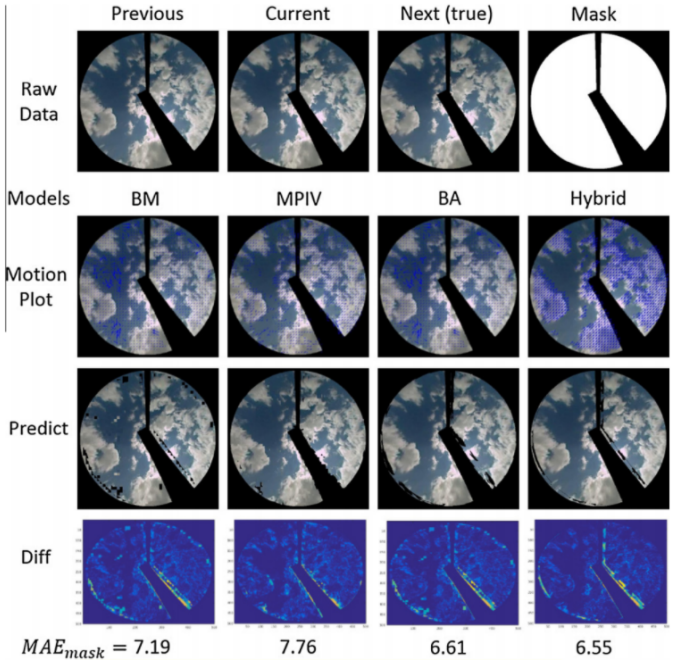


**Figure 23.** Framework of synthesizing two-frame sequence of sky images.

The forecast method was also performed in a different location to confirm its generality and it achieved similar results with 3.3% average error.

#### *1.7.4 Sky Status: A Local Analysis of Ground based Digital Images*

In [30], the sky images were acquired by a digital camera with a resolution of 8Mp. Images of the database were taken in different times with different states of clouds near the sun zone (clear sky, partially cloudy and totally cloudy). The authors compared the obtained sun status and the output of solar panels and to implement the proposed solution, an electric assembly system powered by 50 Watts peak PV panel was created. This embedded system, measures the power generation with an optimal panel orientation, and simultaneously acquires the sky image. The acquired image is converted from RGB color space to HSV color space. For each image, the sun zone is segmented then its surrounding area. The average intensity is computed and then a result providing the brightness difference between the two areas is achieved. Furthermore, it is noticed that the measured power increases proportionally to the brightness difference and vice-versa. The experimental results (Figure 26) show that the proposed process helps to detect the sun position and its status. Figure 26 shows (A) great value of Db: corresponds to clear sun then maximum power generation; (B) middle value of Db: corresponds to partially cloudy sun then average power generation; (C) low value of Db: corresponds to cloudy sun then low power generation.

#### *1.7.5 Utilization of Low Cost, Sky-Imaging Technology for Irradiance Forecasting of Distributed Solar Generation*

In [31], the sky images are taken on the rooftop of the Energy Systems Integration Facility Building (ESIF) at the NREL Facility - USA, using a fish-eye lens camera with a resolution of 1024x768. Due to the camera design, the fish-eye lens captures images in direct sunlight causing over exposure. To bypass this, the system incorporates an exposure fusion operation, to capture images at different exposures and fuse them together. Once the fused image is created, a mask is applied by image “addition”. The initial stage of cloud detection uses a standard approach based on a “Red to Blue Ratio” procedure. A simple threshold is applied to each pixel to thereby change the image from grayscale to binary, with the clouds represented as the color white and the sky represented as the color black. The process to orientate images is performed as a calibration step. The set of images that were acquired at the ESIF facility required a rotation around 170 degree. At its most basic level, the clouds from the binary images created are tracked using a technique called optical flow. With the current image and its feature points defined, the next step is to take an image after a given time-lapse and detect another set of feature points. With both past and present images obtained, the optical flow procedure takes place. With optical flow defined, it is applied towards the binary sky images. By using the head of the individual vectors, the cloud area is then transitioned across the image for each prediction interval. This optical flow method is used to help in disregarding clouds that begin to merge with others or disappear over the time period that is under analysis. Utilizing the cloud base heights and zenith angles of the sun, the region of interest from the cloud motion predictions are found using trigonometry. The graphs in Figure 27 highlight the measured direct solar irradiance (DSI) for five

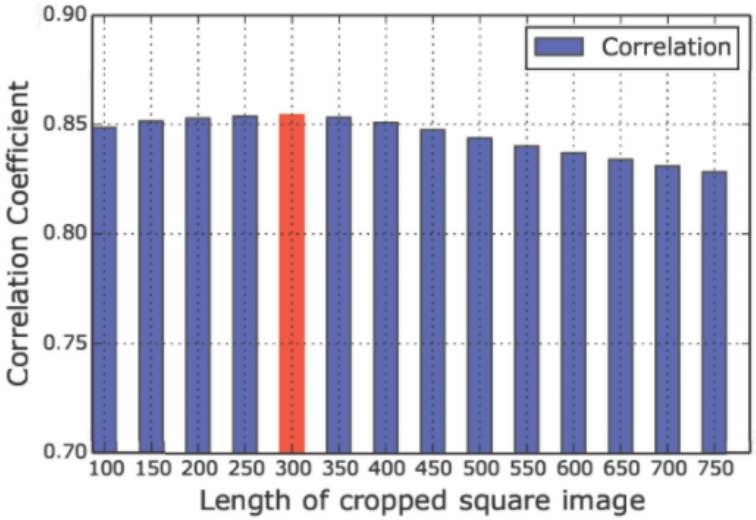


**Figure 24.** Impact of image patch size on correlation. Best performance is obtained for a crop size of 300 x 300 (redbar).

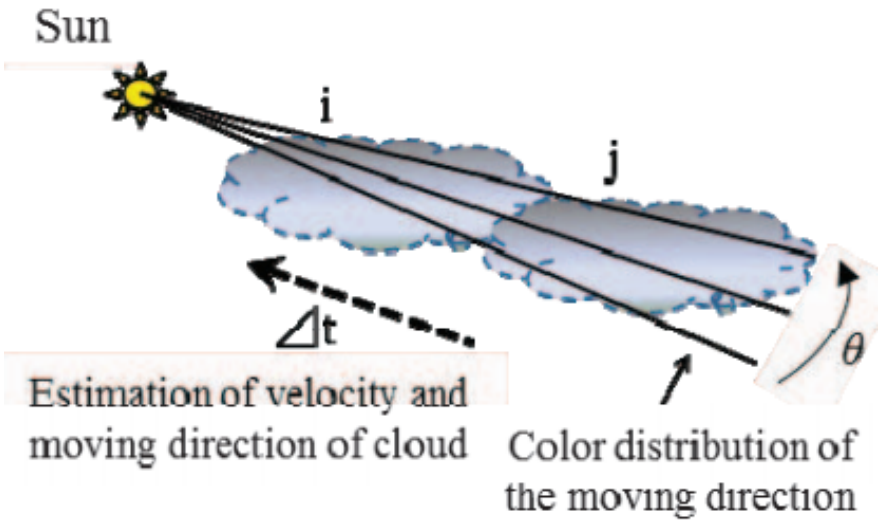


**Figure 25.** Estimating method of moving status of the clouds by using color distribution analysis.

different days that exhibited a variety of irradiance profiles. The measured DSI values were recorded using NREL's CHP1 Pyrheliometer. Also included in these graphs are the forecasted, irradiance spikes generated by the methodology presented. The results show that the day with least errors occurred on 11-15-15 and 11-18-15. These days were fairly clear with few clouds moving through the area.

## 1.8 2017

### *1.8.1 A virtual sky imager testbed for solar energy forecasting*

In [32], Large Eddy Simulations are carried out using the UCLA LES which has been thoroughly validated and tested for a number of cases including continental cumulus, raining cumulus, and stratocumulus clouds. The Spherical Harmonic Discrete Ordinate Method (SHDOM) is used to solve the 3D Radiative Transfer Equation. SHDOM is the most computationally intensive portion of the virtual testbed, requiring over half of the approximately 5000 CPU-core-hours. The sky imager forecast models clouds as occurring in a single plane at the height of the cloud base. Current cloud positions are detected based on the color of the input image, and future positions are forecast using the "frozen cloud advection" assumption, which assumes that the entire cloud field moves in a uniform direction without changing shape. Inputs to the sky imager forecast are a sky image, cloud base height usually derived from lidar data, and recent measured GHI—used to estimate average cloud optical thickness, which is difficult to determine from the image. Figure 28 illustrates data flow through the sky imager forecast algorithm, along with

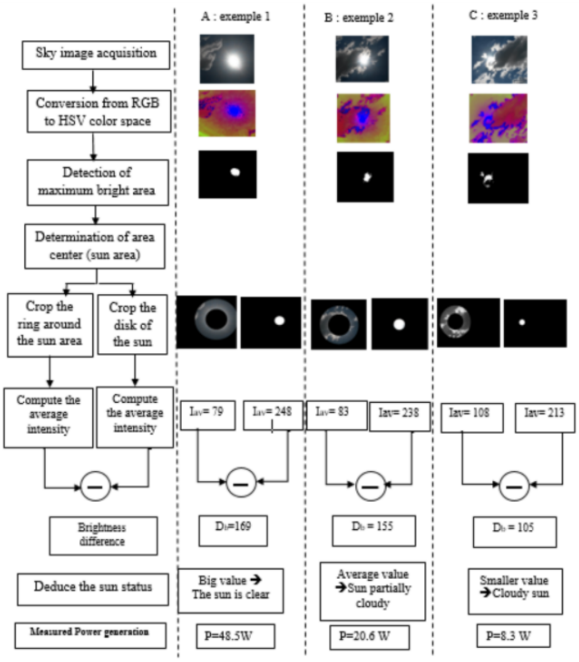


**Figure 26.** Algorithm steps and examples.

inputs from the virtual testbed. Cloud detection operates on the virtual sky images in the same manner as real sky images, and classifies each pixel of the input image as clear sky, thin cloud, or thick cloud, by applying thresholds to the difference between the red-blue ratio (RBR) of the image being analyzed and RBR of a clear sky. Reference optical depth maps are computed using three different geometries zenith projection, sun projection, and converging-rays projection. The sky imager forecast computes cloud speeds based on pixel motion between adjacent frames. Motion vectors are determined for small regions of the image, and then clustered and averaged to produce a single wind vector that will be used to advect the entire cloud field. The final step of the forecast is to place cloud shadows and estimate GHI$(x, y, t)$. During the simulation run, the sky imager forecast had errors (RMS) of 2.0 m/s and 1.7 degrees for the detected cloud velocities compared to LES wind at the cloud base height. Considering multiple cloud classes, 83% of pixels were correctly classified, with 7% that were classified as a cloud of the wrong class, and the remaining 10% classified as clear when they should have been cloud or vice versa. Detected $k_t$ values from the existing histogram-based method were also relatively reliable, with errors (RMS) of 0.033, 0.078, and 0.079 for clear, thin, and thick categories.

### *1.8.2 Battery-Less Short-Term Smoothing of Photovoltaic Generation Using Sky Camera*

In [33], the spherical perspective of the sky-image is projected onto the flat plane using the OCamCalib calibration toolbox. The undistortion is conducted so that the poorly undistorted region with higher circular angle is projected outside the destination frame. A computational approach is deployed, which yields the angular position of the sun corresponding to the specific geographic information, date and time. The fish-eye coordinates of the sun is obtained and then translated into undistorted coordinates using the calibration toolbox. Cloud segmentation is done by applying an ordinary thresholding on the RBR value of the pixels usually shows an unreliable performance in different regions of the sky. Therefore, a collection of clear sky images is created, where each element corresponds to a specific zenith angle considering the daily and seasonal variations of the sun trajectory. TThe sky image and the respective clear sky reference (CSR) are undistorted and averaged block-wise and the corresponding RBR value is calculated for each block instead of pixel-wise processing. The thresholding process produces a binary cloud mask representing the clear sky in zero and clouds in one. The shape of the clouds is defined in a sequence of the coordinates on the outline of the respective area termed as “contours”. An optical-flow approach is deployed to identify the motion of the objects between two successive frames. It calculates an array of two-dimensional displacement vectors respective to all pixels or blocks of pixels. The vectors are then filtered by the binary cloud mask Figure 29 to obtain the motion elements of the pixels inside the cloud regions. In order to make a more reliable prediction, which is less susceptible to occasional errors in segmentation and optical-flow, a series of historical observations are incorporated. The principle of the proposed smoothing method-I is to estimate the projected solar insolation according to the predicted cloudiness indices. The angle of incident for the direct component of the solar irradiance can be obtained using the coordinates of the sun generated by the

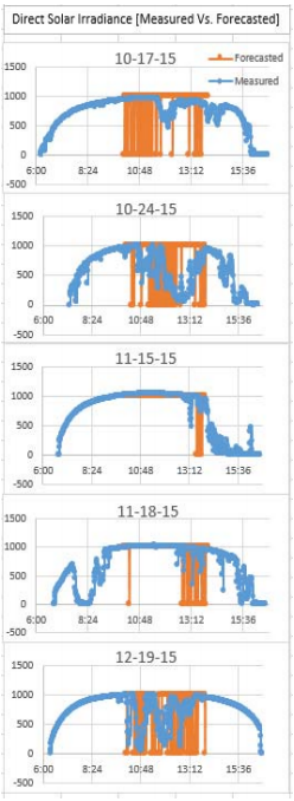


**Figure 27.** DSI for measured and predicted values on five separate days.

solar positioning procedure and alignment of the PV array. Therefore, a rough approximation of forecast values are obtained. The proposed method-II approach slowly lowers the export power into a reduced value during the critical situations when it is highly likely that solar occlusion occurs and ramps that up when the clouds are passed. This is determined by the projected cloudiness figures. A preliminary trial experiment was conducted at Magellan Power in Western Australia, including different meteorological conditions, i.e., fully sunny, overcast, and partly cloudy. The experimental results are also compared with the associated results of the conventional non-predictive smoothing strategy simulated in MATLAB/Simulink.

#### *1.8.3 Cloud Motion Tracking for Short-Term On-Site Cloud Coverage Prediction*

In [34], the authors focus on doing the preliminary pre-processing required to predict the irradiance variation. As the irradiance level is in direct correlation with how much is the sun covered by the cloud, here a cloud motion tracking and cloud motion prediction method were introduced. The sky images are the most dominant input information. For this work, the ground-based sky images were taken using a fish-eye lens camera with a resolution of 1024x768 pixels. The images were captured at every 10 seconds and were stored in JPEG. format. The camera white balance property is a tunable parameter and it was set to 6500 considering sunny sky condition. The cloud detection uses the masks created considering foreground objects and a simple RGB color threshold algorithm. The two methods implemented used Red to Blue ratio based thresholding approach and the difference between Blue and Red component of the image. The sun's position on the image was located using zenith angle, azimuth angle, camera orientation, camera properties, date and time. The whole cloud was tracked in the proposed approach and in order to find correspondence of each cloud in each frame, fast normalized cross-correlation was used. The cloud feature points were found to identify cloud deformation and to find cloud moving velocity. To find the cloud feature points Harris feature detection algorithm was used. Then the authors use the Lucas-Kanade optical flow on feature points to find feature point moving velocities. Using the feature velocities of five consecutive image frames, 3min ahead cloud position was predicted. Figure 30 a) shows the tracked cloud boundaries with 3min ahead predicted cloud boundary (blue) and Figure 30 b) shows the predicted cloud boundary 3min ahead (Brown) and actual cloud boundary (Blue).

#### *1.8.4 Cloud tracking for solar irradiance prediction*

In [35], the authors calculate the sun location in the image view based on the Solar Position Algorithm (SPA) and camera calibration. They follow Jean Meeus's algorithm to precisely calculate the solar zenith and azimuth angles, and convert the sun location to pixel coordinates in the sky image using calibrated camera. They also use a wide angle lens to ensure full sun

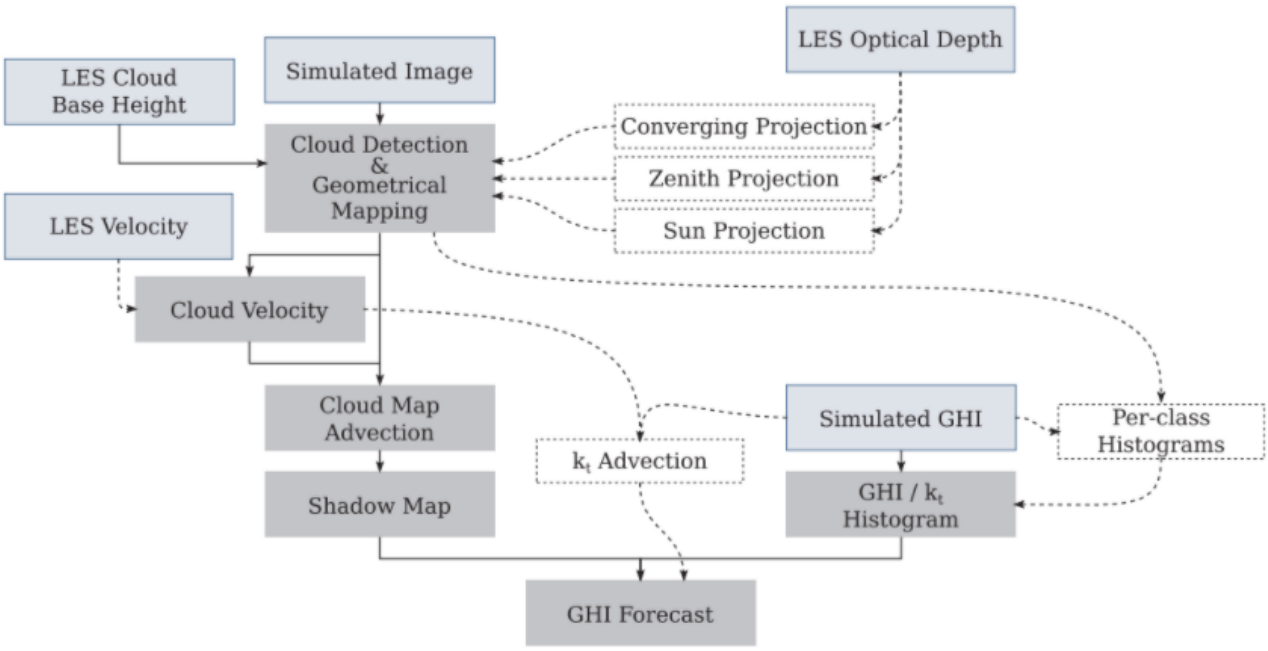


**Figure 28.** Data flow through sky imager forecast algorithms with inputs from virtual testbed. Solid arrows indicate the standard flow of data through the algorithm, while dashed lines show where "correct" data from the virtual testbed can be used in place of a step in the forecast algorithm. Outputs of LES or SHDOM are shown with a thin solid outline, while derived results have a dashed outline; steps in the basic sky imager forecast have no outline.

coverage throughout the day. Thus fisheye rectification is performed, such that linear velocity models can be assumed for cloud motion prediction. The OCamCalib is used to calculate the rectification from a set of checker board images, where both the radial and de-centering distortions are estimated via nonlinear optimization. Camera intrinsic and extrinsic parameters are derived by minimizing the re-projection errors of the image grids. The authors describe an empirical rule-based, probabilistic approach to per-frame cloud pixel analysis for joint segmentation and classification. Using the Horn/Schunck optical flow the displacement is calculated for fine pixel grids between consecutive frames, thus the raw estimated velocity is mostly noisy. To this end, the velocity estimation from a larger boundary region for robust estimation is aggregated. To obtain a robust solar occlusion estimation, the constraint that, the prediction of an occlusion event that will cause solar irradiance drop is accumulated for more than sufficient number of consecutive frames is enforced. The predicted irradiance drop is the averaged over all pixel-wise estimations where, for each category, a fixed weighted amount of irradiance drop when a sun occlusion occurs, is assigned. The authors collected sky video sequences using a Nikon camera with resolution 1936x1296 and an irradiance sensor to collect groundtruth simultaneously at a frequency of one sample per second. Figure 31 reports results on a longer sequence about 7.6 hours at 0.1 FPS.

#### *1.8.5 Machine Learning versus Ray-Tracing to Forecast Irradiance for an Edge-Computing SkyImager*

In [36], high resolution (1024x768) all-sky images are acquired using a Raspberry Pi Camera. Three images at different exposure times are captured and fused together to produce a High Dynamic Range. Cloud base height (CBH) is obtained from ceilometer measurements from the nearest airport. Zenith angles are determined from NREL's solar position and intensity calculator, SOLPOS. Parameters determined by a camera calibration are used to correct for the nonlinear distortion of the fish eye lens. Mathematical transformations are applied to correct for this distortion. Then images are cropped and masked so that only pixels corresponding to the sky remain: obstructions such as terrain or buildings near the horizon are removed. To determine which pixels represent low level clouds, the "Red-to-Blue Ratio" (RBR) is used. A median filter is applied to the grayscale image, and finally thresholding transforms the image from grayscale to binary. The physical model used in the forecasting, it assumes that the base for all low level clouds is the lifting condensation level or CBH as measured by a ceilometer. For periods of time when the sky is completely clear or totally overcast, the algorithm uses persistence. A moderately cloudy sky condition with 15%–70% cloud cover is indicative of air-mass cumulus clouds. In this case, cloud motion tracking by optical flow is used to predict future cloud locations, and then ray-tracing is employed to forecast shadows and GHI. The SkyImager software uses Lucas–Kanade approach to calculate the optical flow motion vectors. A ray-tracing approach to

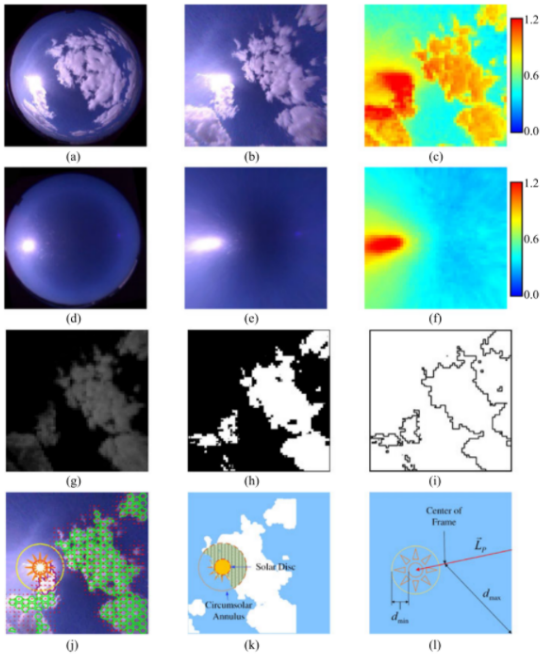


**Figure 29.** Real-time captured image (a) fish-eye, (b) undistorted, (c) RBR in false color. Reconstructed clear sky image, (d) fish-eye, (e) undistorted, (f) RBR in false color. Cloud segmentation, (g) differential image, (h) thresholded , (i) cloud contours. (j) Cloud motion. (k) Cloud Forecast. (l) Observation ranges and effective range of displacement prediction.

locate shadows was chosen early in the design cycle, and while it did not perform significantly better than persistence, reasons why are clear. The Denver airport is 36mi from Golden and frequently there are missing entries in the METAR observations. Moreover, the focus on low level cumulus clouds both ignores the fact that there can be multiple layers of different cloud types, and necessitates a binary cloud/no-cloud classification with its attendant loss of information. Specifically, converting to binary images before feature extraction and optical flow means that much of the rich information content contained in the original RBG image is lost. The neural network software used for the preliminary comparisons is the Multilayer Perceptron (MLP). Two subimage sizes were used: 128x128 and 64x64. The training set consisted of 2465 subimages — one day's data from the SkyImager taken on 27 Oct 2015 at the NREL facility. As shown in Figure 32 the number of neurons in the hidden layer is varied with a corresponding variation in the runtimes. The accuracy achieved during the training of the network is poor, as expected. The results involve only one day's data and the network is having to "learn" the diurnal variation of the GHI, the clear sky irradiance, as well as how different types of cloud layers — cumulus, altocumulus, and cirrostratus — affect the irradiance. The authors present only the training results.

#### *1.8.6 Towards the short-term forecasting of direct normal irradiance using a sky imager*

In [37], the database is derived from measurements realized in Perpignan - France, at the PROMES-CNRS laboratory, using a Rotating Shadowband Irradiometer (RSI). The clear-sky DNI is measured using the empirical model proposed by Ineichen and Perez. The PROMES Sky Imager (PSI) consists in a 4-megapixel colour camera equipped with a fisheye len with images collected every 20 seconds at a resolution of 2048x2048 pixels, with 10 bits per channel. HDR imaging consists in merging several images, taken at different exposure times, such as every pixel is correctly exposed in at least one image. The merging process is as follows: first, for each image, over and underexposed pixels are removed. Then, a linear regression analysis is performed on the remaining pixels in order to map their values according to a reference frame. Finally, a weighted average of valid pixel values is used to generate the high dynamic range image of the sky. Five different exposure times are used. At the end, the composite image has a dynamic range located at around 100 dB. The normalized red-blue-ratio (NRBR) feature was selected because it allows the visual contrast between sky and clouds to be improved. In addition, it is known to be robust to noise. The algorithm developed for cloud detection takes inspiration from the classification algorithm proposed by Ghonima et al. when clear-sky anisotropy is known and from the hybrid thresholding algorithm proposed by Li and Yang. An adaptive threshold, calculated using the Otsu algorithm, is applied to the NRBR feature. In all other cases, a fixed threshold is applied to that feature. The two persistence models assume that DNI and the clear-sky index persist over the forecast horizon, respectively. The third model included in the comparative study is a deterministic model based on the fractional cloud cover ($F_c$). In the last

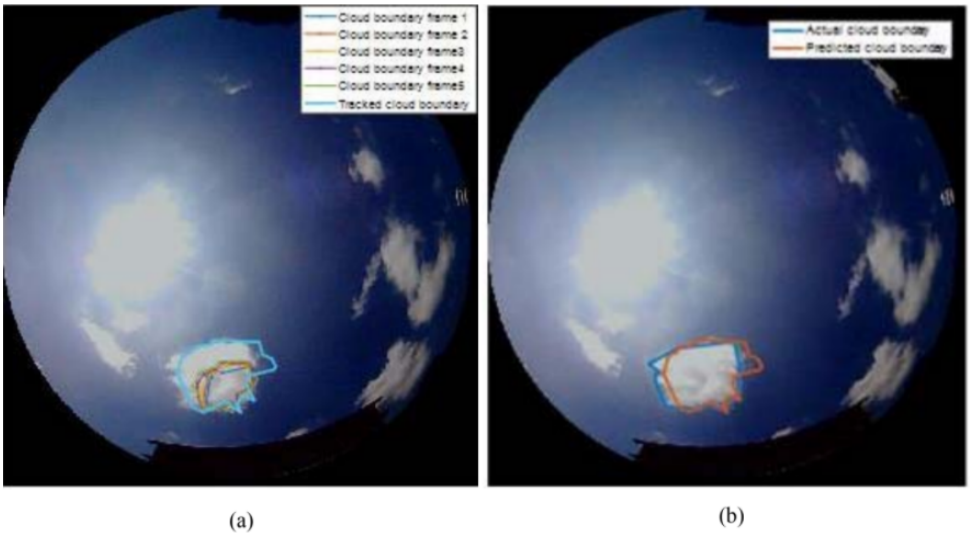


**Figure 30.** (a) Blue color boundary shows the predicted cloud boundary (b) predicted cloud boundary (Brown) and tracked cloud boundary (Blue).

model, an adaptive network-based fuzzy inference system is used to forecast the clear sky index ($k_c$) over the next 30 minutes. The model that relies on a persistence of direct normal irradiance is the simplest model included in the comparative study, having access to real-time measurements of DNI is the only requirement. The apparent movement of the Sun being known, one can try to take its effect on direct normal irradiance into consideration, therefore the persistence of the clear-sky index is calculated. The Adaptive Network-based Fuzzy Inference System (ANFIS) uses as inputs the clear-sky index ($k_c$) at time $t$, the fractional cloud cover ($F_c$) at time t, and $\Delta t_f$. The authors used a training set composed of 40 days, a validation set composed of 20 days, and 20 consecutive days to test the model. The learning process has allowed 8 fuzzy rules to be designed, for a total of 56 parameters in the system. As shown in Figure 33, we can note that the ANFIS model outperforms the other models in terms of forecasting accuracy, whatever the forecast horizon. Both persistence models have more or less the same accuracy. Taking one of these models as reference, RMSE is reduced of about $30 W m^2$ using the ANFIS model. Regarding the deterministic model based on $F_c$, it outperforms the persistence models for $\Delta t_f$ higher than approximately 11 minutes.

#### *1.8.7 Very short-term prediction model for photovoltaic power based on improving the total sky cloud image recognition*

In [38], a cloud extraction method based on the solar facula elimination and piecewise linear transformation cloud feature enhancement algorithm is proposed. In order to improve the efficiency of the algorithm, the authors only work with nephogram containing clouds. In the processing of nephograms, the discrete Fourier transform (DFT) is adopted. Therefore, after Fourier transform, cloud changes can be analysed according to characteristics of the original image in the frequency domain. In the application of cloud judgement, DFT algorithm can greatly reduce cloud misjudgement of degraded nephogram on haze weather conditions, compared with thresholding methods. To remove the solar facula the solar image and declination angle are first located. According to the statistical empirical results, the imaging radius of the general solar facula in the nephogram will not exceed one-third of the effective imaging diameter of the nephogram. Therefore Gray scale histogram statistics are applied only to the circular area covering the solar facula. The gray distribution region of the original nephogram is divided into three sub areas in the figure, and each sub-section is taken a different linear transformation according to the need of cloud recognition, and the gray detail of the cloud cluster is stretched. Based on the piecewise linear transform algorithm, RGB three channels palette of the original image are adjusted separately and then merged again. In order to improve the adaptability of the algorithm, the authors use the intensity slicing technique based on gray histogram of nephograms to realise the recognition of cloud cluster for different cloud background. The improved cloud extraction algorithm proposed in this paper is compared to the conventional threshold extraction method and adaptive cloud extraction method. Then the very short-term prediction model for photovoltaic power based on RBF neural network and ground-based cloud images for verification is chosen. This forecasting model has good following characteristics, and the prediction accuracy is higher in 0–15 min time scales, but for longer time scale prediction assessment requirements, the effect of cloud extraction has great influence on prediction results. The authors selected the 1 h scale. The data used for verification comes from a 20 MW photovoltaic power station in northwest China which was incorporated into power grid in 2013 July, this station equipped with TSI-880 all sky imager. The authors selected data of March 24, 2017 to verify the model. That day was cloudy and has a slight haze according to them. The authors

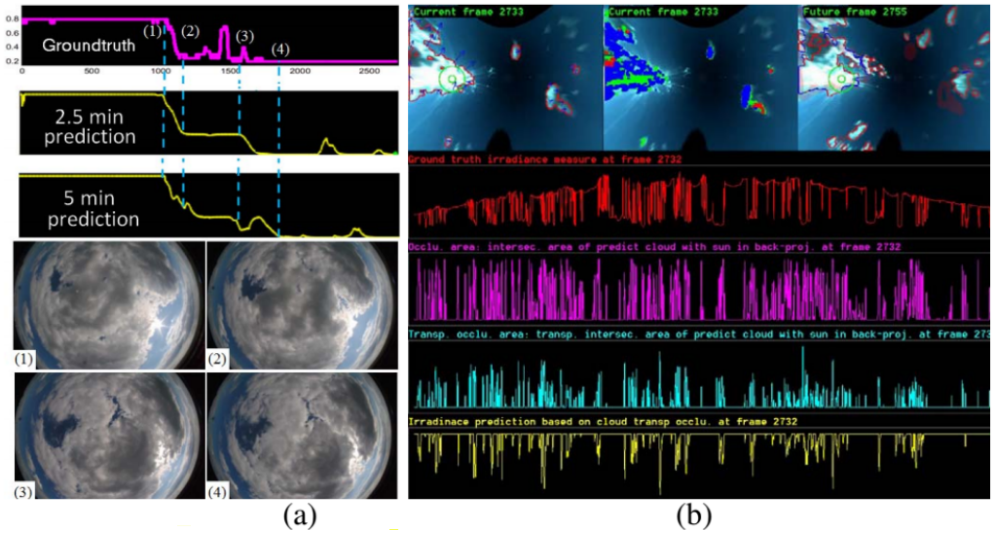


**Figure 31.** Comparison between the recorded groundtruth and predicted irradiance measures for (a) a 40-minutes sequence at two predictions of 2.5 minutes ($\Delta t = 150s$) and 5 minutes ($\Delta t = 300s$), where (1-4) depicts observed images. (b) a 7.5-hours sequence recorded at 0.1 FPS. The first view shows the input image with detected cloud boundary and the optical flow motion field. The second view shows the cloud segmentation with estimated transparency classes. The third view shows the future frame, the calculated sun mask and the predicted cloud boundary. Red curve depicts ground truth. Pink curve depicts the interaction-area based occlusion. Cyan curve depicts the interaction-area considering cloud transparency. Yellow curve depicts the sun irradiance drop estimation curve.

| Image Size | # Samples | # Hidden | Runtime | Accuracy |
|---|---|---|---|---|
| 128 × 128 | 2465 | 50 | 202 min | 31.77% |
| 64 × 64 | 2465 | 200 | 38 *min* | 25.88% |
| 64 × 64 | 2465 | 100 | 19 *min* | 31.44% |
| 64 × 64 | 2465 | 50 | 11 *min* | 25.35% |

**Figure 32.** Training results of the Multilayer Perceptron.

chose three different cloud recognition methods to compare and verify the effectiveness of the proposed algorithm. Method 1 is based on the local threshold interpolation method. Method 2 is based on the red blue ratio threshold method which is used in the very short-term prediction model proposed by Zhibao. Method 3 is based on cloud recognition algorithm proposed in this paper. Method 1: As is shown in Figure 34(a), due to the impact of haze, the accuracy of cloud recognition is poor, and cloud threshold is not obvious and not unified, so the algorithm is not very effective and the prediction results are not ideal. Method 2: As seen in Figure 34(b), the prediction accuracy is improved and cloud recognition in different period is enhanced mainly due to the variable threshold for contour extraction. However, inaccurate cloud boundary extraction leads to inaccurate calculation of the time scale of photovoltaic power stations covered by cloud, and many nephograms have been identified as invalid. Method 3 (Figure 34(c): this method has better applicability; the method was evaluated by calculating the error statistic parameters. The evaluation indexes of photovoltaic power prediction errors mainly include root mean square error (RMSE), mean absolute error (MAE) and correlation coefficient (R). Method 1 has an RMSE of 16.7% whereas Method 2 has 9.38% and the proposed Method 3 has 6.23%. The respective MAE is 2.75, 1.51 and 1.04 and correlation coefficient of 0.921, 0.930 and 0.954.

#### *1.8.8 Research on a cloud image forecasting approach for solar power forecasting*

The work from [39] uses multiple process to forecast the solar power. The first step uses a Otsu method to detect the cloud pixels in the sky. The second, a mathematical description of cloud location, shape and deformation is calculated. The last step applies a genetic algorithm to predict the cloud deformation based on the historical cloud information, that process can be seen in figure 35. Then the forecasting is generated using linear extrapolation with the data from the previous steps. The data used on the work were obtained from a EKO sky camera installed in Yunnan province of China.

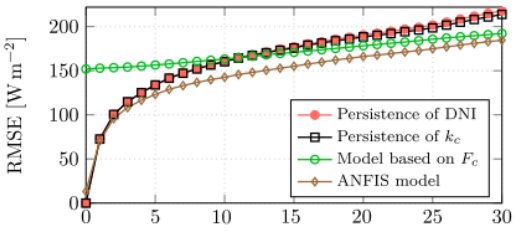


**Figure 33.** Forecasting accuracy. RMSE as a function of the forecast horizon ($\Delta t_f$).

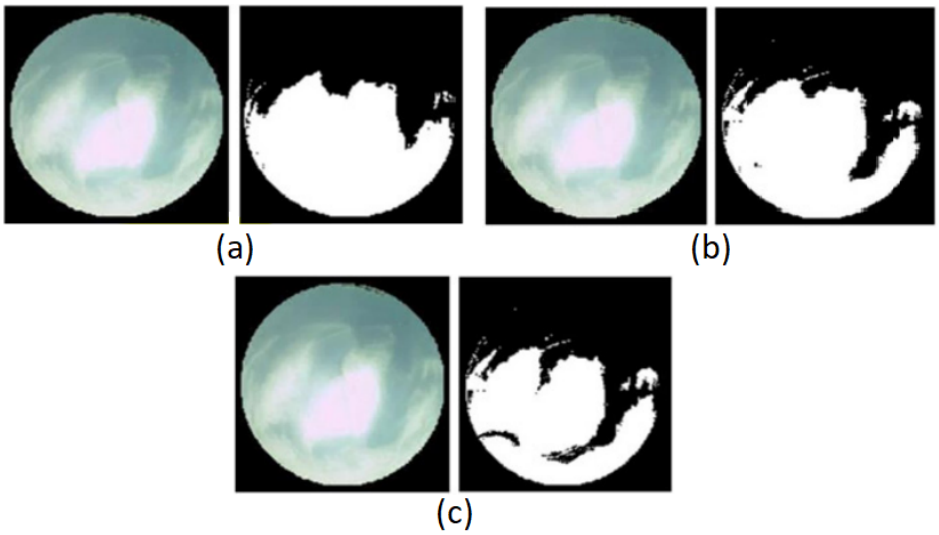


**Figure 34.** Cloud recognition results of Method 1 (a), Method 2 (b) and the proposed Method 3 (c).

#### *1.8.9 Cloud tracking using clusters of feature points for accurate solar irradiance nowcasting*

The work from [40] uses an algorithm based on feature points to identify and track the clouds. Those points are detected using harris corner detector and clustered on groups using the author max-min enhanced clustering algorithm, as we can see in figure 36. Feature points are used to calculate the motion vector of the clouds that are used to forecast obscuration and ramp-down events. To predict the obscuration events, the sun position is calculated by an algorithm using the zenith, location and time. Motion vectors and sun position are used to train a SVM classifier to predict the obscuration event. The ramp down event is predicted using two markov chain models with the data generated by the previous algorithms. The experiment was evaluated with a dataset from all-sky images and irradiance data from Taiwan. The impact of providing clustering information in the obscuration event detection process was tested with an experiment that uses feature point tracking information without clustering when constructing the feature vector. It was verified that performing clustering and including clustering information in the feature vector can enhance the detection accuracy. Also, the proposed clustering method was compared with the classic max-min clustering to see its impact on the obscuration event detection results. With the proposed clustering algorithm that improves the clustering results, the obscuration event detection accuracy is also improved.

### 1.9 2018

#### *1.9.1 A low-cost two-camera sky-imager ground-based intra-hour solar forecasting system with cloud base height estimation capabilities working in a smart grid*

In [41], the proposed method for dynamic creation of clear sky (CS) RBR images first evaluates the conditions of the original input RBR image and then creates a CS RBR image according to the former. Solar position is calculated using NREL's Solar Position Algorithm (SPA), using geographical coordinates of the location and time as inputs. Then, solar position is converted from real space (defined by its solar azimuth and zenith) to image space (polar or Cartesian coordinates). The algorithm fails to detect darker clouds, lighter clouds. Other problematic situations occur when sun is near the edges of the image. The optical-flow method used was the Gunnar-Farneback dense OF. The authors don't perform undistortion of the fisheye images. Cloud trajectories are modelled as ellipses that have their major-axis aligned with the predominant direction of the clouds. An estimation of an elliptic trajectory for each point contained in each contour of the clouds mask is made by finding the

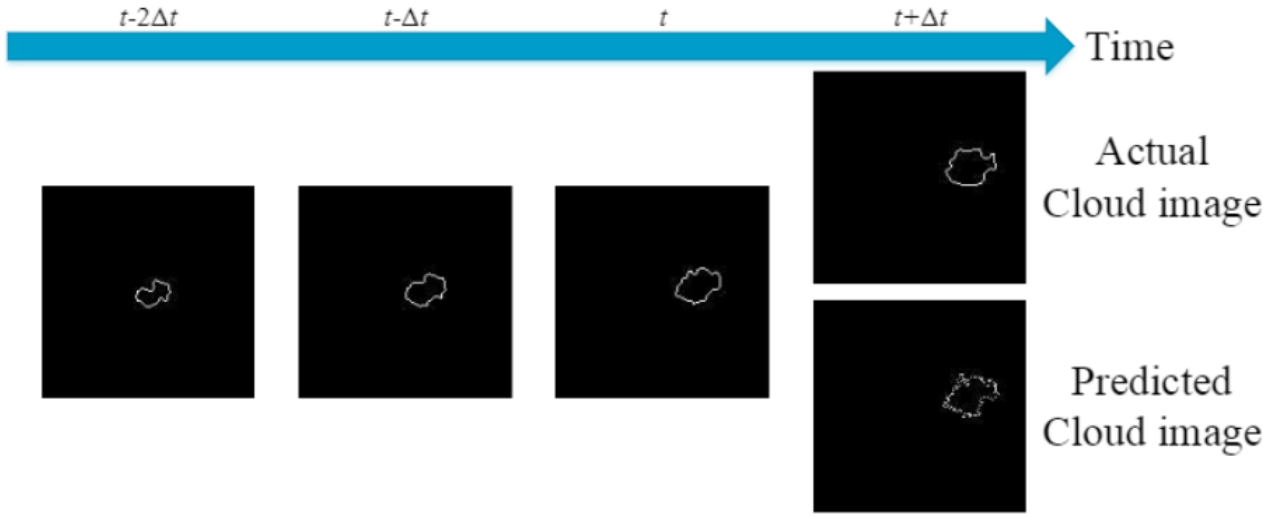


**Figure 35.** Cloud forecasting results

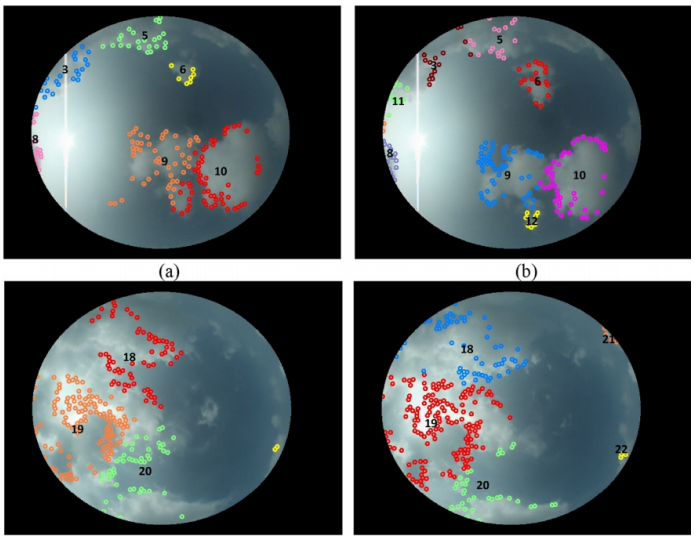


**Figure 36.** Feature point clustering and cluster tracking examples.

contour of the mask. The authors estimate the predominant movement direction from the weighted average of the angles of the movement of the clouds in relation with their magnitude (both are obtained from the optical flow algorithm). The path for each point constructing the associated elliptic trajectory that has a major axis with a length equal to the diameter of the circle containing the sky image is obtained. Figure 37(a) shows an example of the trajectories constructed by the algorithm. To estimate the length of the elliptic arc described by each feature of the clouds, an algorithm analyzes the angle described for the feature in two consecutive images, and then, the angle is translated to the desired time horizon. Once trajectories are properly defined and the movement over the paths is calculated by the angles, projections of the future movements are made (as shown in Figure 37(b)). The forecast algorithm registers when clouds will affect the irradiance reaching the solar module, creating a time series of binary states where a 1 represents a cloud and a 0 represents clear sky. The Scale-Invariant Feature Transform (SIFT) algorithm is applied to pairs of simultaneous images from both cameras. Valid features are then transposed from the image (pixels) to real space (azimuth and zenith). With real space coordinates defined, geometric functions are used to obtain the length of the vectors containing each feature and the geographical position of each camera in real space, from which the height of the evaluated feature can be derived. Validation of the forecasting system has been done with the irradiance data obtained by the mini solar photovoltaic module installed at the base of one of the cameras, from which the global horizontal irradiance is derived. Irradiance data has a temporal resolution of 5 seconds, however the forecast horizon had to be reduced from the desired value of 15 minutes to 5 minutes due to the dynamics of the region. To evaluate the performance the Mean

Absolute Error (MAE), Mean Biased Error (MBE) and Root Mean Square Error (RMSE) are used. The results show that the first day was a very cloudy day with high variability in irradiance, while the second had a period of clear sky during the midday. Although the first day has a huge RMSE of $939.8W/m^2$, the other metrics are at least comparable to those of the persistence model. During the second day, the behavior of the system was better, with a RMSE considerably inferior ($240.9W/m^2$), and the system even outperforms persistence model in the MAE.

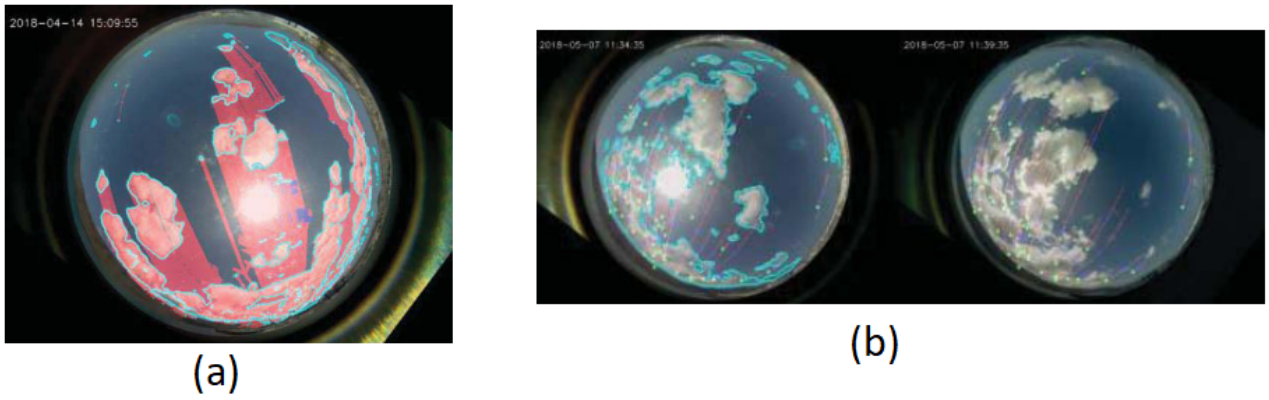


**Figure 37.** (a) Elliptical trajectories obtained for each point in the contours of the clouds mask. (b) Determination of clouds' movement. Light green dots represent the estimated position in $t+5$ (right) from the image in $t$ (left).

#### *1.9.2 A new ultra-short-term photovoltaic power prediction model based on ground-based cloud images*

In [42], a solar tracker is used to locate the sun. The reference image is divided into small blocks of the same size using the image segmentation algorithm. The corresponding matching block is selected in the current image, and the position deviation of matching block in current image and reference image is recorded, and labeled as the motion vector. Due to rapid change of cloud images, the matching of cloud images can be considered as an inexact matching problem, therefore, the sequential similarity detection algorithm (SSDA) is used in this paper. The forecasting cloud location is be obtained by the velocity extrapolation method. The authors use weighted moving average method to forecast the image brightness and the gray level histogram theory is adopted to recognize the cloudiness and to obtain the area in the cloud image within a certain threshold range. The RBF neural network was used to develop the prediction model based on the cloud image information. According to the analysis of surface radiation and extraction of image features, the image brightness and cloudiness are selected as the random influence sources, whereas the ambient temperature and surface radiance are chosen as the direct influence sources, and the historical power generation data is used as the reference influence source. The hidden layer of RBF neural network contains only one layer with $n$ neurons and the Gauss function is selected as a radial basis function. The mean absolute error (MAE) and mean absolute percentage error (MAPE) are used to evaluate the performance of the prediction models. The historical data are provided by the Key Laboratory of Ministry of Education in China. The data was taken on 19th and 20th of November, during time period 6:00-18:00. The comparison of AR and RBF prediction models based on the data of Hangzhou City is presented in Figure 38. The MAE of RBF model was 43.0 W, and the MAPE of RBF model was 4.2%. Meanwhile, the MAE of AR model was 50.1 W, and the MAPE of AR model was 4.5%. The relative error between the predicted value and the observed value was 3%. The daily electricity output for the AR method was 17.8 kWh, and the relative error between the predicted value and the observed value was 5%.

#### *1.9.3 Convolutional Neural Network for Short-term Solar Panel Output Prediction*

In [43], sky images and PV output data are collected from Mar.2017 to Mar.2018, spanning a whole year to reflect the seasonal cycle of meteorology conditions. Video recordings of the daytime sky are shot with a 6-megapixel fish-eye camera, which is located on top of Green Earth Sciences Building at Stanford Universities. In the baseline model, images are down-sampled to a resolution of 64x64 pixels to reduce training time. The testing set is twenty complete days of data isolated from the training process, with half of them sunny and the other half partly cloudy. The train-val set is shuffled by the day and subject to 10-fold cross-validation. A sequence of recent images are fed in where each image sequence input is concatenated on the color channel. The number of filters is substantially increased in the convolutional layers to account for the increased number of image input per sample. Recent PV panel output history is injected as input before the first fully-connected layer. We train the network using the Adam Optmizer with the mean square error (MSE) as loss function. The baseline model is able to perform relatively well, with a mean training set loss of $5.63kW^2$ and a mean validation set loss of $4.51kW^2$. For the sunny half of the test set, the

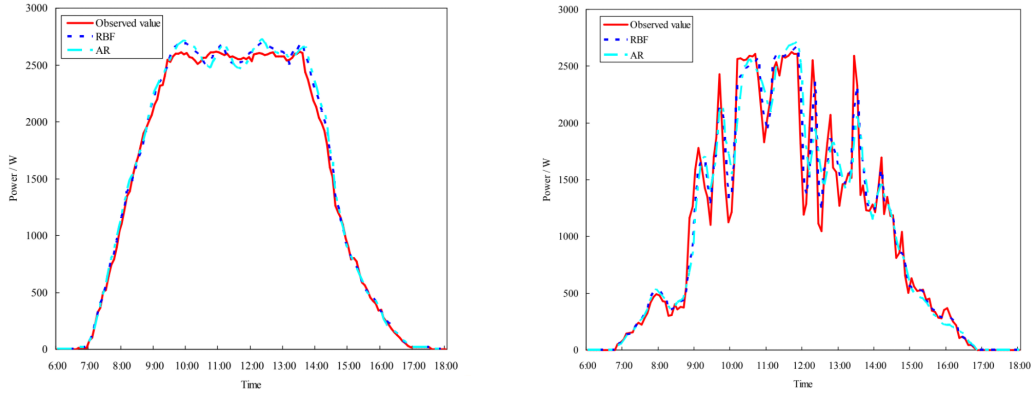


**Figure 38.** (a) Comparison of the two models on Nov. 19th. (b) Comparison of the two models on Nov. 20th.

baseline model is able to achieve a 26.22% reduction in RMSE. On the harder cloudy test set, the forecast skill still reaches 16.11%. The schematic of the proposed solution is shown in Figure 39.

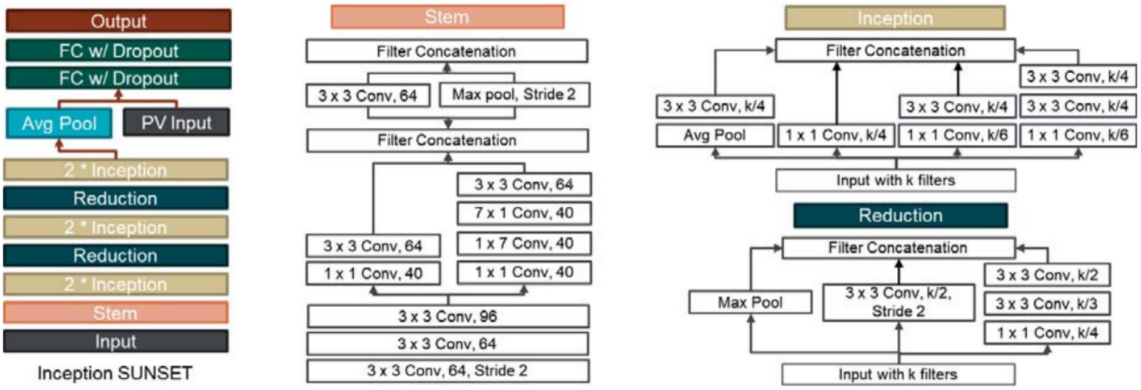


**Figure 39.** Schematic of the proposed "Inception inspired model". The image sequence goes through a stem as pre-processing. This is followed by several inception and reduction layers, which is shown in detail to the right. The graphical features are average pooled and stacked with the PV log to serve as input to fully connected layers as in Baseline.

#### *1.9.4 Deep photovoltaic nowcasting*

In [44], sky images were captured at 1280x1280 pixel resolution using a SonyIMX265 camera equipped with a Spacecom TV1634M fisheye lens pointing to the zenith. The temporal resolution of the used data is every minute. When image data is used, each input image actually corresponds to a 3D matrix with 4x5 channels, the images taken 60 s before the current time $t$ with a 15 s interval are stacked. A baseline model is defined with a multilayer perceptron (MLP) network. This MLP network is composed of two hidden layers and using a separate validation dataset it was determined that the dimensions of the hidden layer as 64 provide a good compromise between performance and generalization. For the temporal information the authors use the Long Short-Term Memory (LSTM) network. Instead of concatenating the latent vectors that are encoded from the input image set, they instead instead use a 2-layer LSTM network on these latent vectors. The networks are trained and evaluated on a large dataset containing 90 days, which is split randomly (by days): 80% (72 days) for training the networks, and 20% (18 days) for test. The test dataset is manually split into three different categories based on the weather conditions: clear, partly cloudy and overcast. Here, the authors manually define “clear” days as those with less than approximately 10% clouds on average throughout the day, “partly cloudy” have between 10% and 90%, and “overcast” are completely overcast days. The performance with the following metrics are taken on each of these categories: “mean absolute error” (MAE); “root mean squared error” (RMSE); “forecast skill score” (SS). Figure 40 shows a result example where a day that is mostly clear in the morning and cloudy in the afternoon. In the first half of the day, the model predicts the future power values very accurately (left). While sudden, unanticipated changes currently cannot be handled (middle), the model recovers when changes are less abrupt (right). The results show that even with longer time horizons, the proposed approach still achieves low error under clear skies and outperforms the persistence model with an SS-MAE of 16.4% and SS-RMSE of 11.5% for 2-min horizon, an

SS-MAE of 14.4% and SS-RMSE of 10.4% for 5-min horizon, and an SS-MAE of 12.1% and SS-RMSE of 7.7% for 10-min horizon. It is noticeable however that, as time horizon increases, the skill score decreases.

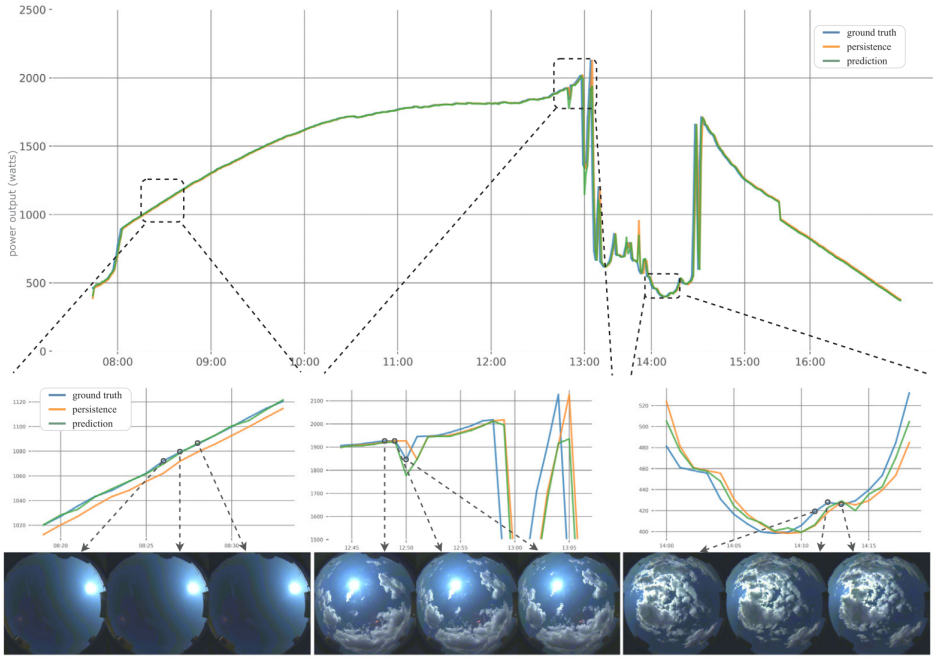


**Figure 40.** Prediction curve for 1-min horizon on a typical day captured on 04/02/2017. The plot in the top shows the photovoltaic power for ground truth (blue), persistence (orange), and prediction (green). Close-up views of the curves is shown the windows in the middle. Three sky images are shown in the bottom for each window.

#### *1.9.5 Image phase shift invariance based cloud motion displacement vector calculation method for ultra-short-term solar PV power forecasting*

In [45], a general estimate of cloud base height considering image distortion is applied and the proposed solution mainly focus on the horizontal position of clouds in the sky images. The automatic sky imaging system acquiring the sky images consists of a sky camera and its supporting software produced by EKO INSTRUMENTS. The sky camera is installed at the Yunnan Electric Power Research Institute in Yunnan province of China. The viewing angle of the camera is 120 and the time interval between two consecutive sky images is one minute. The supporting software of the sky camera is used for basic image preprocessing, including the perspective rectification, identification of cloud type based on cloud thickness, and sun position calculation. In this paper, perspective rectification has been performed on all images by the supporting software. The authors propose an image phase shift invariance (IPSI) based cloud motion displacement vector (CMDV) calculation method using Fourier phase correlation theory (FPCT) for minute time scale solar irradiance forecasting. First, the IPSI in terms of the synchronous rotation of two images is expounded to reflect the invariable cross correlation characteristic on the image displacement of two different images in frequency domain. Second, multiple CMDVs are obtained from the corresponding consecutive image pairs according to different rotational angles compared to the original images using FPCT. At last, the final CMDV is generated from all of the calculated CMDVs through a density and distance distribution based centroid iteration algorithm. To calculate the CMDV utilizing the IPSI characteristic in image deformation, a rotation of each sky image continuously from $0^o$ to $90^o$ with a certain angle is applied each time to extract the corresponding processing region. When the total rotation angle is equal to or greater than $90^o$, the elements of the extracted image grayscale matrix are the same with the existing matrices, just arranged in a different direction. Considering two scenarios of thick clouds and thin clouds, the authors chose two sequences of sky images for simulation: sequence A shows the motion of thick clouds and sequence B shows the motion of thin clouds. The deformation of clouds in sequence A is also more evident than in sequence B. The resolution of each sky image is 513x513 pixels. Four displacement estimation methods are applied in the simulations to calculate the cloud displacement: the original FPCT based CMDV calculation method; the IPSI-based CMDV calculation method using FPCT proposed in the paper; The PIV method contained in the MATLAB toolbox; The optical flow (OF) method using Piotr's Computer Vision MATLAB Toolbox. Sky image sequences A and B both contain 50 consecutive images. Therefore, 49 CMDVs for each method are obtained in one image sequence, and the displacement calculation results in the X and Y coordinate. The last four sky images

in image sequence A are shown in Figure 41, it can be seen that the sky region at the bottom of the image is becoming smaller and the thick cloud region at the top of the image is expanding, which indicates that the clouds are moving from top to bottom of the image. It is also noticeable that a small piece of cloud marked by the blue circle is moving to the lower right of the image. Therefore, the value of CMDV in the Y-coordinate should be less than zero, and the results obtained by IPSI based method are more reasonable. The CMDV calculation results of the first three methods are consistent in directions, i.e. clouds moving up and right in the sky images. The results of the original FPCT method and the IPSI-based method are practically identical in image sequence B, and very stable compared with the PIV method. For thin clouds, the gray scale value of cloud pixel is strongly influenced by sunlight and could change during the cloud movement. Therefore, the prerequisite assumption of OF method is less than satisfactory, so the CMDVs results calculated by this method were unacceptable.

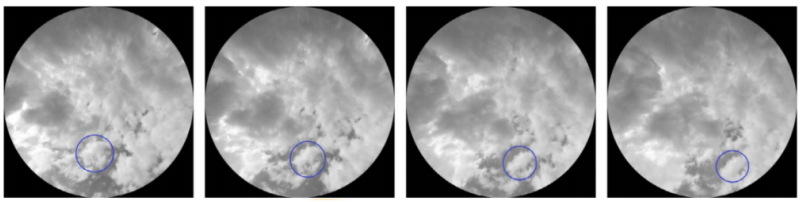

**Figure 41.** The last four sky images in image sequence A.

#### *1.9.6 Intra-hour direct normal irradiance forecasting through adaptive clear-sky modelling and cloud tracking*

In [46], the DNI measurements were obtained using an EKO Instruments MS-56 pyrheliometer mounted to an STR-22G sun tracker and the sky images were captured using an EKO Instruments SRF-02 sky camera. The equipment was located on the roof of the Hawken Engineering Building at the University of Queensland St Lucia campus, a total of 37 complete days (7 am to 6 pm) of data were collected over the summer of 2014/2015. Two images were taken at each interval, one at full exposure and one at the camera's "under exposed" setting. The sky images were processed with the EKO Instruments Findclouds software using the default binary RGB cloud classification algorithm. This software generates clear-sky DNI predictions using the Ineichen model. It uses extraterrestrial solar irradiance; solar position; and three atmospheric parameters, site to sea pressure ratio (PR), water vapour column (WVC), and aerosol optical depth at 700 nm; as inputs. The process of classifying DNI data into clear sky and non-clear sky sets is performed using a clear sky detection algorithm. The clear sky detection algorithm presented here is based on the observation that the clear-sky DNI versus time curve is a smooth diurnal curve. From this observation, it follows that successive clear-sky data points should have similar DNI values. A sensitivity analysis showed that PR variations within expected bounds have a negligible effect on DNI predictions. Thus, its value is fixed to 1.0 since the site is very close to sea-level. The sector-ladder method (used by the authors) is a two-part cloud fraction prediction algorithm that was developed as an alternative to traditional PIV method (Figure 42 illustrates the construction of a ladder for a given cloud flow vector). Two modifications to improve the accuracy of the sector-ladder method are proposed in this work. The first is to use the weighted mean of circular quantities and the second is to pass these preliminary cloud flow vectors through an autoregressive filter to remove noise and algorithm artefacts. The effectiveness of the modifications proposed to the sector method are assessed using the normalised angular root mean squared error (nARMSE) metric. Results show that that the autoregressive filtering improves the accuracy of the sector method for all proposed weightings. Other three metrics are used to compare the results with other works: normalised root mean squared error (nRMSE), normalised mean absolute error (nMAE), and forecast skill (FS). To statistically compare the two methods, the error metrics are evaluated over all the sample days for prediction horizons of 1–15 min. The average nRMSE values across all prediction horizons for days of average cloud fraction of 0.2 or higher the modified sector-ladder method performs 13% better than the persistence method. After about 8 and a half minutes the proposed solution achieves better results for all metrics used.

#### *1.9.7 Prediction of HSV color model parameter values of cloud movement picture based on artificial neural networks*

In [47], a Java application is used to perform conversion from RGB to HSV and the morphological operations of erosion and dilation. The movement of the clouds is based on the detected centroid point of the identified countour-shaped object and the location change of this point within 12 seconds. Therefore the determination of the centroid position is calulated every 12 seconds. The clouds with an area smaller than 1000 pixels are ignored because it is claimed they don't affect the Sun coverage. The authors use the RGB values from the image histogram as inputs for the artificial neural network. The the artificial neural network adjusts the HSV parameters to detect cloud edges in order to maintain the precision of determining the position of the centroid. The neural network has 5 layers of neurons as input layer, three hidden layers and one output layer as shown Figure 43. The first input layer has 6 neurons and every neuron is used for one of the following parameters used in the learning phase: the average R value from the histogram from the previous image processed 12 seconds ago, the average value of the GB

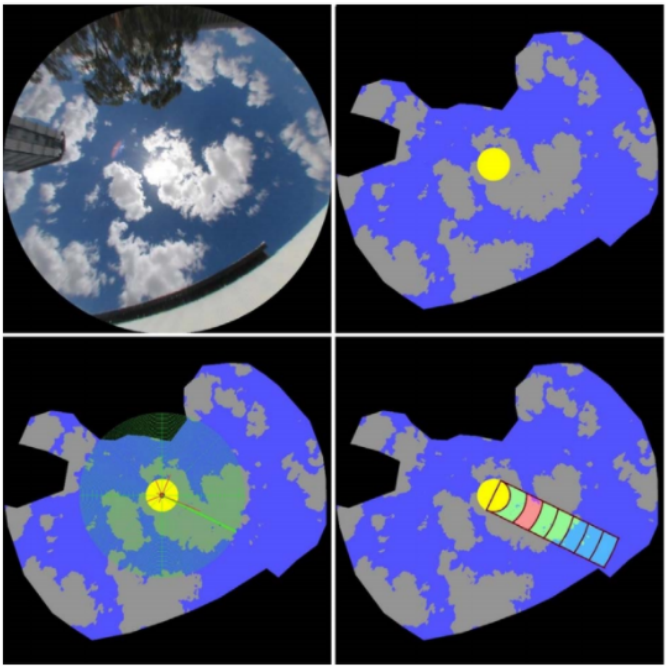

**Figure 42.** The ladder method. A 'ladder', consisting of concentric arcs of radius, is projected from the sun centre in the direction of cloud flow. The cloud fraction in each ladder band corresponds to the cloud fraction at different prediction horizons.

component from the histogram from the previous image, the number of very large clouds ($area > 20000 pixels$), the number of clouds with an $area > 0, area < 100$ pixels, and the number of clouds with surface equal to zero pixels. The output layer has six neurons each of which is assigned one of the following normalized values for the following parameters: "HUE MIN", "HUE MAX", "SAT MIN", "SAT MAX", "VAL MIN" and "VAL MAX". The input values were normalized between 0 and 1. The neural network was first trained on 100 images to automatically process 471 images for which the optimal parameters were defined by an image processing expert. After that, the amount of images for learning increased to 200, 300 and 400. The results show that with 10000 learning iterations the network was able to achieve an error rate of 0.07% with 400 images.

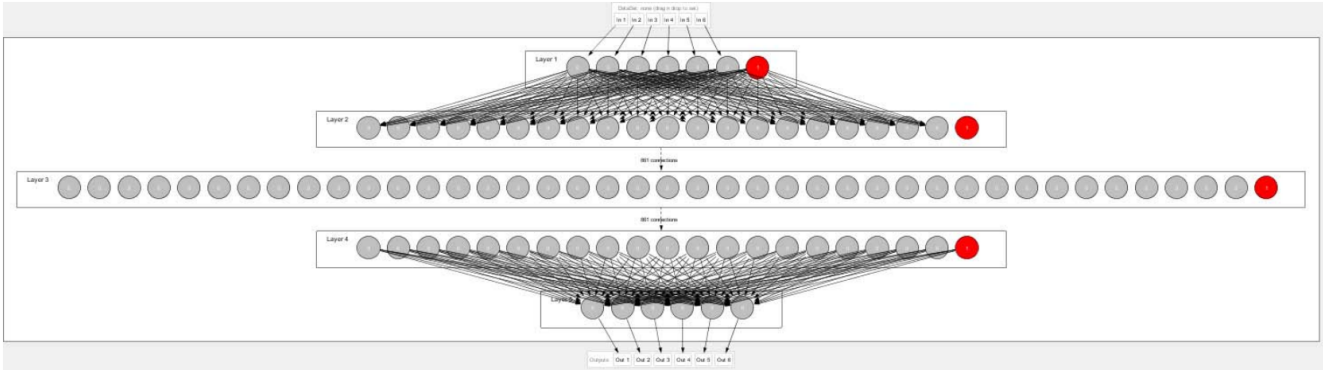

**Figure 43.** Architecture of the proposed neural network.

#### *1.9.8 Towards the intrahour forecasting of direct normal irradiance using sky-imaging data*

In [48], the database is derived from measurements realized in Perpignan, at the PROMES-CNRS laboratory, using a Rotating Shadowband Irradiometer (RSI). The station is located in southern France, approximately 20 km west of the Mediterranean Sea. The authors used 80 days of data, collected in Perpignan from July 30 to October 17, 2015. They used the empirical model proposed by Ineichen and Perez to compute the position of the Sun. Regarding the forecasting, the approach relies on a persistence of atmospheric turbidity, taking advantage of the fact that changes in this quantity are relatively small throughout the day in comparison to changes in DNI, even when the sky is free of clouds. Overall, for the available data (a total of 80 days),

the Mean Absolute Error (MAE) is lower than 15 $Wm^{-2}$ whereas the Root Mean Square Error (RMSE) is lower than $20Wm^{-2}$, regardless of the forecast horizon ($\Delta t_f \leq 30min$). The PROMES Sky Imager (PSI) consists in a 4-megapixel color camera equipped with a fisheye lens and protected by a waterproof enclosure. Sky images are collected every 20 s at a resolution of 2048x2048 pixels, with 10 bits per channel. A geometric angular calibration of the camera has been performed in order to get the relationship between a given pixel point and its projection onto the unit sphere. The authors used the OcamCalib toolbox to calibrate the camera. The system is not equipped with a solar occulting device to reduce the light intensity reaching the sensor. The authors also generate high dynamic range (HDR) images from the low dynamic range (LDR) images. The algorithm developed for cloud detection takes inspiration from the classification algorithm proposed by Ghonima et al. when clear-sky anisotropy is known and the hybrid thresholding algorithm proposed by Li et al. in the opposite case. An adaptive threshold, calculated using the Otsu algorithm, is applied to the NRBR (Normalized Red/Blue Ratio) feature. The model that relies on a persistence of direct normal irradiance is the simplest model included in the comparative study. It allows forecasting DNI for all types of horizons and does not need any knowledge about the atmosphere. Having access to real-time measurements of DNI is the only requirement. The DNI is split into two terms: clear-sky DNI and the clear-sky index. The forecasting of clear-sky DNI uses the aforementioned technique and the proposed DNI forecasting model, makes use of an Adaptive Network-based Fuzzy Inference System (ANFIS). The variables used as model inputs and the tuning of the system (through a supervised learning process) and the model allows the clear-sky index to be forecasted over the next 30 min. The authors used a training set composed of 40 days, a validation set composed of 20 days, and 20 consecutive days to test the model. The learning process has allowed 8 fuzzy rules to be designed, for a total of 56 parameters in the system. Figure 44 shows some 30-min forecasts of DNI produced by the four models included in the comparative study. The ANFIS-based model outperforms the other models in terms of forecasting accuracy, regardless of the forecast horizon. Both persistence models have similar accuracy: RMSE is approximately equal to $170Wm^{-2}$, with $\Delta t_f = 15min$, and equal to $220Wm^{-2}$, with $\Delta t_f = 30min$. Taking one of these two models as reference, RMSE is reduced of about $20Wm^{-2}$ using the ANFIS-based model, with $\Delta t_f = 15min$. It is reduced of about $40Wm^{-2}$, with $\Delta t_f = 30min$. Regarding the deterministic model based on $F_c$ , it outperforms the persistence models for a forecast horizon longer than approximately 11 min.

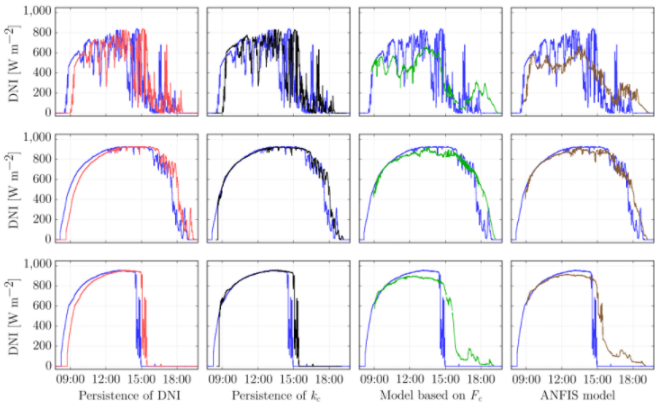


**Figure 44.** 30-min forecasts of DNI. Blue lines are for DNI measurements. Top: October 1, 2015. Middle: October 10, 2015. Bottom: October 15, 2015.

### *1.9.9 An Unsupervised Clustering-Based Short-Term Solar Forecasting Methodology Using Multi-Model Machine Learning Blending*

The authors in [49] developed an unsupervised clustering-based (UC-based) solar forecasting methodology for short-term (1-hour-ahead) global horizontal irradiance (GHI) forecasting. This methodology consists of three parts: GHI time series unsupervised clustering, pattern recognition, and UC-based forecasting. The daily GHI time series is first clustered by an Optimized Cross-validated Clustering (OCCUR) method, which determines the optimal number of clusters and best clustering results. Then, support vector machine pattern recognition (SVM-PR) is adopted to recognize the category of a certain day using the first few hours data in the forecasting stage. GHI forecasts are generated by a two-layer Machine learning based Multi-Model (M3) forecasting framework. The overall architecture of this framework is shown in Figure 45 The features selected in this paper are from three information resources: GHI features: historical GHI, clear sky GHI, and clear sky index (CSI); sky imaging features: mean, standard deviation, and Rényi entropy of the normalized sky image pixel RBR (nRBR) values; and other meteorological measurements: direct normal irradiance (DNI), direct horizontal irradiance (DHI), temperature (T), relative humidity (RH), pressure (Pres), wind speed (WS), and wind direction (WD); with the Ineichen and Perez model

selected as the clear-sky model. A 1-year hourly GHI and sky imaging data set released by the National Renewable Energy Laboratory (NREL) is adopted in the case study, which was collected at a location in Colorado, USA. The number of pixels in each image is 1392x1040 and the ratio of training days to testing days is 3:1. Two error metrics are used to evaluate forecasting results, which are normalized mean absolute error (nMAE) and normalized root mean square error (nRMSE). Case studies based on 1-year of solar data showed that the OCCUR method successfully clustered daily GHI time series by using different cross-validated unsupervised clustering methods, the SVM-PR enhanced classification accuracy by using limited data within a day, which made it possible to perform UC-based forecasting, the UC-M3 forecasting method in conjunction with M3 significantly improved the short-term GHI forecasting accuracy by the effectiveness of both UC and M3 methods and the calendar and weather effects analysis indicated the robust and consistent improvements of the developed UCM3 method.

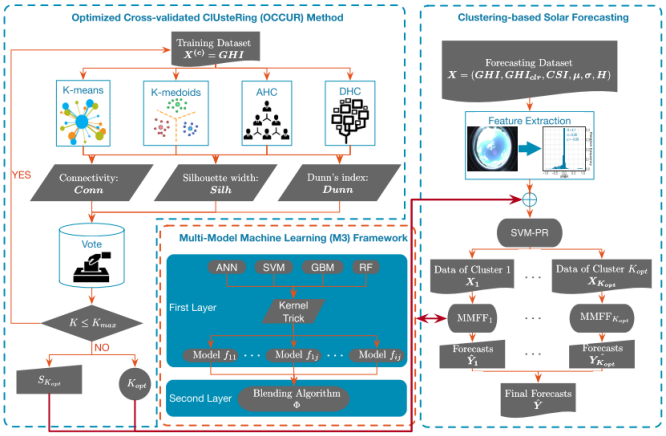


**Figure 45.** Overall framework of the unsupervised clustering-based short-term solar forecasting methodology.

#### *1.9.10 Deep Learning for Inferring the Surface Solar Irradiance from Sky Imagery*

In [50], the authors use a data set consisting of RGB hemispheric sky images of size 512x512 pixels, taken with a fish-eye camera, and their corresponding GHI, recorded with a pyranometer. The data set was recorded during a period of three months (October, November and December of 2016) in Folsom, CA, USA. A record is taken every minute. A stochastic gradient descent k-means algorithms is proposed and before running the k-means algorithm, a mask hiding the surrounding components which are not part of the sky is applied to the images in order to intercept exclusively sky pixels. After training the mini-batch k-means algorithm on the entire set of sky images, the authors perform the segmentation using the resultant centroids. Then, for each segmented image, the number of pixels present in each segment is extracted and referred as per cluster number of pixels (PCNP). The data set consists of 7000 sky images labeled manually, from which 75% serve as a training set and the remaining sky images as a testing set. The classifier is a single hidden layer neural network that takes as inputs the PCNP features extracted from the raw sky images and outputs two probability scores corresponding to the two labels. The data set used consists of 256 PCNP features. Dropout regularization and batch normalization are applied to each hidden layer of the network during the training phase. Figure 46 shows the overall proposed architecture. The hyper-parameters of the deep neural network are determined using 10-fold cross validation. The estimation of the transfer function between the PCNP features and the GHI shows on the testing set a coefficient of determination $R^2$ of 0.95. The corresponding mean absolute error on GHI estimation is about 27 $W/m^2$, where the measured GHI ranges from 0 to 931 $W/m^2$.

#### *1.9.11 Learning to Compensate Photovoltaic Power Fluctuations from Images of the Sky by Imitating an Optimal Policy*

In [51], the authors focus on a PV power plant with ramp rate limitations that uses a battery to compensate sudden shortfalls and sudden overproduction due to cloud movement. A control policy trained with imitation learning aims to imitate the actions taken by a target policy $\pi^*$ with the goal of finding a policy $\pi_\theta$ that performs similarly to the policy $\pi^*$ when applied on the underlying dynamical system. To achieve that the authors train a neural network controller with imitation learning based on the optimal MPC control actions in hindsight with the neural network based on the ResNet architecture. The model predictive control (MPC) on the training data is used to compute the optimal policy which is used as the target policy for imitation learning. The authors use the DAGGER algorithm together with a large dataset of past irradiance measurements and sky images. Real-world data collected by ABB Corporate Research from a PV power plant located in Italy is used. The data consists of whole sky images and various sensor measurements such as irradiance values. The images are post-processed to have a high dynamic range (HDR), which improves the quality as the camera is pointed at the sun. Measurements were taken every seven seconds during daytime for 256 days with the days in the dataset assigned at random to the training, validation and test set

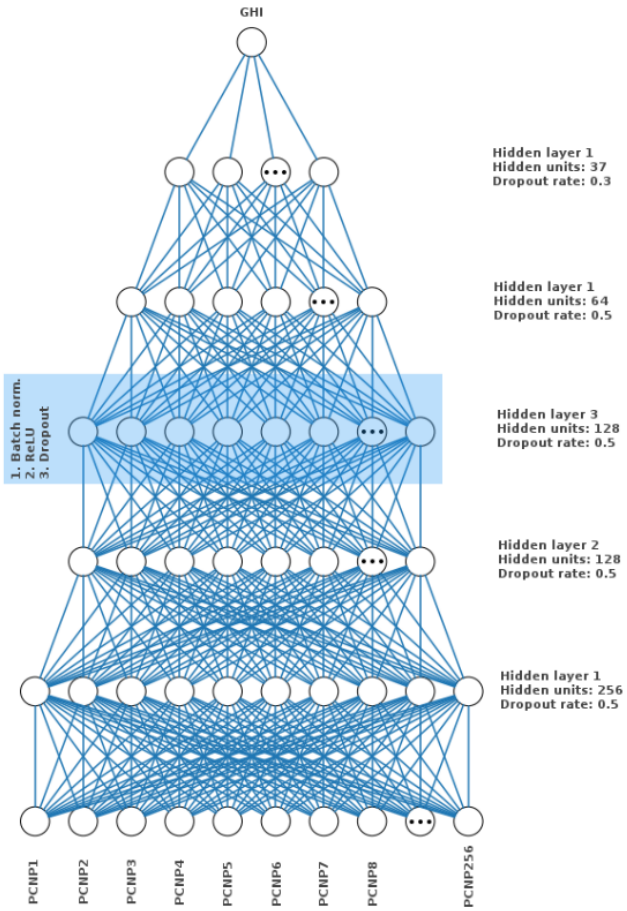


**Figure 46.** Architecture of the deep neural network.

with a split of 70%, 15% and 15%, respectively. The authors scale irradiance values to [0, 1] based on their value range in the dataset and divide each pixel by their maximum possible value, which is 255. A mask is applied to the images to remove the border of the camera and other background objects. The image is centered on the sun and cropped from 1566x1566 pixels to 448x448. To this end, the sun's position in the sky based on time, camera, and geographic location is computed. The images are further downsampled by a factor of two to obtain an image of size 224x224, suitable for training in a neural network. An overview of the proposed architecture is shown in Figure 47(a). As an input to the policy sequence of the current image and the images 30 seconds and 1 minute in the past is used. Past images are also included to allow the policy to extract cloud movement, which is not contained in a single static image. The neural network outputs a probability distribution over actions. The authors use this distribution to estimate the confidence of the proposed model, where a high probability for a single action indicates a high confidence. To evaluate the reliability of these confidence estimates on the real data, they test how strongly the output distribution correlates with the accuracy of the model. To this end, the probability distribution over actions for the states visited during a run on the validation set and bin the actions is computed according to the maximum assigned probability across all three actions. The average accuracy of these bins matches the corresponding confidence of the neural network. The authors only use the neural network action when the confidence estimate of the prediction is above some fixed threshold, and employ the baseline policy otherwise. The proposed approach is compared to the baseline and optimal policy. The best performance is achieved with a threshold of 0.65 resulting in an improvement of 92% over the baseline, close to the optimal policy. The authors evaluate the performance on the original problem, where the policy only has access to past and present irradiance data and images. On the test set, the best results are achieved with a confidence threshold of 0.7. With only past and present data as input, the model is able to achieve an improvement of 4.35% over the baseline. An overview of the performance of all methods is shown in Figure 47(b).

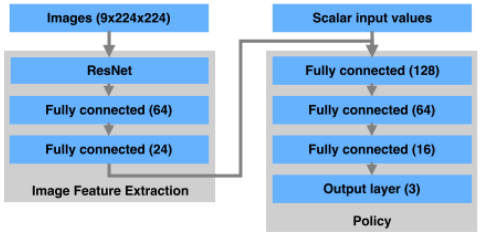


(a)

PERFORMANCE OVERVIEW

| Experiment | Validation ($10^7$) | Test ($10^7$) |
|---|---|---|
| Optimal | 100% (1.448) | 100% (1.880) |
| Future Irradiance | 91.62% (1.497) | 92.37% (1.940) |
| Future Images | 58.62% (1.690) | 62.14% (2.179) |
| Past Data | 2.62% (2.018) | 4.35% (2.637) |
| Baseline | 0% (2.033) | 0% (2.671) |

(b)

**Figure 47.** (a) Neural network architecture. The left part of the network uses a ResNet to extract features from the images, while the right hand represents the control policy based on the features and scalar sensor measurements. (b) Overall performance.

## 1.10 2019

### *1.10.1 3D-CNN-based feature extraction of ground-based cloud images for direct normal irradiance prediction*

In [52], the clear-sky indexes are used as the classification criterion for ground-based cloud (GBC) image feature extraction. The clear-sky index is defined as the ratio between the measured DNI and the estimated theoretical clear-sky DNI. The Linke formulation with turbidity coefficient is used to calculate theoretical clear-sky DNI. For action recognition in videos, the 3D-CNN method takes all video frames as inputs and does not rely on any preprocessing. In the proposed solution, the data from the NREL database are used for the experiments. Multiple 3D convolutions with different kernels are applied to the same location in the input layer. All the weights of convolutional connections are not shared. The number of valid samples is approximately 13,000. In this study, the classification criterion of 3D-CNN model is based on the clear-sky index to be predicted (DNI attenuation). The clear-sky index $k$ is divided into 5 categories, including completely overcast and rainy strong attenuation, medium attenuation, weak attenuation and clear-sky. The final forecasting model with the input of fully-connected features and DNI data is used for DNI predication. The Bayesian information criterion (BIC) for the DNI training set is used to determine the input dimension of forecasting model. The input dimension is chosen to be 3. Linear autoregressive model (AR) and nonlinear multi-layer perceptron model (MLP) are selected as forecasting models. The proposed DNI forecasting model is shown in Figure 48. The GBC images are taken by a Total Sky Imager (TSI-880), and the DNI values are measured by a Kipp and Zonen pyrheliometer. The image resolution is 352x288 pixels and the GBC images in different weather. The models are evaluated synthetically using the following evaluation criteria: normalized root mean square error (nRMSE); normalized mean absolute error (nMAE); normalized mean bias error (nMBE); mean absolute percentage error (MAPE). In order to prevent over-fitting, the 10% data in 2014 is used as the validation set. To evaluate the performance of the proposed 3D-CNN-based features extraction method for predicting DNI, the two groups of experiments were carried out by using: (1) only historical measured DNI time series and (2) historical measured DNI, theoretical clear-sky DNI and extracted GBC images features as inputs. The forecasting results of AR-A are close to the AR-M results. However, MLP-A performance is better than MLP-M. The MLP model coupled the automatically extracted GBC images features with DNI data has the best forecasting results with nRMSE of 30.82% and nMAE of 17.91%, the forecast skill is 17.06%.

### *1.10.2 A Method for Detailed, Short-Term Energy Yield Forecasting of Photovoltaic Installations*

In [53], the data set used for the studies has been acquired at the University of Oldenburg and spans from the 19th of July until 31st of August 2015. Sky images are retrieved every 10s from sunrise to sunset with a Vivotek FE8172V network camera equipped with a fisheye lens. Images are taken at 1920x1920 pixels resolution. A sun tracker equipped with a pyrheliometer for DNI and a shaded pyranometer for DHI measurements is placed three meters north-west of the camera. Specific image features are computed for each image, then provided as inputs for the machine learning applications. The 4 features are quantified characteristics like image textures, color values and other metrics. The features are computed on the masked image, so that non-sky parts of the image are masked out before image features are computed. In this study, the extracted image features are used for irradiance modelling (k-neighbors neural network model), cloud classification (support vector classification model) and the energy yield prediction with neural networks. The features used for the focus of the study, the neural network based energy yield prediction, are presented briefly. First, the image Contrast retrieved from the grey-level co-occurrence matrix (GLCM) is used as input to the neural network. Additionally, image features are derived from RGB channel-based color statistics. In addition to the image features, the solar position relative to the observer and the cloud coverage as the ratio of cloudy pixels to all pixels are used as input for the neural network. The sky imaging software determines for each image the predominant sky or cloud type as one of seven categories: Cumulus (Cu); Cirrostratus (Cs), Cirrus (Ci); Cirrocumulus (Cc), Altocumulus (Ac); Clear sky (Clear); Stratocumulus (Sc); Stratus (St), Altostratus (As); Nimbostratus (Ns), Cumulonimbus (Cb). The Support

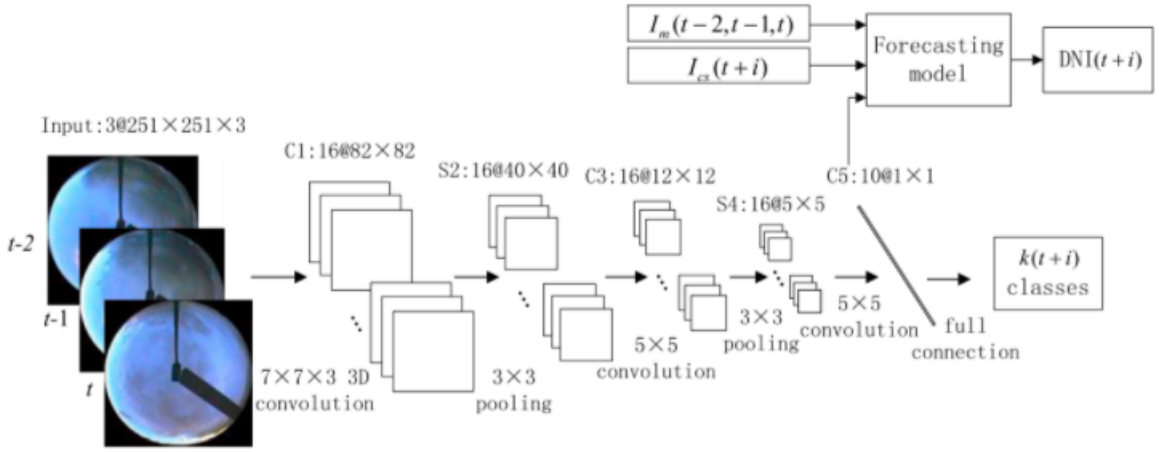


**Figure 48.** The DNI forecasting model. The 3D-CNN architecture consists of 3 convolution layers, 2 downsampling layers, and 1 fully-connected layer. The features in fully-connected layer and DNI value are used as forecasting model inputs.

Vector Classification (SVC) has been chosen with best classification results. About 21500 images were manually pre-selected into the different cloud type categories. The classification performance has been determined by applying a model trained on a subset of pre-classified images (70 %) on the remaining 30% of images. An accuracy of more than 99% correct classification is reached. A non-linear auto-regressive network with exogenous input was selected (NARX) to predict the DNI. A two hidden layer structure was chosen with the dataset segmented into training (70%) and testing/validation (30%) sub-sets. The final layer was chosen among a binary decision model, a weighted average model and an extra multi-layer perceptron network, where cloud class probabilities also contributed as inputs. An abstract view of the network is shown in Figure 49. For most part of the results section, the normalized root-mean-square error and the forecast skill score (FSS) are used. From the presented results, both models perform better than persistence. First, the bias of the power forecast model is increasing with the horizon, reaching values up to 10%. The proposed model performs clearly better on all forecast horizons with regard to persistence vs. the benchmark power model. Skill scores are always positive, as high as 39%, highlighting the inability of persistence to capture all the stochastic effects in such conditions.

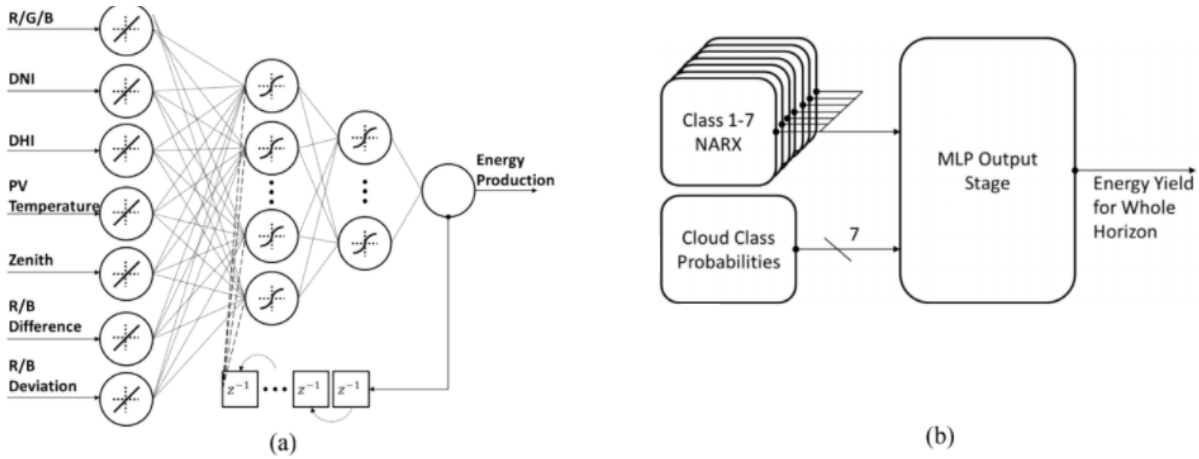


**Figure 49.** (a) Morphology of the NN for each class, with all inputs present, (b) Topology of the final forecast system.

### *1.10.3 A Short Term Cloud Tracking Model Based on the Bruhn Optical Flow Method*

In [54], sky images were obtained in regular intervals of 5 seconds with a Nikon D60 camera, which was fitted with a Sigma 4.5mm circular fisheye lens. The proposed model utilizes the Bruhn method which is a hybrid approach that combines both the Lucas-Kanade and Horn-Schunk approach. The Sun, if present in images, is identified and the pixels surrounding it are masked out as undefined pixels since they belong neither to the cloud nor sky. To segment sky and cloud pixels the authors used the normalized ratio categories. A histogram of the ratio is obtained for an image and a threshold was determined by minimizing

the cross-entropy between the normalized ratio and the segmented binary image. By utilizing the Bruhn method, the optical flow between two images taken is obtained, which were taken at time $t = 0$ and $t = 60s$ respectively. The optical flow obtained was then imposed on the second image to obtain a forecast image at $t = 120s$. This was then compared with the actual image taken at $t = 120s$ and the tracking accuracy defined by means of comparing whether the sky/cloud classification for each pixel matched. Figure 50b showcases the image at t = 60s and this is combined with that of Figure 50a to obtain the optical flow in Figure 50c. Such a flow field is then used to warp a third image that corresponds to the forecast image at $t = 120s$, as seen in Figure 50e. By comparing with the actual image in Figure 50f corresponding to $t = 120s$, a tracking accuracy can then be obtained. Such a process was repeated for time steps ranging from $t = 5s$ to $t = 600s$. The tracking accuracy at each time step was obtained, and the results show that the proposed Bruhn based model, in general, achieves a tracking accuracy that is quite similar to other more conventional methods. If compared to the original Bruhn method with the second best performer for a timeframe up to t = 600s, it performs 0.6% better on average. Although the tracking accuracy eventually reduces to around 75% at $t = 600s$.

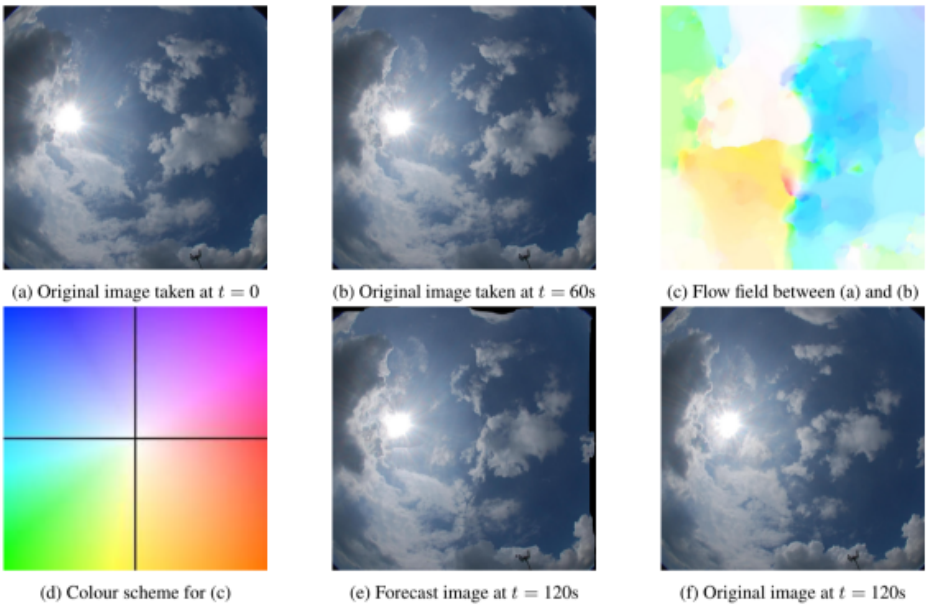


**Figure 50.** Cloud tracking procedure with the Bruhn method. Note that for (d), the x-axis and y-axis represent horizontal and vertical velocities respectively. For example, turquoise in (c) implies that movement is predominantly in the negative x-direction.

#### *1.10.4 Determination of cloud transmittance for all sky imager based solar nowcasting*

In [55], the nowcasting system consists of two ASIs (Mobotix Q24 surveillance cameras) and one CHP1 pyrheliometer. The studied nowcasting system is located at the Plataforma Solar de Almería (PSA) in southern Spain and additional cloud base height (CBH) measurements are taken by a CHM 15 k Nimbus ceilometer from the G. Lufft Mess- und Regeltechnik GmbH. A total of 574 cloudy days distributed over the years 2014 to 2017 are used for the probability analysis with 316,419 valid transmittance measurements detected within this data set. The complete years 2016 and 2017 are used for the validation of the transmittance estimation method. Cloud heights are discretized in five height ranges from 0 to 12.5 km in 2.5 km steps and optically very thin clouds with transmittance above 0.9 are not considered by the nowcasting system. The occurrence probability of the defined transmittance range within the height ranges is analyzed for each of the 574 days separately. For the two lowest height ranges, the average probability for optically very thick clouds are 93% and 77%. The remaining transmittance ranges have an average probability below 10%. However, the average probability for optically thin clouds rises to 21%. The average probability for thick clouds is quite low with 2% and 6% for the highest cloud height range. On the opposite side of the transmittance spectrum the average probabilities are 23% and 54%. The transmittance estimation for the nowcasting system is based on the ASI derived cloud object specific cloud height and shadow projection is done individually for each cloud. DNI maps for the current situation and forecasts up to 15 min ahead in 1 min steps are created and the actual cloud transmittance measurement is applied to the DNI map with a lead time of 0 min. The clouds responsible for the transmittance measurement received previously to the transmittance measurement a transmittance estimation which is known from the DNI map with a lead time of 1 min as shown in Figure 51. The cloud height validation of the nowcasting system detected a tendency for a slight

overestimation of the cloud height. The overall average MAD and RMSD over the entire data set are 0.11 and 0.16 respectively. Relative deviation metrics of the validation period (two years) are: MAD and RMSD for lead time 0 min is approximately 2%, 4% and 8%, respectively, and rises up to 5%, 15% and 23%, respectively, for a lead time of 15. The deviations increase for higher lead times, due to uncertainties of the used tracking and transmittance estimation method.

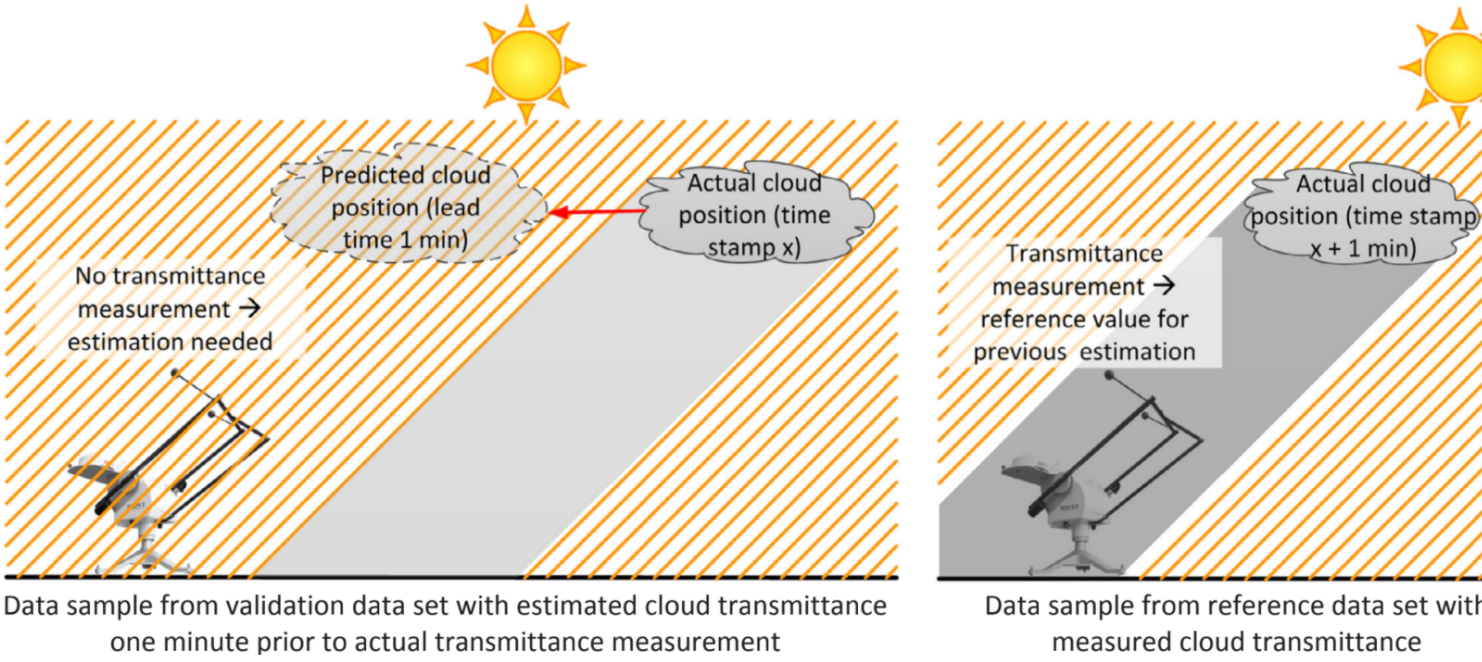


**Figure 51.** Illustration matching transmittance measurements with previously estimated transmittance values from the same cloud. (Left) cloud with estimated cloud transmittance 1 min prior to actual transmittance measurement. (Right) Cloud with transmittance measurement.

#### *1.10.5 Intrahour Cloud Tracking Based on Optical Flow*

In [56], the images were obtained by a commercial All-Sky camera (Model: SRF-02), operating on a flat roof of a laboratory of the Hong Kong Polytechnic University. The camera is programmed to capture a pair of images every 5 seconds. One is a normal-exposure image, the other is the associated under-exposure image with the same scene. All the images are stored in 24-bit (8 bit for each RGB channel) JPEG format with a maximum resolution of 1600x1200. The color edge image is firstly generated using the color image edge extraction algorithm. Then, the corresponding grayscale image can be obtained by the weighted average method. Next, a binary mask image is completed after executing the filling algorithm twice. In addition, due to the edge distortion, the zenith angle is set to $70^{o}$. In order to track the movement of clod, the authors identify cloudy pixels apart from clear-sky pixels. The authors obtain the optimal threshold of each criterion for different clouds, and verify whether optimal threshold of each criterion is the same. In order to find the optimal threshold, a reference binary image was create. After identifying clouds the binary image of original image is used and the optical flow algorithm (with the Lukas-Kanade algorithm) is used to track the flow of cloud pixels, as shown in Figure 52. The authors executed the optical flow algorithm on six datasets. Since the camera is programmed to capture images every 5 seconds, the precision of actual time is in units of 5 seconds. For the given six datasets, the prediction error is less than 25%. The average error of the six datasets is 16.4%.

#### *1.10.6 Pattern Classification and PSO Optimal Weights Based Sky Images Cloud Motion Speed Calculation Method for Solar PV Power Forecasting*

In [57], the authors propose a pattern classification and particle swarm optimization (PSO) optimal weights based sky images cloud motion speed calculation method. The authors use a texture features based on a gray-level co-occurrence matrix (GLCM) to classify the clouds. Its basic idea is to widen the gray levels that contain more pixels in the image, and to compress the gray levels that contain fewer pixels in the image. The flowchart of the PV power forecasting is shown in Figure 53. The authors generate four GLCMs for each sky image, and the corresponding energy, correlation, entropy, and contrast mean values are calculated as the four-dimensional (4-D) texture feature vectors of each image. Then, the mean of the feature vectors of two adjacent images are calculated as their common feature vectors and take them as samples of pattern classification. The k-means to cluster the cloud are used in this approach, alongside the block matching algorithm and the optical flow (with

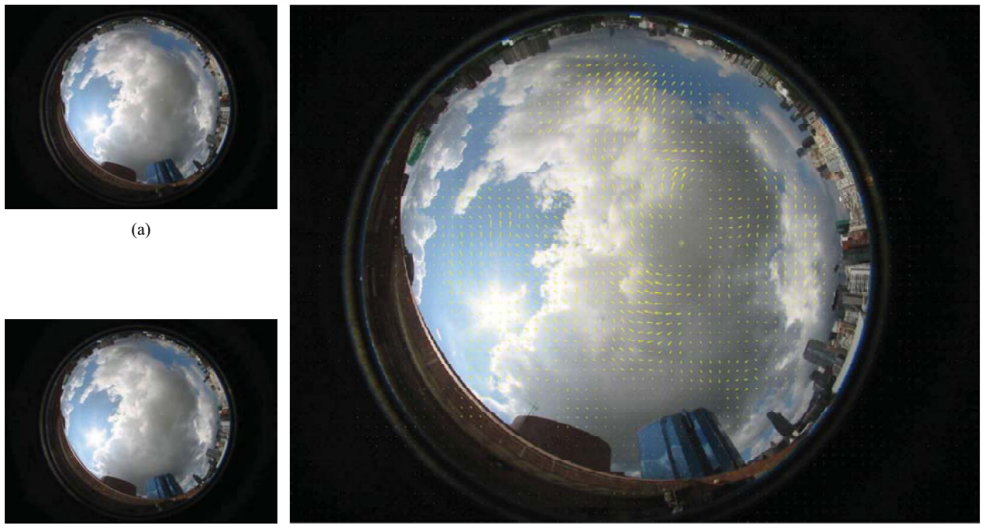


**Figure 52.** (a) Original image at time $t = n$; (b) Original image at time t=n+1; (c) Processed image with velocity vectors.

Lucas-Kanade algorithm), to track the moving clouds. The SURF feature operator is used for image matching. The data used are sky images provided by Yunnan Electric Power Research Institute as the experimental sample. These photos were taken in August 2015 and at intervals of 1 min. The authors used the correlation coefficient (R1), variance (R3), and sum of gray value differences (R4) to evaluate the accuracy of the algorithm. The resolution of these images was 256x256. Among them, 300 images were selected as training samples and 200 images were used as testing samples. The proposed combined calculation modeling has higher accuracy than the other three traditional methods. Especially, the calculation precision of SURF feature matching algorithm and optical flow algorithm is very low in class 6 and in class 9 separately. The results show that if different computing strategies are not adopted for different classes of sky images, the overall accuracy of the testing samples will be greatly reduced. The authors applied the cross-validation method to further develop the simulation with a total of 300 training samples and 200 testing samples. The authors use the samples to train and test the model, and present the average calculation accuracy $R1$ of the testing images. It can be seen that the average accuracies are similar.

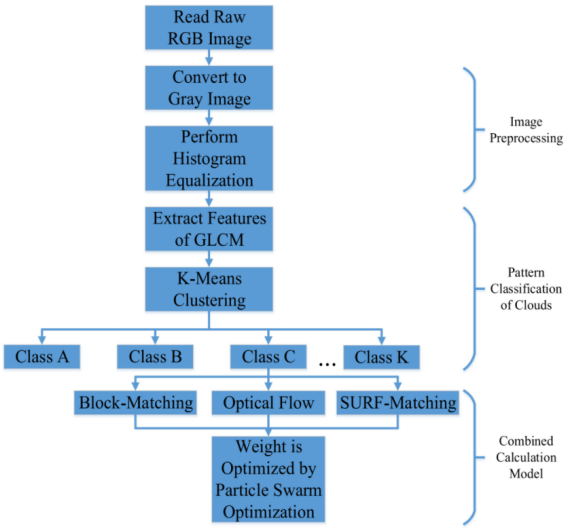


**Figure 53.** Flowchart of the PCPOW.

#### *1.10.7 Short Term Solar Irradiance Forecast based on Image Processing and Cloud Motion Detection*

In [58], the authors propose a 10-minute irradiance forecast using dense optical flow, specifically coarse to fine optical flow and ResNet50 machine learning algorithm. The major contribution in this study is the use of dense optical flow, which would be

more efficient to show the cloud movement parameters. For this study, the data have been acquired in the form of cloud images from National Renewable Energy Lab (NREL) sky imager, which has a time horizon of 10 minutes. The are resized to 800x800, the irrelevant color components are removed and averaging of the pixel values is applied. The optical flow Gunner Farneback's algorithm is used to track all the features in the image. More specifically, coarse to fine optical flow is used with Gunner Farneback's algorithm. Figure 54(a) shows the input images from May 5th, 2017 to the optical flow algorithm. The thermal image generated as the result of optical flow is shown in Figure 54(b). The thermal image is then converted to RGB image. Figure 54(c) shows the actual image and the image predicted using optical flow at 6:20 AM. A residual learning algorithm (ResNet50) is used with added three layers (with activation "relu") just before the last layer, with the density of 1000 in the last fourth layer, 500 in the last third layer and 5 on last second layer. The model is trained on shuffled optical flow output images and corresponding irradiance data of 6 months, where the training accuracy was found to be 94.67%. The trained model is hence tested on one month of data. The performance of the proposed approach is evaluated using Root Mean Squared Error (RMSE), Mean Absolute Error (MAE) and Mean Absolute Percentage Error (MAPE) parameters. The results shows that for clear sky the approach achieved 3.81 MAE, 6.11 RMSE and 2.91% MAPE; for partially cloudy sky it achieved 9.01 MAE, 15.38 RMSE and 4.84% MAPE; for overcast sky it achieved 5.46 MAE, 7.8 RMSE and 6.6% MAPE.

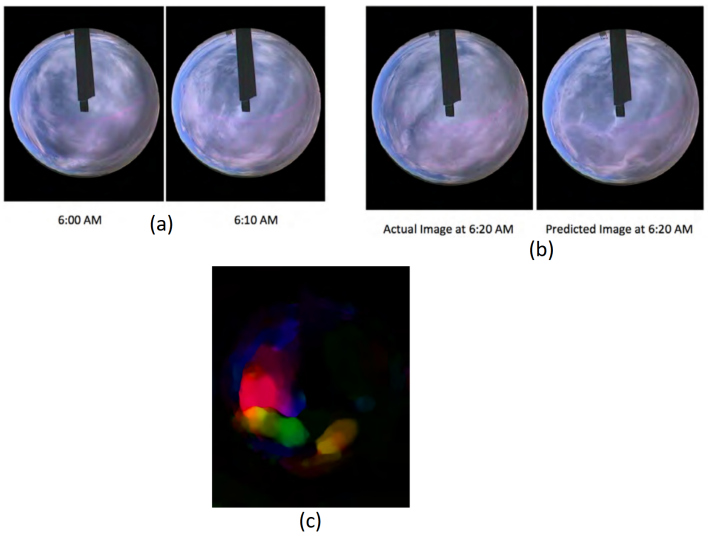


**Figure 54.** (a) Input images to optical flow. (b) Thermal image after running the optical flow. (c) Optical flow results.

#### *1.10.8 Short-term solar power forecast with deep learning: Exploring optimal input and output configuration*

In [59], data are collected from March 1st 2017 to March 1st 2018, spanning a complete year to incorporate seasonal cycles. The SUNSET (Stanford University Neural network for Solar Electricity Trend) model ingests two categories of data: sky images and PV generation. Videos are captured in a resolution of 1536x1536 pixels at 20 frames per second. Images (.jpg) are extracted at a chosen sampling frequency, and down-sampled to a resolution of 64x64 pixels. Images are retained between the hours of 6:00 AM and 8:00 PM local time. Images with no simultaneous PV output are removed from the data set. PV panel output data is collected from the closest solar PV array to the camera, located on top of Stanford's Jen-Hsun Huang Engineering Center. The total number of valid observations totals approximately 77,000 in the baseline input configuration. The test set includes twenty complete days of data isolated from the training process, with nine sunny and eleven partly cloudy and the test set has roughly equal coverage from each season and each cloud genus, from stratiform clouds during the rainy winter to high cirriform clouds in clear summer. The authors use intra-day consecutive splitting: data from the same day ends up in the same data set, either the training, validation or test and employ leave-one-out ten-fold cross-validation (CV). In the SUNSET model, a sequence of recent images first go through two convolutional structures. Comparing to a single frame, image sequences can better capture trends of cloud movement. After two convolution structures, recent PV output history is injected. The architecture of the deep convolutional neural network is shown in Figure 55. The authors used mean squared error (MSE) as the loss function. When the CV is finished, the model performance is characterized by mean RMSE across the 10 validation folds. As benchmarks for the SUNSET models, they developed a smart persistence model (henceforth simply persistence) and an auto-regressive (AR) model. For the SUNSET baseline, it has a training set RMSE of 2.37 kW, and a cross-validated validation set RMSE of 2.12 kW, which is significantly smaller than the persistence and AR references. On the test set, the baseline model outperforms the persistence model in cloudy and overall category, and the AR model in all conditions. Comparing to persistence, it achieves 16.3% forecast skill in cloudy condition, and 15.7% overall.

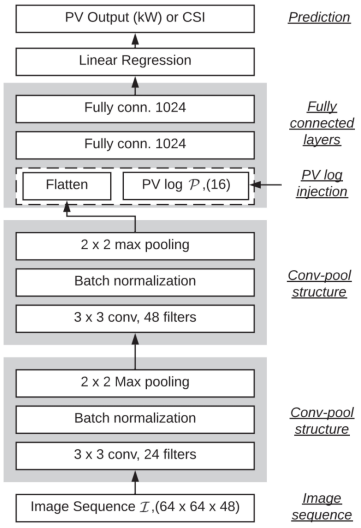


**Figure 55.** SUNSET deep CNN network architecture diagram, with image sequences entering at the bottom, going through layers of operation, and forming an output. 3x3 Conv, 24 denotes a convolutional layer with 24 filters, and each filter with a size of 3x3. Fully conn. 1024 denotes a fully connected layer with 1024 neurons.

#### *1.10.9 Sky Image forecasting with Generative Adversarial Networks for cloud coverage prediction*

In [60], the all-sky images were obtained using a commercial compact digital camera, operating on the roof of the building of Physics Department at the University of Patras - Greece, with a fisheye lens mounted in front of the entrance optics of the camera. The RGB images were stored in JPEG format with spatial resolution 1600x1200 pixels. The whole sky is represented in a circular disk, while no mechanism for shadowing was used in order to obscure the direct solar radiation. The data for the experiments consists of over 1.5 million images obtained by continuous operation of the camera from August 2014 until April 2017. During the experiments, a 4-scale networks framework is used, followed. Each scale's input size is 4x4, 8x8, 16x16 and 32x32. Batch of 8 sequences of images were used during the whole training process. The common criteria for evaluating GANs (e.g. Inception Score) are not applicable for this task since a metric for representing the quality of the generated images with respect to the cloud-based sky image prediction task is needed. This criterion is selected to be the cloud coverage in a percentage manner, which is a measurement with a physical context that fits with the prediction problem. The GANs topology was trained using a subset of the data consisted of 15000 images captured during different days. This subset includes images with varying weather conditions such as sunshine, light cloudy, heavy cloudy and rainy weather. The images that are captured during night hours are not considered since the weather conditions are not distinct and the results can't be evaluated. The test set contains 680 images captured from different days with varying weather conditions; thus, there are images of clear, light cloudy and heavy cloudy sky. For the evaluation, it is ensured that the training set and the test set are non-overlapped since they consisted of images from different days. In order to speed up the training process, images resized to 520x390 pixels from 1600x1200 pixels. The trained model was evaluated on all available 676 test images in order to have an overview of the performance. The average MSE of these 676 sequences is 4.75%. Furthermore, the same process was repeated when the network is trained without using adversarial loss to check for blurrier images. The average MSE for the network without loss is 4.42%. This iterative approach was incurred until 8 sequential images were generated, therefore the forecasting prediction is made for the next 8 minutes (8 generated images) after 4 minutes measurements (4 input images). The authors also developed a forecasting with a many-to-many scheme. In this part of the research, GANs topology was developed in order to predict multiple sequential images simultaneously. The network was designed receiving a sequence of 8 images. This topology was also trained without considering adversarial loss. Having estimated the cloud coverage from all the generated and ground truth images, the Mean Square Error (MSE) for every couple of generated and ground truth image that are available from the dataset is calculated. Analyzing the results the average deviation of the cloud coverage estimation comes about 10% at the 8th predicted image. For investigating the spatial information in the generated images, a segmentation of all the sky images in 17 regions is incurred, as shown in Figure 56. At each segment of the image, the cloud coverage is estimated. This results in a 17-dimensions vector for every image. Then, the Euclidean distance is calculated for every couple of vectors corresponding to the generated and the ground truth images. The results are presented as boxplot graphs and show that both the iterative and many-to-many methods without an adversarial loss, achieve a lower MSE than with it.

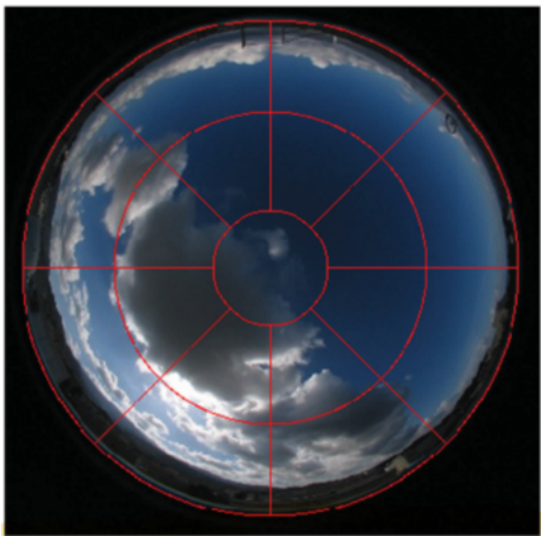

**Figure 56.** Segmentation of sky image in 17 parts. Cloud coverage in each segment was separately calculated.

#### *1.10.10 Sky Image-Based Solar Irradiance Prediction Methodologies Using Artificial Neural Networks*

In [61], sky images and global horizontal irradiance data are used as ANN inputs. The sky images are taken using a waterproof 12-megapixel camera with a fish-eye lens mounted on a 2-axis solar tracker. The sky images are taken with 20-second intervals from July to September 2016 from 10:00 AM to 4:30 PM. The global horizontal irradiance is measured minutely using a pyranometer as the sky images are taken. Five successive sky images taken with 20-second intervals are used for a set of ANN input data. The combination of 5 successive images and 20-seconds intervals are chosen because it takes around 2 minutes or less for the clouds to travel from the outermost sampling points to the center of the sun, depending on the cloud speed. Red-blue-ratio (RBR) values from the sampling points are extracted and used as the ANN inputs. A total of 1,580 sets equivalent to about 11 hours of solar irradiance data and sky images are used for ANN training and testing. Among the 1,580 data sets, 80% is used for training the network, while the remaining 20% is for testing. ANN is selected in this research as a regression method since it does not require prior knowledge of the predicting functions and a traditional ANN is used rather than deep learning because it is suited for sparse data sets and require less data. The ANN configurations and the activation functions are selected by trial and error bases to maximize the $R^2$ value of the training and testing sets during the preliminary analysis. The $R^2$ refers to the coefficient of multiple determination and is used to measure the accuracy of the ANN prediction. The authors developed a one-step method for global horizontal irradiance prediction where a single ANN predicts the global horizontal irradiance directly, by eliminating the cloud movement direction prediction step. The RBR values extracted from the five sky images and the measured global horizontal irradiance values are the inputs for the ANN. The number of the RBR values increases as the number of sampling point axes increases. The ANN generates five outputs, which are global horizontal irradiance in 1 to 5 minutes in advance for any axis. In the 2-step method, two ANNs, ANN-1 and 2, are connected in series. The first network, ANN-1, predicts the cloud movement direction, while the second network, ANN-2, predicts the global horizontal irradiance values by using the output from the first network. In the first step, the RBR values extracted from the five sky images taken consecutively are used as the inputs for the ANN-1 to predict the cloud movement directions. The actual cloud movement direction, which is used for the ANN-1 training and testing, is obtained manually by comparing the five consecutive sky images. In the second step, the RBR values are extracted from the 5 sampling points on an axis that is closest to the predicted cloud movement direction. The outputs for the ANN-2 are predicted global horizontal irradiance values in 1 to 5 minutes in the future. The root mean square error (RMSE) is used to evaluate the accuracy of the solar irradiance prediction results. In order to identify the color information suitable for this research, several color information used in existing methodologies are compared. The prediction errors are calculated from a total of 5460 data sets, which are equivalent to a total of about 91 hours of measurement and results are shown in Figure 57.

#### *1.10.11 Transfer Learning on the Feature Extractions of Sky Images for Solar Power Production*

In [62], the authors propose to use CNN as a regressor instead of a classifier to quantitatively map the sky images to continuous solar irradiance values. They start by training a CNN as a classifier and then utilize the transfer learning technique to obtain the desired regressor. Two classes with labels '0' (the sun is not shaded at all) and '1' (otherwise) are used. When the CNN is constructed as a classifier, the last stage for the network is a softmax function. All available sky images are manually labeled and used to train the AlexNet classification model and fine-tune the network parameters using the accuracy of the validation

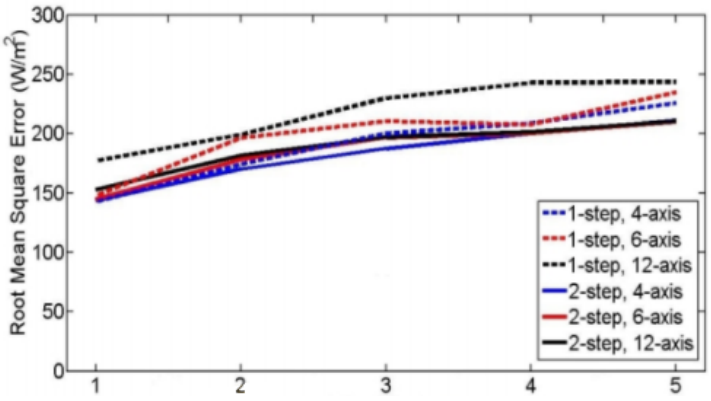


**Figure 57.** Comparison of RMSE values of 2-steps and 1-step methods.

set as the evaluation criteria during the cross-validation process. When the CNN is construced as a regressor all layers except for the final softmax layer of the trained CNN classifier is transferred to the regressor. The softmax layer is replaced by a regression layer to map the sky images to continuous solar irradiance values. For transfer learning, the parameters of the CNN classifier's convolution layers are fixed, while the parameters of the fully connected layers are used as variables that can be updated during the training process. The flow chart of the entire feature extraction framework is shown in Figure 58. The sky images used to validate the approach are obtained from the National Renewable Energy Laboratory (NREL) Solar Radiation Research Laboratory in Denver - USA. A Yankee total-sky imager (TSI-880) is capturing all-sky images at a rate of one image every 10 minutes with time stamps. In addition, global horizontal irradiance measurements are provided also with time stamps, which are used as training data for the development of the CNN regressor. Only sky images during summer time and the corresponding data are considered in the experiments. The images and data cover the time window from 8:00am to 4:00pm in the day and the authors collected 7-year worth of data in June, July and August for the experiments with a total number of images of 21,600. To focus the network to capture the effects of clouds on the solar irradiance, the authors de-trend the data to remove the effects of time. To reduce the complexity and save the cost for manual labeling, they train the classifier with sky images collected over one summer. The CNN as classifier achieves very good accuracy in terms of identifying whether the sun is shaded by clouds or not. The accuracy of the testing set has exceeded 93%, and the accuracy for the training set has reached nearly 98%. For all testing data, the root mean squared error (RMSE) is $130.69 W/m^2$. While without the transfer learning, the RMSE is $187.04 W/m^2$.

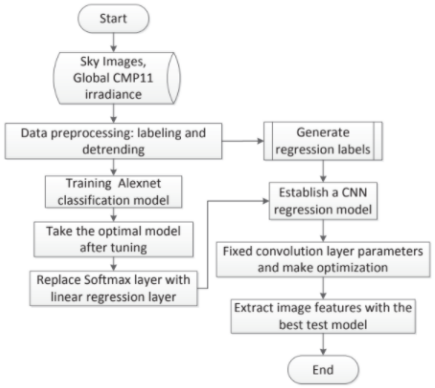


**Figure 58.** Flow chart of feature extraction system based on transfer learning and CNN.

#### *1.10.12 A deep learning approach to solar-irradiance forecasting in sky-videos*

In [63], the authors propose an architecture consisting of two stages: (i) A convolutional neural network stage to encode a frame from a sky-video to obtain a full-sky representation aided by auxiliary weather data, (ii) A two-tier LSTM architecture to observe historical full-sky representations and produce ahead-of-time forecasts. The proposed model can be seen in Figure 59. In the experiments, the average wind speed, barometric pressure, relative humidity, and air temperature are used alongside the Azimuth angle of the sun, which is derived geometrically as a function of geo-coordinate location of the camera and timestamp.

Further, the estimated solar irradiance from a clearsky model is also used which measures the solar irradiance as a Cosine function of the sun's Azimuth angle (z) under the assumption of cloudless skies. A sky-video is obtained from an upward facing wideangle lensed video camera. The obtained images are circular and sample the full-sky region. Based on the configuration of the camera, the sun region may be occluded to prevent image saturation or cameras with anti-blooming filters may be used. The performance of the approach is assessed on two publicly available datasets of sky-videos obtained from two different locations in the United States. Each of the two datasets use different cameras to record the videos. Golden, Colorado Dataset: is recorded at Solar Radiation Research Laboratory (SRRL) where a mechanical sun tracker is used to block the sun to prevent saturation in the image. The dataset is available for the last 12 years from 2004-2016 and the total images captured are 304,309. Tuscan, Arizona Dataset: has been recorded at the Multiple Mirror Telescope Observatory (MMTO). The dataset is available from the months November, 2015 to May, 2016 and 993,101 images are recorded during this period. Both nowcasting and forecasting are performed on these datasets. For the forecasting, predictions are given for the next 4 hours in an interval of 10 minutes. For the nowcasting experiments with and without the aid auxiliary data are performed. The results are reported as normalized mean absolute percentage (nMAP) error of predictions and the performance of the proposed approach is compared along with traditional VGG16 deep learning framework on both the datasets with random weight initialization. The authors avoid data augmentation by orientation or zooming, as they could change the position of sun with respect to the camera. Results show that the nowcasting nMAP trained with weather parameters, as opposed to just sky images, has an overall 1.46 decrease in error in Colorado, and an overall of 36.02 decrease in Arizona dataset. For the forecasting the proposed approach had a decrease in error on both datasets for every the time-window experimented.

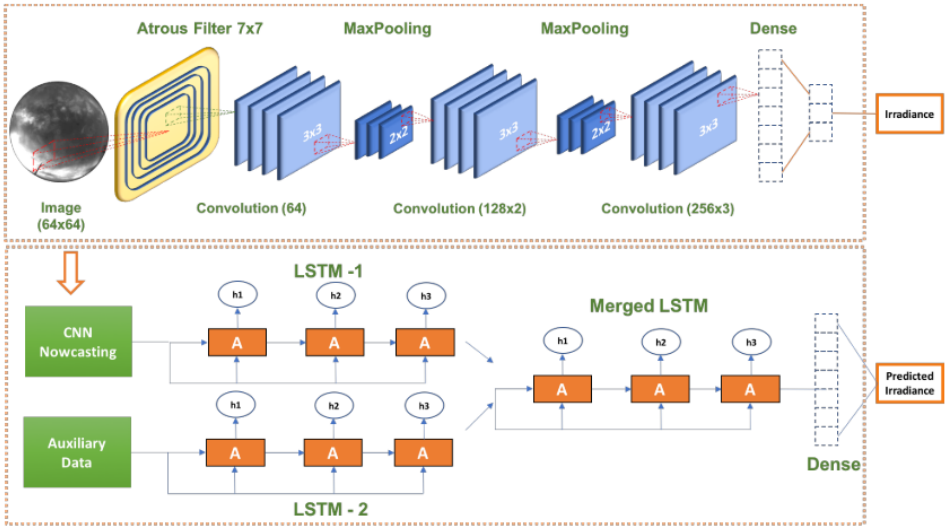


**Figure 59.** The proposed CNN+LSTM based architecture uses auxiliary weather information to guide the training process to produce short-term (between one and four hours ahead) forecasting of solar irradiance.

### *1.10.13 Estimating Solar Irradiance Using Sky Imagers*

In [64], the experimental setup consists of weather stations and ground-based whole-sky imagers (WSIs). These devices are co-located on the rooftop of our university building in Singapore. They continuously capture various meteorological data, and we archive them for subsequent analysis. The authors use the popular toolbox by Scaramuzza et al. for the geometric calibration of the sky imager and use a black-and-white regular checkerboard pattern to calibrate the distortion caused by the fish-eye lens. In addition to the sky imagers, meteorological data is used, such as rainfall, total solar radiation, temperature and pressure at intervals of 1 minute. The authors use a hemispheric sampling and relative luminance computation for each image. This relative luminance value to estimate the solar radiation. The images used to model the solar radiation were captured during the period from January 2016 to August 2016. The solar irradiance is computed as the flux of radiant energy per unit area normal to the direction of flow. The authors attempt to fit a linear model and other higher-order polynomial regressors to model the relationship between image luminance from sky camera images and the measured solar radiation. In order to provide an objective evaluation of the different models, they also compute the RMSE value between the actual and regressed values. The best polynomial presented has 5 degrees and RMSE of 176.49. The authors benchmark the proposed approach against 4 existing models: Hargreaves and Samani (1985); Donatelli and Campbell (1998); Bristow and Campbell (1984); and Hunt et al. (1998). The overall results can be seen on Figure 60(a). Results show that the proposed approach can estimate the solar

radiation accurately with the smallest RMSE compared to other models. The red-blue-ratio (RBR) is used alongside an optical flow technique to obtain the flow field. The authors estimate the future $t+2$ minutes frame, and subsequently the $t+4$ minutes frame. Figure 60(b) illustrates this. A forecast accuracy of 70% is obtained for a prediction lead time up to 6 minutes.

| Methods | RMSE (W/m$^2$) | Correlation |
|---|---|---|
| Proposed approach | **178.27** | **0.86** |
| Hargreaves and Samani (1985) | 982.35 | 0.67 |
| Donatelli and Campbell (1998) | 324.48 | 0.67 |
| Bristow and Campbell (1984) | 318.07 | 0.68 |
| Hunt et al. (1998) | 922.66 | 0.65 |

(a)

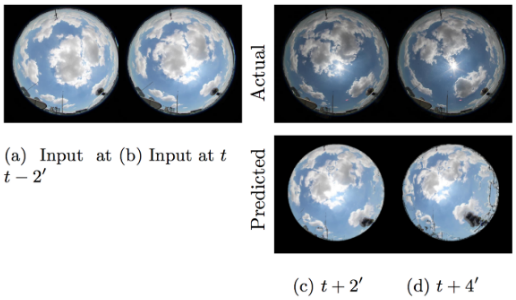


(a) Input at $t-2'$ (b) Input at $t$

(c) $t+2'$ (d) $t+4'$

(b)

**Figure 60.** (a) Benchmarking of the proposed approach with other solar radiation estimation models. (b) Prediction of sky/cloud image using optical flow technique.

#### *1.10.14 Very short-term solar irradiance forecast using all-sky imaging and real-time irradiance measurements*

The author from [65] proposes a hybrid forecast method to predict the solar irradiance up to ten minutes in advance. The first step of the method is responsible to detect the clouds, it uses the Fixed Threshold and Clear Sky Library method with adaptive threshold applied to the image's red to blue ratio. The second step estimates the cloud motion, to accomplish this step the author undoes the optical system equisolid angle projection then applies a cross-correlation method described in Hamill and Nehkorn. Then a ladder grid of elements, that can be seen on figure 61, is constructed, with the origin in the sun's position to the mean displacement vector, to forecast direct normal irradiance in a custom model made by the author. The validation was done with a sample of 5230 forecasting time points, spread over a six-month period.

#### *1.10.15 Inter-hour direct normal irradiance forecast with multiple data types and time-series*

In [66] the author uses multiple data types as images and numerical time-series to forecast irradiance. The images were captured by a Sky Imager, every 30 seconds, and measured data employed were downloaded from the open database of the Solar Radiation Research Laboratory, which was provided by the National Renewable Energy Laboratory (NREL). The sun position was extracted from the images, using the zenith and azimuth angle, and cloud detection algorithms as Clear-Sky Background Different and Red to Blue Ratio were used to detect the clouds and identify the error pixels, pixels from the sun that were identified as clouds. The images were also in-painted and corrected to obtain a better information from the sky. The cloud motion was calculated using the centroid of the clouds from two different images and the linear regression between wind and cloud direction was calculated to verify the relationship between them. Finally, a support vector regression model using: cloud cover, clear-sky index, wind speed and humidity was employed to predict the irradiation for the next 10 minutes. The whole pipeline process can be seen in the figure 62. The experiment achieved a 34% of nRMSE improvement over the persistent model.

### 1.11 2020

#### *1.11.1 Cloud motion estimation from small-scale irradiance sensor networks: General analysis and proposal of a new method*

In [67], the authors implemented a synthetic framework in order to generate time series for irradiance monitoring networks according to a given cloud motion vector (CMV). The authros used a fractal cloud model to simulate irradiance fields of 8192 m x 8192 m with a resolution of 1 m. In each iteration, the algorithm gives values to the central pixels by adding the arithmetic mean of the corners to a Gaussian variable whose standard deviation depends on the chosen fractal dimension, so that smaller squares are generated. The cloud motion is simulated by displacing the obtained irradiance field over a monitoring domain according to the given CMV and sampling period, as show in Figure 63. The authors use the most correlated pair (MCP) method. The estimated cloud motion direction is given by the line defined by the two concerned sensors. The MCP method is affected by noise produced by the inaccuracies in the determination of time lags, and raw results are quality controlled in the following aspects: (i) CMVs with low correlation coefficient are excluded and (ii) unphysical speeds and direction outliers are discarded. The Linear Cloud Edge (LCE) method works with a triplet of sensors, assuming linear edges of the observed part of the clouds and is also used by the authors. The LCE method has been implemented with two modifications: the time window for the search of global maxima is adapted to the sampling rate and the distance between sensors in order

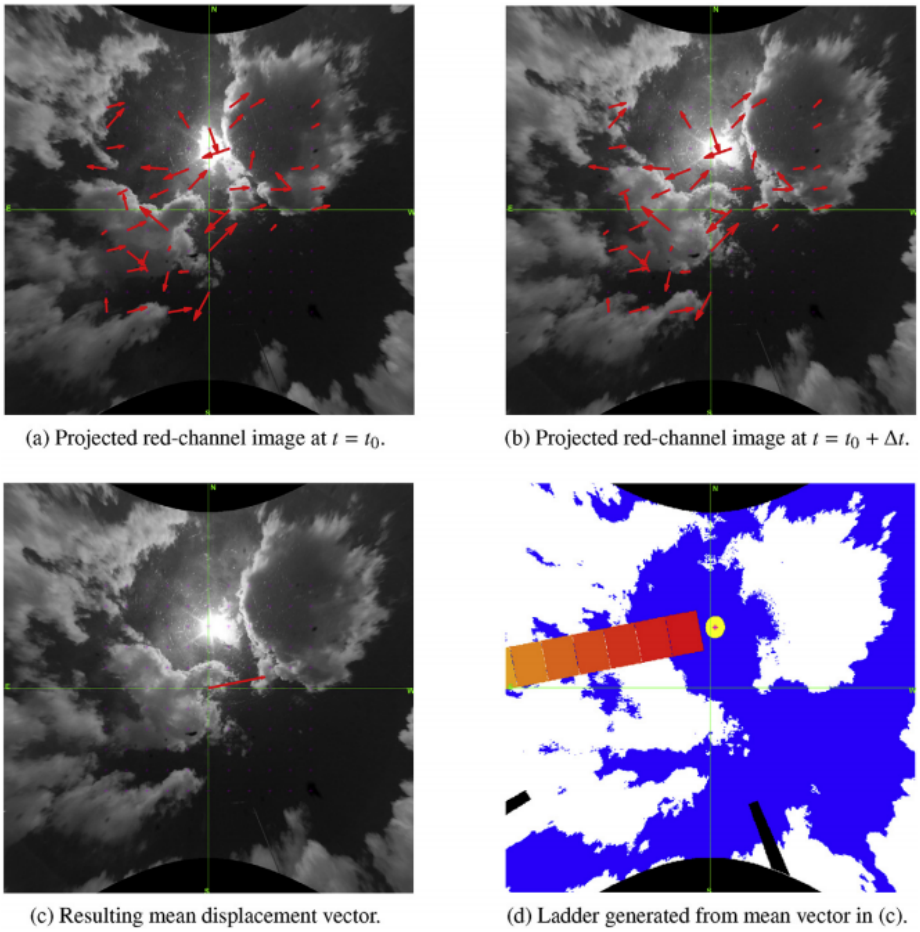

(a) Projected red-channel image at $t = t_0$.

(b) Projected red-channel image at $t = t_0 + \Delta t$.

(c) Resulting mean displacement vector.

(d) Ladder generated from mean vector in (c).

**Figure 61.** Results of the CCM algorithm for computing the mean cloud displacement. Vectors shown in (a) and (b) are those having cc > 0.8.

to capture minimum speeds of 3 m/s, (ii) the quality control is based on measurement of 5 min, where the unphysical cloud speeds has also been considered as outliers applying the quality control. The proposed formulations of the cross-correlation method (CCM) are limited by the convolution, which is not able to provide reliable similarity measures under the particular conditions of small-scale irradiance sensor networks, therefore the convolution is replaced by the mean absolute error (MAE) and consequently, the search of the maximum cross-correlation coefficient is also replaced by the search of the minimum MAE. A series of tests have been performed considering different network layouts by varying the number of sensors, sizes of the monitored area, and sampling periods. Concretely, configurations of 9 ($n = 3$), 16 ($n = 4$), 36 ($n = 6$) and 100 ($n = 10$) sensors with side lengths of 10, 30, 50 and 100 m were chosen. Once a configuration is chosen, 100 CMVs were randomly generated with speeds ranging from 0 to 30 m/s and directions ranging from 0 to 360º. The simulated sequences were forced to include more than 150 s of irradiance variability in order to assure enough cloud passing information to perform the estimations. The three methods (MCP, LCE and CMAE) were applied to each sequence with known CMV. The CMAE shows the best performance in all cases, specially in those networks with a high spatial density of sensors. Thus, the CMAE method achieved a root mean square error (RMSE) value of 1.4 m/s with the highest density network ($n = 10$, $L = 30m$, 1 sensor per 9.0 $m^2$), while the MCP and LCE obtained 6.5 m/s, and 5.6 m/s, respectively. On the other hand, the RMSE values for the lowest density network ($n = 3$, $L = 100m$, 1 sensor per 1111.1 $m^2$) were 5.7 m/s, 8.4 m/s, and 9.2 m/s for the CMAE, MCP and LCE, respectively. The two intermediate cases help to complete the scenario. The network $n = 6$, $L = 50m$ (1 sensor per 69.4 $m^2$) provided RMSE values of 1.2 m/s, 6.2 m/s, and 8.3 m/s; and the network $n = 4$, $L = 50m$ (1 sensor per 156.3 $m^2$) provided values of 3.2 m/s, 7.3 m/s, and 6.7 m/s for the CMAE, LCE and MCP, respectively.

#### *1.11.2 Short Term Prediction of Solar Irradiance Fluctuation Using Image Processing with ResNet*

In [68], sky images were captured at 1280x960 pixel resolution using a SJCAM-SJ4000 camera pointing to the sky. The camera was installed at the Department of Electrical Engineering building, in Bangkok - Thailand. Sky images were captured every

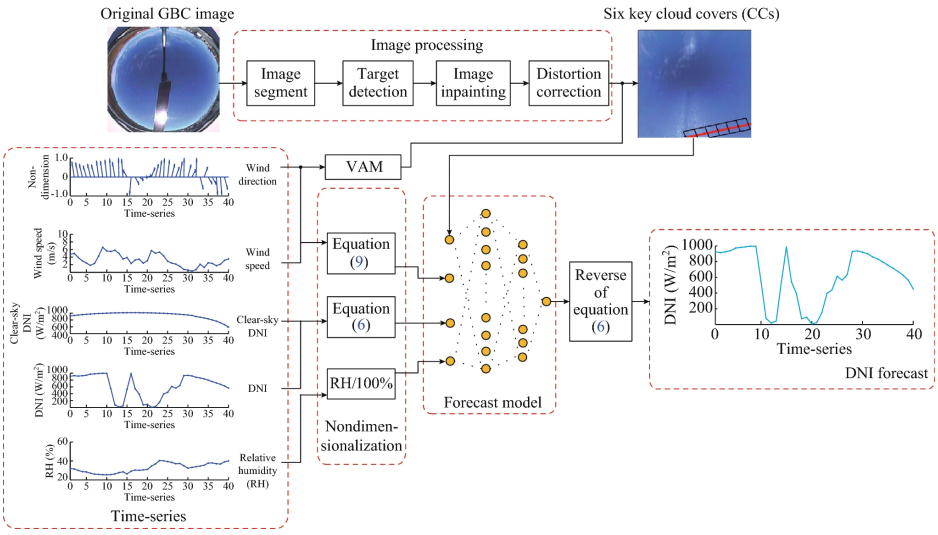


**Figure 62.** Structure chart of DNI forecast framework based on multiple time-series and GBC images.

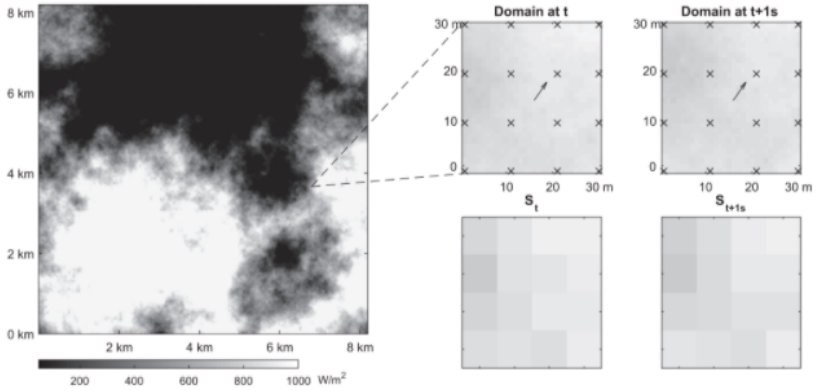


**Figure 63.** Generation of snapshots. Left graph: irradiance map derived from the fractal cloud model. Right upper graphs: zoom and evolution of the monitored domains for a given cloud motion vector (represented in the center of the graphs), the position of the sensors is indicated with 'x'. Right lower graphs: Snapshots provided by the 4-by-4 array of sensors.

20 seconds automatically. Images are converted to the red-blue-ratio and the position of the Sun is located by using Hough transform technique. The vector direction and velocity of a moving cloud are estimated from images using the Farneback method. The final image is resized to 256x256 pixels. Cloud motion vector image and the position of the sun are used as inputs for the CNN and the network generates a trigger when there is an event. The proposed solution is based on the ResNet-101 architecture. Motion vectors image from sky images captured from November 2018 to January 2020 for 20 days and during 10:00 am to 3:00 pm were used to train the network. The sky images were captured in clearly day, cloudy day and in solar eclipse for testing the developed algorithm to see if it could raise trigger for the sun coverage events. In Figure 64 shows the solution to generate a trigger to notify the system. In the first image take at figure 6(a), cloud motion vector is generated. 2 minute later figure 6(b), the system found that the motion of the cloud has a tendency to cover some parts of the Sun, therefore the trigger is generated and at 11:19 as shown in figure 6(c) a part of the sun was covered by clouds. The overall result shows an error as 27.78% for 6 days of test data. In clearly day for 2 days testing data, the system accuracy is high. There were 4 sun coverage events. The system raises the correct trigger totally 4 times. Error in the cloudy day is 27.50%, it is higher more than errors in clearly day. And errors in solar eclipse day is 40%, that is highest in all data for testing the system.

### *1.11.3 Convolutional Neural Networks applied to sky images for short-term solar irradiance forecasting*

In [69], the dataset used in this study originated from the SIRTA laboratory Haeffelin (2005), France. Samples were collected over a period of seven months from March 2018 to September 2018. Images of the sky have RGB resolution of 768x1024 pixels. Samples are taken every two minutes and composed of two images with different exposures. The proposed model

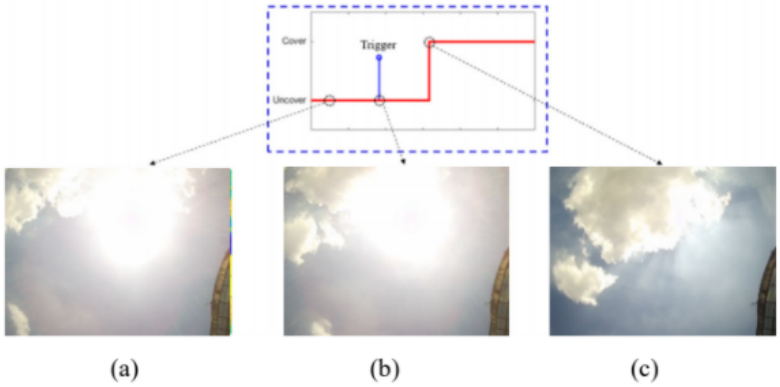


**Figure 64.** Example of the case that raising trigger events on 13 March 2018 (a) at 11:17h, (b) at 11:19h, (c) at 11:21h.

follows the configuration presented in Figure 65(a). It is composed of two distinct networks merged into one which output the irradiance estimate. On the one side, a CNN made of ResNet units is used to extract features from sky images and on the other side, an ANN treats available auxiliary data (past irradiance measurements, angular position of the sun, etc). Both outputs are fed into another ANN, which integrates them to give its prediction. Each sample given to the network is composed of four images in total where each 2D input was originally downsized to a grey scale 150x150 pixels resolution. In parallel, metadata are made of the past irradiance measurements at time $t$ and $(t-2)$ min, the angular position of the sun at time $t$ is defined by its Zenith and Azimuthal angles, plus the cosine and sine of those angles. The assessment of the model was performed on a setting of the training and the validation sets composed of 16,000 and 4000 samples respectively. The loss function used by the model as a reference to assess its own performance is the unregularised MSE. Hyperparameter tuning was performed to achieve the best forecasting performance on the 10-min ahead forecast. The same network architecture has been used to train models for the 2-min to 20-min ahead forecasts. Figure 65(b) shows the performance of the model obtained with the same architecture for different time windows from 2 to 20-min.

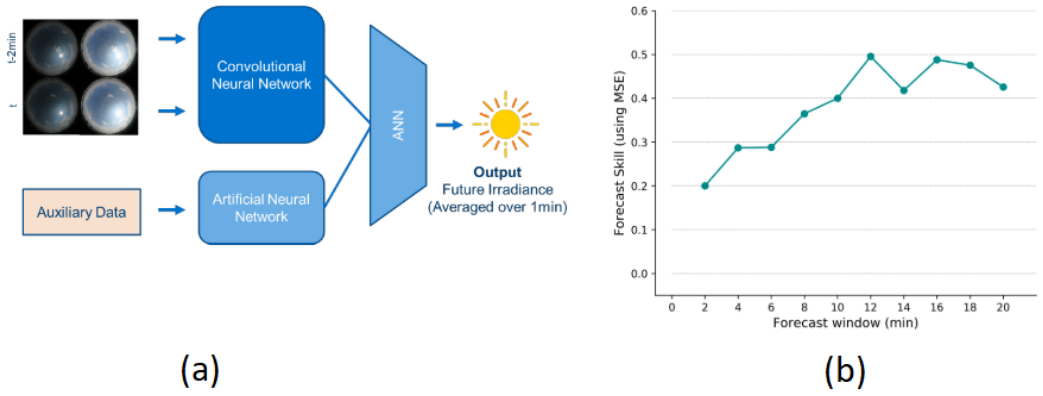


**Figure 65.** (a) Schematic network architecture. (b) Forecasting skill on the validation set using the MSE based on the smart persistence model for different time windows, the training and validation sets being generated from different days.

## Discussion

Most of the studies use a segmentation method to extract meaningful statistics from the captured images. Table 4 summarizes the utilized methods of the works included in this review.

Even though most works use a segmentation method we can see that this is not applicable to almost 1/3 of all the articles. This is mainly due to the use of a machine learning technique that has the ability to extract meaningful statistics from the data (images) by itself. The most used methods are RBR (Reb-blue-ratio), a fixed threshold, a mix of both RGB (Red-green-blue) and RBR features, and grayscale. The RBR is used to elaborate some sort of threshold where sky pixels are expected to have a lower ratio because of their higher blue saturation, facilitating the segmentation of sky x clouds. The imposed thresholds could be fixed or adaptive. We can see that 7 works use fixed thresholds, which ends up being a localized threshold that most likely

will not be able to perfom well on a different location, with different weather conditions. The grayscale is one of the most common methods for segmentation in computer vision due to eliminating the need to work with 3 dimensions (RGB), making it easy to compute statistics from an image. Grayscale images work in the range of 0-255, where 0 is a black pixel and 255 is a white pixel. In the context of cloud image segmentation, the grayscale can also be used to create a fixed or adaptive threshold to segregate clouds from sky, which tend to have values closer to 255. Most works use a Total Sky-imager (TSI), with only 8 (12.3%) articles using another type of cameras. This shows a limitation when extracting features from the images, since TSIs are pointed to the zenith, the images don't capture the cloud's height. This problem can be solved by having a camera pointing to the horizon, even though a single camera would not be able to capture the entire sky, this could be mitigated by pointing the camera to the most predominant direction from where the wind flows. Nevertheless, the authors believe that this is a potential subject to be worked on in future works.

As Figure 66 most forecasting techniques still rely on classical statistics methods (38 in total). However, as the authors hypothesized, we can observe a change from 2018 and further years from classical to machine learning approaches (27 in total). Still the number of works relying on classical approaches is still relevant in the subject of forecasting solar power generation. As we can see 2017 was the year with most articles published using this approach of all the results obtained in this SLR. In summary, during the last decade there was approximately 2.7 articles being published every year using a machine learning approach with a standard deviation of 3.19, meanwhile there was approximately 3.8 articles being published using a classical statistics approach for the same problem with a standard deviation of 2.44. Therefore we can conclude that even though there is an apparent increase of interest in machine learning during the last 3 years, the use of classical approaches still dominate overall.

| Year of Publication ▲ | ML | Classic |
|---|---|---|
| 2011 | 0 | 1 |
| 2012 | 0 | 3 |
| 2013 | 2 | 1 |
| 2014 | 1 | 6 |
| 2015 | 3 | 5 |
| 2016 | 1 | 4 |
| 2017 | 1 | 8 |
| 2018 | 8 | 3 |
| 2019 | 9 | 6 |
| 2020 | 2 | 1 |

**Figure 66.** Amount of articles utilizing a "classical" vs. machine learning approach for forecasting.

By looking at Table 5 we can see a dominance by the United States (USA) in regards of data sets used. This can likely be explained by the sheer amount of focus on research of the countries, however we can neither confirm or deny it. From all the works presented, 19 of them did not express the location of the data used in the proposed approach, which represents 29.23% of all articles. This shows us two things: 1) there's a need for more data sets available from other countries and 2) authors most likely use local data that they do not wish to provide publicly. By having more data sets from other countries and more data sets in general, it's possible to validate and assess the quality of past works as well as apply approaches to different countries than were the data was collected from. Machine learning in special can benefit from that in regards of generality of past (and new) models proposed.

As we can see in Figure 67, the most used type of data for forecasting it's the image (or a sequence of images) itself. There were 37 works relying entirely on the image and it's characteristics to provide a forecast of solar power generation and 28 papers that used meteorological (e.g. direct normal radiance, global horizon irradiance, solar position, power generation) data and images. Even though image-based models can predict cloud motion well, we believe that by adding meteorological more robust models that can reflect the real power generation can be created, specially when dealing with machine learning approaches. Most models can benefit from past information when used as metadata during training. Nevertheless this proportion can be explained due to the amount of works based on classical statistical models only.

Most works (50.76%) don't inform if a cloud motion analysis was performed. The most used approach for this subject is the optical flow approach, which can be seen in Figure 68 as Lucas-Kanade, Gunnar-Farneback and Horn/Schunck, totaling 8 articles utilizing these methods. Alongside is the Cross correlation method, with 7 articles using it. Optical flow is the pattern of apparent motion of objects in general in a visual scene caused by the relative motion between an observer and a scene. Cross-correlation is used to calculate the similarity of two different spectra. Both approaches depend on the time

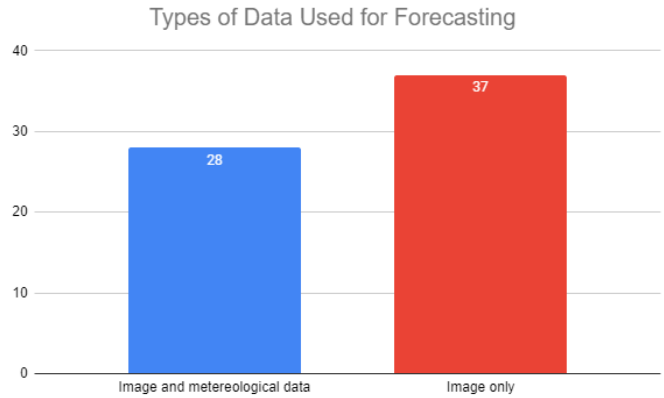


**Figure 67.** Amount of types of data used for forecasting.

resolution between images where a larger resolution leads to a less accurate motion vector. These methods can be used directly to perform a forecast when using a classical approach or as a independent feature when using a machine learning approach. On Figure 69 we can see that the classical approach is the most used, totaling 37 works (56.92%). However when looking at the works proposing a machine learning approach we can see that Artificial Neural Networks (ANN), Convolutional Neural Networks (CNN) and Multilayer Perceptrons (MLP) are the most used models to predict solar power generation. This result is mainly given by the ease of implementing those types of networks and due to the nature of the data used. Convolutional neural networks' (CNN) main focus is on the image domain whereas ANN's and MLP's are good for forecasting in general, depending on the designed architecture. With that in mind authors used CNNs to extract meaningful information over the images and predict the solar power generation using well-grounded neural networks. Our results only obtained 2 works using Long Short-term Memory approaches, which leads us to believe that either our search-strings can be refined to include more works using this methodology or there's not a significant focus on Recurrent Neural Networks at the moment for the subject of solar power nowcasting. Both works present good results with the first one in [44] showing that even with longer time horizons, the proposed approach still achieves low error under clear skies and outperforms the persistence model with an SS-MAE (Skill Score Mean Average Error) of 16.4% and SS-RMSE (Skill Score Root Mean Square Error) of 11.5% for 2-min horizon, an SS-MAE of 14.4% and SS-RMSE of 10.4% for 5-min horizon, and an SS-MAE of 12.1% and SS-RMSE of 7.7% for 10-min horizon. The second one in [63], show that the nowcasting nMAP (normalized Mean Average Precision) trained with weather parameters, as opposed to just sky images, has an overall 1.46 decrease in error in one dataset, and an overall of 36.02 decrease in another dataset used, as well as having a decreased error on both datasets for every time-window experimented.

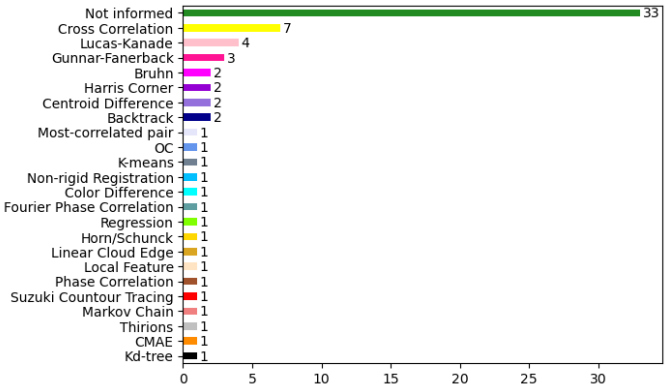


**Figure 68.** Methods for detecting cloud movements.

We can see in Figure 70 that the Root Mean Square Error (RMSE) is the most used error metric, which is a frequently used metric error used to calculate the difference between predicted values from observed ones. The RMSE is also known as Root Mean Square Deviation, which leads to a total of 32 works using this metric to validate their proposed models. The Matching Error and Mean Absolute Error (MAE) are the next leading metrics with 17 and 16 works using them as metrics, respectively. The Matching Error is a simple metric that calculates the exact difference between the predicted values from the

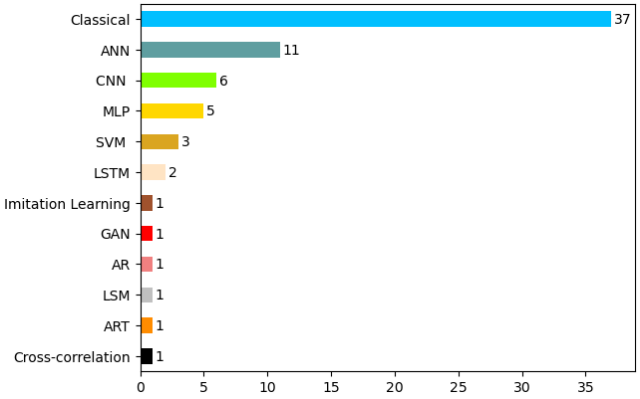


**Figure 69.** Forecasting techniques.

observed values and the MAE is very similar, it calculates the mean of exact difference between values. If we consider the concept of the Matching Error and MAE as the same we have that these two are the most used error metrics by the resulting works. The authors believe that this shows a lack of proper validation of proposed methods in this area, specially the ones utilizing a machine learning approach with images as their inputs. These models can have different validations for different tasks, for example a CNN network can be validated by means of Average, Precision and IoU (Intersection over Union) during the cloud detection/classification step.

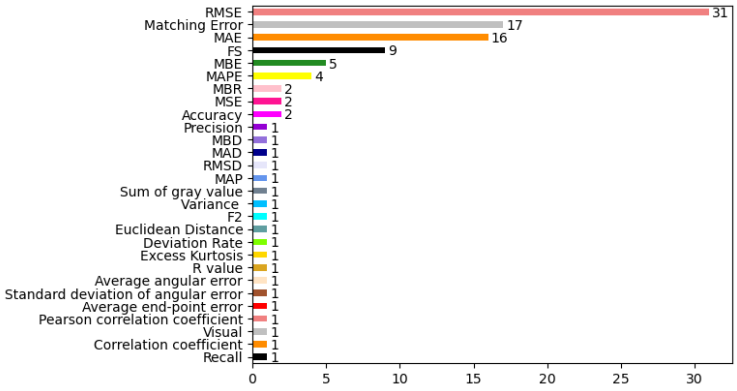


**Figure 70.** Error metrics.

| Method | Amount |
|---|---|
| N/A | 21 |
| RBR | 14 |
| Fixed Threshold | 7 |
| RGB/RBR | 6 |
| Grayscale | 5 |
| Otsu | 3 |
| HSV | 3 |
| Normalized RBR | 3 |
| Histogram | 2 |
| SVM | 2 |
| RBD | 2 |
| LOG | 1 |
| Variance | 1 |
| Clear Sky Library | 1 |
| Color-invariance | 1 |
| Trained Classifier | 1 |
| Clear-sky Background Difference | 1 |
| Entropy | 1 |
| Local Patterns | 1 |
| KNN | 1 |
| K-means | 1 |
| Luminance | 1 |
| CNN | 1 |
| Transmittance | 1 |
| Adaptive Threshold | 1 |
| Co-occurence Matrix | 1 |
| Pixel Averaging | 1 |
| PCA | 1 |
| Laplacian of Gaussian | 1 |
| BGR | 1 |
| HSL | 1 |
| Fourier Transform | 1 |
| Manual | 1 |
| RGB | 1 |
| Genetic Algorithm | 1 |
| Standard Deviation | 1 |

**Table 4.** Amount of articles aggregated by the segmentation method used.

| Country | Amount |
|---|---|
| USA | 20 |
| Not informed | 19 |
| China | 7 |
| Taiwan | 3 |
| France | 3 |
| Singapore | 2 |
| Germany | 2 |
| Spain | 1 |
| Australia | 1 |
| Uruguay | 1 |
| Thailand | 1 |
| Italy | 1 |
| Papua New Guinea | 1 |
| Japan | 1 |
| Greece | 1 |

**Table 5.** Amount of data sets by country.

## References


[1] World Meteorological Organization. *Guide to Meteorological Instruments and Methods of Observations*. 2008. URL: http://www.wmo.int/pages/prog/gcos/documents/gruanmanuals/CIMO/CIMO_Guide-7th_Edition-2008.pdf.

[2] Quan Tang et al. *Attention-guided Chained Context Aggregation for Semantic Segmentation*. 2021. arXiv: 2002.12041 [cs.CV].

[3] Ian Marius Peters and Tonio Buonassisi. *On Climate Change and Photovoltaic Energy Production*. 2019. arXiv: 1908.00623 [physics.soc-ph].

[4] Hung D. Nguyen and Konstantin Turitsyn. *Voltage multi-stability in distribution grids with power flow reversal*. 2014. arXiv: 1404.6581 [nlin.CD].

[5] Chi Wai Chow et al. "Intra-hour forecasting with a total sky imager at the UC San Diego solar energy testbed". In: *Solar Energy* 85.11 (2011), pp. 2881–2893. ISSN: 0038-092X. DOI: https://doi.org/10.1016/j.solener.2011.08.025. URL: http://www.sciencedirect.com/science/article/pii/S0038092X11002982.

[6] V. P. A. Lonij et al. "Forecasts of PV power output using power measurements of 80 residential PV installs". In: *2012 38th IEEE Photovoltaic Specialists Conference*. 2012, pp. 003300–003305. DOI: 10.1109/PVSC.2012.6318280.

[7] K. Stefferud, J. Kleissl, and J. Schoene. "Solar forecasting and variability analyses using sky camera cloud detection motion vectors". In: *2012 IEEE Power and Energy Society General Meeting*. 2012, pp. 1–6. DOI: 10.1109/PESGM.2012.6345434.

[8] Hao Huang et al. "Correlation and Local Feature Based Cloud Motion Estimation". In: MDMKDD '12. Beijing, China: Association for Computing Machinery, 2012, pp. 1–9. ISBN: 9781450315562. DOI: 10.1145/2343862.2343863. URL: https://doi.org/10.1145/2343862.2343863.

[9] Yinghao Chu, Hugo T.C. Pedro, and Carlos F.M. Coimbra. "Hybrid intra-hour DNI forecasts with sky image processing enhanced by stochastic learning". In: *Solar Energy* 98 (2013), pp. 592–603. ISSN: 0038-092X. DOI: https://doi.org/10.1016/j.solener.2013.10.020. URL: http://www.sciencedirect.com/science/article/pii/S0038092X13004325.

[10] Ricardo Marquez and Carlos F.M. Coimbra. "Intra-hour DNI forecasting based on cloud tracking image analysis". In: *Solar Energy* 91 (2013), pp. 327–336. ISSN: 0038-092X. DOI: https://doi.org/10.1016/j.solener.2012.09.018. URL: http://www.sciencedirect.com/science/article/pii/S0038092X1200343X.

[11] A. Mammoli et al. "Low-cost solar micro-forecasts for PV smoothing". In: *2013 1st IEEE Conference on Technologies for Sustainability (SusTech)*. 2013, pp. 238–243. DOI: 10.1109/SusTech.2013.6617327.

[12] Hsu-Yung Cheng, Chih-Chang Yu, and Sian-Jing Lin. "Bi-model short-term solar irradiance prediction using support vector regressors". In: *Energy* 70 (2014), pp. 121–127. ISSN: 0360-5442. DOI: https://doi.org/10.1016/j.energy.2014.03.096. URL: http://www.sciencedirect.com/science/article/pii/S0360544214003600.

[13] S. Quesada-Ruiz et al. "Cloud-tracking methodology for intra-hour DNI forecasting". In: *Solar Energy* 102 (2014), pp. 267–275. ISSN: 0038-092X. DOI: https://doi.org/10.1016/j.solener.2014.01.030. URL: http://www.sciencedirect.com/science/article/pii/S0038092X14000486.

[14] A. Radovan and Ž. Ban. "Predictions of cloud movements and the sun cover duration". In: *2014 37th International Convention on Information and Communication Technology, Electronics and Microelectronics (MIPRO)*. 2014, pp. 1210–1215. DOI: 10.1109/MIPRO.2014.6859752.

[15] S. Sun et al. "Short term cloud coverage prediction using ground based all sky imager". In: *2014 IEEE International Conference on Smart Grid Communications (SmartGridComm)*. 2014, pp. 121–126. DOI: 10.1109/SmartGridComm.2014.7007633.

[16] D. Cai et al. "Short-term solar photovoltaic irradiation predicting using a nonlinear prediction method". In: *2014 IEEE PES General Meeting | Conference Exposition*. 2014, pp. 1–5. DOI: 10.1109/PESGM.2014.6939406.

[17] Handa Yang et al. "Solar irradiance forecasting using a ground-based sky imager developed at UC San Diego". In: *Solar Energy* 103 (2014), pp. 502–524. ISSN: 0038-092X. DOI: https://doi.org/10.1016/j.solener.2014.02.044. URL: http://www.sciencedirect.com/science/article/pii/S0038092X14001327.

[18] David Bernecker et al. “Continuous short-term irradiance forecasts using sky images”. In: *Solar Energy* 110 (2014), pp. 303–315. ISSN: 0038-092X. DOI: https://doi.org/10.1016/j.solener.2014.09.005. URL: https://www.sciencedirect.com/science/article/pii/S0038092X14004356.

[19] F. Su et al. “A local features-based approach to all-sky image prediction”. In: *IBM Journal of Research and Development* 59.2/3 (2015), 6:1–6:10. DOI: 10.1147/JRD.2015.2397772.

[20] B. Guanjun et al. “An ultra-short-term power prediction model based on machine vision for distributed photovoltaic system”. In: *2015 IEEE International Conference on Information and Automation*. 2015, pp. 1148–1152. DOI: 10.1109/ICInfA.2015.7279459.

[21] Chi Wai Chow, Serge Belongie, and Jan Kleissl. “Cloud motion and stability estimation for intra-hour solar forecasting”. In: *Solar Energy* 115 (2015), pp. 645–655. ISSN: 0038-092X. DOI: https://doi.org/10.1016/j.solener.2015.03.030. URL: http://www.sciencedirect.com/science/article/pii/S0038092X15001565.

[22] Hsu-Yung Cheng and Chih-Chang Yu. “Multi-model solar irradiance prediction based on automatic cloud classification”. In: *Energy* 91 (2015), pp. 579–587. ISSN: 0360-5442. DOI: https://doi.org/10.1016/j.energy.2015.08.075. URL: http://www.sciencedirect.com/science/article/pii/S0360544215011512.

[23] Yinghao Chu et al. “Real-time forecasting of solar irradiance ramps with smart image processing”. In: *Solar Energy* 114 (2015), pp. 91–104. ISSN: 0038-092X. DOI: https://doi.org/10.1016/j.solener.2015.01.024. URL: http://www.sciencedirect.com/science/article/pii/S0038092X15000389.

[24] J. Alonso-Montesinos, F.J. Batlles, and C. Portillo. “Solar irradiance forecasting at one-minute intervals for different sky conditions using sky camera images”. In: *Energy Conversion and Management* 105 (2015), pp. 1166–1177. ISSN: 0196-8904. DOI: https://doi.org/10.1016/j.enconman.2015.09.001. URL: http://www.sciencedirect.com/science/article/pii/S0196890415008365.

[25] Zhenzhou Peng et al. “3D cloud detection and tracking system for solar forecast using multiple sky imagers”. In: *Solar Energy* 118 (2015), pp. 496–519. ISSN: 0038-092X. DOI: https://doi.org/10.1016/j.solener.2015.05.037. URL: https://www.sciencedirect.com/science/article/pii/S0038092X15002972.

[26] Jin Xu et al. “Solar Irradiance Forecasting Using Multi-Layer Cloud Tracking and Numerical Weather Prediction”. In: *Proceedings of the 30th Annual ACM Symposium on Applied Computing*. SAC ’15. Salamanca, Spain: Association for Computing Machinery, 2015, pp. 2225–2230. ISBN: 9781450331968. DOI: 10.1145/2695664.2695812. URL: https://doi.org/10.1145/2695664.2695812.

[27] Zhenzhou Peng et al. “A hybrid approach to estimate the complex motions of clouds in sky images”. In: *Solar Energy* 138 (Nov. 2016), pp. 10–25. DOI: 10.1016/j.solener.2016.09.002.

[28] S. Dev et al. “Estimation of solar irradiance using ground-based whole sky imagers”. In: *2016 IEEE International Geoscience and Remote Sensing Symposium (IGARSS)*. 2016, pp. 7236–7239. DOI: 10.1109/IGARSS.2016.7730887.

[29] T. Koyasu et al. “Forecasting variation of solar radiation and movement of cloud by sky image data”. In: *2016 IEEE International Conference on Renewable Energy Research and Applications (ICRERA)*. 2016, pp. 401–406. DOI: 10.1109/ICRERA.2016.7884369.

[30] S. Moughyt et al. “Sky status: A local analysis of ground based digital images”. In: *2016 5th International Conference on Multimedia Computing and Systems (ICMCS)*. 2016, pp. 667–670. DOI: 10.1109/ICMCS.2016.7905628.

[31] M. Cervantes et al. “Utilization of Low Cost, Sky-Imaging Technology for Irradiance Forecasting of Distributed Solar Generation”. In: *2016 IEEE Green Technologies Conference (GreenTech)*. 2016, pp. 142–146. DOI: 10.1109/GreenTech.2016.33.

[32] Benjamin Kurtz, Felipe Mejia, and Jan Kleissl. “A virtual sky imager testbed for solar energy forecasting”. In: *Solar Energy* 158 (2017), pp. 753–759. ISSN: 0038-092X. DOI: https://doi.org/10.1016/j.solener.2017.10.036. URL: http://www.sciencedirect.com/science/article/pii/S0038092X1730899X.

[33] M. Saleh et al. “Battery-Less Short-Term Smoothing of Photovoltaic Generation Using Sky Camera”. In: *IEEE Transactions on Industrial Informatics* 14.2 (2018), pp. 403–414. DOI: 10.1109/TII.2017.2767038.

[34] D. M. L. H. Dissawa et al. “Cloud motion tracking for short-term on-site cloud coverage prediction”. In: *2017 Seventeenth International Conference on Advances in ICT for Emerging Regions (ICTer)*. 2017, pp. 1–6. DOI: 10.1109/ICTER.2017.8257803.

[35] M. Chang et al. “Cloud tracking for solar irradiance prediction”. In: *2017 IEEE International Conference on Image Processing (ICIP)*. 2017, pp. 4387–4391. DOI: 10.1109/ICIP.2017.8297111.

[36] Walter Richardson et al. “Machine learning versus ray-tracing to forecast irradiance for an edge-computing SkyImager”. In: Sept. 2017, pp. 1–6. DOI: 10.1109/ISAP.2017.8071425.

[37] Julien Nou et al. “Towards the short-term forecasting of direct normal irradiance using a sky imager”. In: *IFAC-PapersOnLine* 50.1 (2017). 20th IFAC World Congress, pp. 14137–14142. ISSN: 2405-8963. DOI: https://doi.org/10.1016/j.ifacol.2017.08.1856. URL: http://www.sciencedirect.com/science/article/pii/S2405896317324813.

[38] Z. Xiang et al. “Very short-term prediction model for photovoltaic power based on improving the total sky cloud image recognition”. In: *The Journal of Engineering* 2017.13 (2017), pp. 1947–1952. DOI: 10.1049/joe.2017.0669.

[39] Zhao Zhen et al. “Research on a cloud image forecasting approach for solar power forecasting”. In: *Energy Procedia* 142 (2017). Proceedings of the 9th International Conference on Applied Energy, pp. 362–368. ISSN: 1876-6102. DOI: https://doi.org/10.1016/j.egypro.2017.12.057. URL: https://www.sciencedirect.com/science/article/pii/S1876610217357855.

[40] Hsu-Yung Cheng. “Cloud tracking using clusters of feature points for accurate solar irradiance nowcasting”. In: *Renewable Energy* 104 (2017), pp. 281–289. ISSN: 0960-1481. DOI: https://doi.org/10.1016/j.renene.2016.12.023. URL: https://www.sciencedirect.com/science/article/pii/S0960148116310710.

[41] David Cañadillas Ramallo et al. “A low-cost two-camera sky-imager ground-based intra-hour solar forecasting system with cloud base height estimation capabilities working in a smart grid”. In: June 2018, pp. 2282–2287. DOI: 10.1109/PVSC.2018.8548294.

[42] Keyong Hu et al. “A new ultra-short-term photovoltaic power prediction model based on ground-based cloud images”. In: *Journal of Cleaner Production* 200 (July 2018). DOI: 10.1016/j.jclepro.2018.07.311.

[43] Y. Sun, V. Venugopal, and A. R. Brandt. “Convolutional Neural Network for Short-term Solar Panel Output Prediction”. In: *2018 IEEE 7th World Conference on Photovoltaic Energy Conversion (WCPEC) (A Joint Conference of 45th IEEE PVSC, 28th PVSEC 34th EU PVSEC)*. 2018, pp. 2357–2361. DOI: 10.1109/PVSC.2018.8547400.

[44] Jinsong Zhang et al. “Deep photovoltaic nowcasting”. In: *Solar Energy* 176 (2018), pp. 267–276. ISSN: 0038-092X. DOI: https://doi.org/10.1016/j.solener.2018.10.024. URL: http://www.sciencedirect.com/science/article/pii/S0038092X1831003X.

[45] Fei Wang et al. “Image phase shift invariance based cloud motion displacement vector calculation method for ultra-short-term solar PV power forecasting”. In: *Energy Conversion and Management* 157 (2018), pp. 123–135. ISSN: 0196-8904. DOI: https://doi.org/10.1016/j.enconman.2017.11.080. URL: http://www.sciencedirect.com/science/article/pii/S0196890417311305.

[46] Viv Bone et al. “Intra-hour direct normal irradiance forecasting through adaptive clear-sky modelling and cloud tracking”. In: *Solar Energy* 159 (2018), pp. 852–867. ISSN: 0038-092X. DOI: https://doi.org/10.1016/j.solener.2017.10.037. URL: http://www.sciencedirect.com/science/article/pii/S0038092X17309064.

[47] A. Radovan and Z. Ban. “Prediction of HSV color model parameter values of cloud movement picture based on artificial neural networks”. In: *2018 41st International Convention on Information and Communication Technology, Electronics and Microelectronics (MIPRO)*. 2018, pp. 1110–1114. DOI: 10.23919/MIPRO.2018.8400202.

[48] Julien Nou et al. “Towards the intrahour forecasting of direct normal irradiance using sky-imaging data”. In: *Heliyon* 4.4 (2018), e00598. ISSN: 2405-8440. DOI: https://doi.org/10.1016/j.heliyon.2018.e00598. URL: http://www.sciencedirect.com/science/article/pii/S2405844017320893.

[49] Cong Feng et al. *An Unsupervised Clustering-Based Short-Term Solar Forecasting Methodology Using Multi-Model Machine Learning Blending*. 2018. arXiv: 1805.04193 [cs.LG].

[50] Mehdi Aakroum et al. “Deep Learning for Inferring the Surface Solar Irradiance from Sky Imagery”. In: *2017 International Renewable and Sustainable Energy Conference (IRSEC)* (Dec. 2017). DOI: 10.1109/irsec.2017.8477236. URL: http://dx.doi.org/10.1109/IRSEC.2017.8477236.

[51] Robin Spiess et al. *Learning to Compensate Photovoltaic Power Fluctuations from Images of the Sky by Imitating an Optimal Policy*. 2018. arXiv: 1811.05788 [cs.LG].

[52] Xin Zhao et al. “3D-CNN-based feature extraction of ground-based cloud images for direct normal irradiance prediction”. In: *Solar Energy* 181 (2019), pp. 510–518. ISSN: 0038-092X. DOI: https://doi.org/10.1016/j.solener.2019.01.096. URL: http://www.sciencedirect.com/science/article/pii/S0038092X19301082.

[53] D. Anagnostos et al. “A method for detailed, short-term energy yield forecasting of photovoltaic installations”. In: *Renewable Energy* 130 (2019), pp. 122–129. ISSN: 0960-1481. DOI: https://doi.org/10.1016/j.renene.2018.06.058. URL: http://www.sciencedirect.com/science/article/pii/S0960148118307109.

[54] J. O. Zhe Ao et al. “A Short Term Cloud Tracking Model Based on the Bruhn Optical Flow Method”. In: *IGARSS 2019 - 2019 IEEE International Geoscience and Remote Sensing Symposium*. 2019, pp. 7598–7601. DOI: 10.1109/IGARSS.2019.8899104.

[55] “Determination of cloud transmittance for all sky imager based solar nowcasting”. In: *Solar Energy* 181 (2019), pp. 251–263. ISSN: 0038-092X. DOI: https://doi.org/10.1016/j.solener.2019.02.004. URL: http://www.sciencedirect.com/science/article/pii/S0038092X19301306.

[56] S. Zhang et al. “Intrahour Cloud Tracking Based on Optical Flow”. In: *2019 Chinese Control Conference (CCC)*. 2019, pp. 3023–3028. DOI: 10.23919/ChiCC.2019.8865296.

[57] Z. Zhen et al. “Pattern Classification and PSO Optimal Weights Based Sky Images Cloud Motion Speed Calculation Method for Solar PV Power Forecasting”. In: *IEEE Transactions on Industry Applications* 55.4 (2019), pp. 3331–3342. DOI: 10.1109/TIA.2019.2904927.

[58] S. Tiwari, R. Sabzehgar, and M. Rasouli. “Short Term Solar Irradiance Forecast based on Image Processing and Cloud Motion Detection”. In: *2019 IEEE Texas Power and Energy Conference (TPEC)*. 2019, pp. 1–6. DOI: 10.1109/TPEC.2019.8662134.

[59] Yuchi Sun, Vignesh Venugopal, and Adam R. Brandt. “Short-term solar power forecast with deep learning: Exploring optimal input and output configuration”. In: *Solar Energy* 188 (2019), pp. 730–741. ISSN: 0038-092X. DOI: https://doi.org/10.1016/j.solener.2019.06.041. URL: http://www.sciencedirect.com/science/article/pii/S0038092X19306164.

[60] G. Andrianakos et al. “Sky Image forecasting with Generative Adversarial Networks for cloud coverage prediction”. In: *2019 10th International Conference on Information, Intelligence, Systems and Applications (IISA)*. 2019, pp. 1–7. DOI: 10.1109/IISA.2019.8900774.

[61] Jane Oktavia Kamadinata, Tan Lit Ken, and Tohru Suwa. “Sky image-based solar irradiance prediction methodologies using artificial neural networks”. In: *Renewable Energy* 134 (2019), pp. 837–845. ISSN: 0960-1481. DOI: https://doi.org/10.1016/j.renene.2018.11.056. URL: http://www.sciencedirect.com/science/article/pii/S0960148118313752.

[62] Y. Lin et al. “Transfer Learning on the Feature Extractions of Sky Images for Solar Power Production”. In: *2019 IEEE Power Energy Society General Meeting (PESGM)*. 2019, pp. 1–5. DOI: 10.1109/PESGM40551.2019.8973423.

[63] Talha A. Siddiqui, Samarth Bharadwaj, and Shivkumar Kalyanaraman. *A deep learning approach to solar-irradiance forecasting in sky-videos*. 2019. arXiv: 1901.04881 [cs.CV].

[64] Soumyabrata Dev et al. *Estimating Solar Irradiance Using Sky Imagers*. 2019. arXiv: 1910.04981 [eess.IV].

[65] M. Caldas and R. Alonso-Suárez. “Very short-term solar irradiance forecast using all-sky imaging and real-time irradiance measurements”. In: *Renewable Energy* 143 (2019), pp. 1643–1658. ISSN: 0960-1481. DOI: https://doi.org/10.1016/j.renene.2019.05.069. URL: https://www.sciencedirect.com/science/article/pii/S0960148119307426.

[66] Tingting ZHU et al. “Inter-hour direct normal irradiance forecast with multiple data types and time-series”. In: *Journal of Modern Power Systems and Clean Energy* 7.5 (Sept. 2019), pp. 1319–1327. ISSN: 2196-5420. DOI: 10.1007/s40565-019-0551-4. URL: https://doi.org/10.1007/s40565-019-0551-4.

[67] Manuel Jesús Espinosa-Gavira et al. “Cloud motion estimation from small-scale irradiance sensor networks: General analysis and proposal of a new method”. In: *Solar Energy* 202 (2020), pp. 276–293. ISSN: 0038-092X. DOI: https://doi.org/10.1016/j.solener.2020.03.081. URL: http://www.sciencedirect.com/science/article/pii/S0038092X20303273.

[68] T. Leelaruji and N. Teerakawanich. “Short Term Prediction of Solar Irradiance Fluctuation Using Image Processing with ResNet”. In: *2020 8th International Electrical Engineering Congress (iEECON)*. 2020, pp. 1–4. DOI: 10.1109/iEECON48109.2020.229573.

[69] Quentin Paletta and Joan Lasenby. *Convolutional Neural Networks applied to sky images for short-term solar irradiance forecasting*. 2020. arXiv: 2005.11246 [cs.CV].